

**pH-RESPONSIVE CYCLODEXTRIN NANOSPONGES FOR DRUG
DELIVERY**

**by
SERAP SEZEN**

**Submitted to the Graduate School of Engineering and Natural Sciences in partial
fulfillment of the requirements for the degree of Doctor of Philosophy.**

**Sabanci University
December 2024**

SERAP SEZEN 2024 ©

All Rights Reserved

ABSTRACT

pH-RESPONSIVE CYCLODEXTRIN NANOSPONGES FOR DRUG DELIVERY

SERAP SEZEN

Molecular Biology, Genetics and Bioengineering, PhD Thesis, December 2024

Thesis Advisor: Assoc. Prof. Dr. Feray Bakan Mısırlıoğlu

Thesis Co-Advisor: Assoc. Prof. Dr. Ali Zarrabi

Keywords: Cyclodextrin Nanosponges, Cancer Therapy, pH-Responsiveness, Doxorubicin, Targeted Drug Delivery.

Smart drug delivery systems offer significant advantages in cancer treatment. The tumor microenvironment's acidified pH, caused by cancer cell metabolism, provides a unique opportunity to exploit pH-responsive therapies.

In this thesis, pH-responsive cyclodextrin nanosponges (CD NSs) were synthesized for the first time for drug delivery applications. β -cyclodextrin (β -CD) was oxidized and crosslinked with adipic acid dihydrazide (ADH) to produce NSs containing acid-sensitive

hydrazone bonds, designed to cleave in acidic conditions. These NSs were used for doxorubicin delivery, with additional functionalization using folic acid to enhance selective uptake by cancer cells.

Comprehensive characterization techniques, including FTIR, ¹H-NMR, DLS, zeta potential measurements, UV-Vis, TGA, DSC, XRD, SEM, and TEM, confirmed successful β-CD oxidation, NS formation, drug loading, and folic acid conjugation. The NSs exhibited an amorphous structure, spherical morphology, uniform size distribution, and minimal surface charge. These NSs were thermally stable, having doxorubicin encapsulation efficiency (EE) of 58% and showed a 1.5-fold increase in drug release under acidic conditions compared to neutral pH.

Biological tests demonstrated that blank NSs were non-toxic to MCF-7 breast cancer cells and L929 fibroblast cells. Doxorubicin-loaded NSs (NS-Dox) induced selective cytotoxicity in MCF-7 cells while sparing L929 cells from the harmful effects. FA conjugation significantly enhanced therapeutic efficacy by reducing the IC₅₀ value of NS-Dox. Cellular uptake studies confirmed that doxorubicin encapsulation in NSs substantially improved internalization by MCF-7 cells.

These findings highlight the potential of the synthesized pH-responsive NSs as effective and targeted delivery vehicles for cancer therapy, offering a promising alternative to conventional treatments.

ÖZET

pH-DUYARLI SIKLODEKSTRİN NANOSÜNGERLERİNİN İLAÇ TAŞINIMI İÇİN GELİŞTİRİLMESİ

SERAP SEZEN

Moleküler Biyoloji, Genetik ve Biyomühendislik, Doktora Tezi, Aralık 2024

Tez Danışmanı: Doç. Dr. Feray Bakan Mısırlıoğlu

Tez Eş-Danışmanı: Doç. Dr. Ali Zarrabi

Anahtar Kelimeler: Siklodekstrin Nanosüngerleri, Kanser Terapisi, pH'a duyarlılık, Doksorubisin, Hedefli İlaç Taşınımı.

Akıllı ilaç dağıtım sistemleri, kanser tedavisinde önemli avantajlara sahiptir. Kanser hücresi metabolizması tarafından oluşturulan tümör mikroortamının asidik pH'ı, pH'a duyarlı tedavilerin kullanımını konusunda benzersiz fırsatlar sunar.

Bu tezde, ilaç taşınım uygulamaları için ilk kez pH'a duyarlı siklodekstrin nanosüngerleri (CD NS'ler) sentezlenmiştir. Asidik koşullarda parçalanacak şekilde tasarlanmış asite

duyarlı hidrazon bağları içeren NS'ler üretmek için β -siklodekstrin (β -CD) oksitlenmiş ve adipik asit dihidrazid (ADH) ile çapraz bağlanmıştır. Bu NS'ler, doksorubisin taşınımı için kullanılmış ve dahası kanser hücrelerinin seçici alımını artırmak için folik asit ile de fonksiyonelleştirilmiştir.

FTIR, $^1\text{H-NMR}$, DLS, zeta potansiyel ölçümleri, UV-Vis, TGA, DSC, XRD, SEM ve TEM gibi kapsamlı karakterizasyon teknikleri, β -CD oksidasyonunun, NS oluşumunun, ilaç yüklenmesinin ve folik asit konjugasyonunun başarılı olduğunu doğrulamıştır. NS'ler, amorf bir yapıya, küresel bir morfolojiye, homojen bir boyut dağılımına ve minimal yüzey yüküne sahiptirler. Termal olarak kararlı olan bu NS'ler, %58 oranında doksorubisin yükleme verimliliği (EE) göstermiş ve nötr pH'a kıyasla asidik koşullarda ilaç salınımında bir buçuk kat artışa sahip olmuşlardır.

Biyolojik testler, boş NS'lerin MCF-7 meme kanseri hücrelerine ve L929 fibroblast hücrelerine toksik olmadığını göstermiştir. Doksorubisin yüklü NS'ler (NS-Dox), MCF-7 hücrelerinde seçici sitotoksikite indüklerken, L929 hücrelerini ilacın zararlı etkilerinden korumuşlardır. Folik asit konjugasyonu, NS-Dox'un IC_{50} değerini azaltarak tedavi etkinliğini önemli ölçüde artırmıştır. Hücre alımı çalışmaları, NS'lerde doksorubisinin kapsüle edilmesinin MCF-7 hücreleri tarafından alımını önemli ölçüde artırmıştır.

Bu bulgular, sentezlenen pH-duyarlı NS'lerin kanser tedavisi için etkili ve hedeflenmiş taşıyıcı araçlar olarak potansiyelini vurgulamakta ve geleneksel tedavilere umut verici bir alternatif sunmaktadır.

ACKNOWLEDGEMENTS

I am grateful to my supervisors, Assoc. Prof. Dr. Feray Bakan Mısırlıođlu and Assoc. Prof. Dr. Ali Zarrabi, for their guidance, support, and significant time and effort during my studies. Their advice helped me throughout the entire thesis.

I am also thankful for my thesis committee members, Assoc. Prof. Dr. Meral Yüce, Assoc. Prof. Dr. Murat Topuzođulları, Assoc. Prof. Dr. Nur Mustafaođlu Varol and Assoc. Prof. Dr. Yasemin Budama Kılınç for their valuable comments to finalize my thesis.

I would like to express my gratitude to my beloved friend Dr. Atefeh Zarepour for her valuable contributions on the subject, and Şevin Adıgüzel for her supports during the cell culture studies. I also thank to my friends Dr. Alp Yetişgin, Burak Ölmez and Sarp Kölgesiz for their support in several analyses.

I am very grateful to have such incredible husband, Yusuf Sezen, who supported me during my entire PhD and my son Selim, to be a huge cherishment for us. I dedicated this thesis to my beloved ones.

Finally, I would like to express my gratitude to TÜBİTAK for financially supporting me via National PhD Scholarship Program (2211A) during my thesis. The funder did not participate in the study design, data collection or analysis, the decision to publish, or the preparation of this thesis.

“To my husband and son...”

TABLE OF CONTENTS

1. Introduction.....	1
1.1. Cancer	1
1.1.2. Cancer Treatment.....	3
1.1.3. Nanoparticle-based Drug Delivery Systems for Cancer Treatment.....	5
1.2. Cyclodextrins	10
1.2.1. Definition, Structure and Properties of Cyclodextrins.....	10
1.2.2. Modifications of Cyclodextrins	15
1.3. Cyclodextrin Nanosponges	19
1.3.1. Definition and Properties of Cyclodextrin Nanosponges	19
1.3.2. Synthesis of Cyclodextrin Nanosponges	21
1.3.3. Types of Cyclodextrin Nanosponges	24
1.3.4. Stimuli-Responsive Cyclodextrin Nanosponges	26
1.4. Cyclodextrin Nanosponges in Drug Delivery.....	27
1.5. Examples of Smart Cyclodextrin Nanosponges in Drug Delivery	32
1.6. Aim of the Study	36
2. Materials and Methods.....	38
2.1. Materials	38
2.2. Methods	39
2.2.1. Synthesis of Oxidized β -Cyclodextrin.....	39
2.2.2. Synthesis of Nanosponges	40
2.2.3. Doxorubicin Loading to the NSs	43
2.2.4. Folic Acid conjugation to NS3:1	44
2.2.5. Preparation of Physical Mixtures.....	44

2.2.6. Aldehyde Content Determination	45
2.2.7. ¹ H-NMR Analysis	45
2.2.8. FTIR Analysis	45
2.2.9. Size and Zeta Potential Measurements	46
2.2.10. XRD Analysis	46
2.2.11. TGA Analysis	46
2.2.12. DSC Analysis	47
2.2.13. TEM Analysis	47
2.2.14. SEM Analysis	47
2.2.15. Fluorescence Spectroscopy	47
2.2.16. UV-Vis Analysis.....	48
2.2.17. pH-responsiveness and long-term stability of NS3:1	49
2.2.18. Drug Release Investigations	49
2.2.19. <i>In vitro</i> MTT Assay	50
2.2.20. Confocal Microscopy	51
2.2.21. Cellular Uptake Studies	51
2.2.22. Data Analysis	52
3. Results and Discussion	53
3.1. Synthesis of Oxidized β-CD	54
3.1.1. FTIR Analysis for β-CD Oxidation	55
3.1.2. UV-Vis Analysis for β-CD Oxidation	56
3.1.3. Aldehyde Content Determination	57
3.1.4. Proton NMR Analysis	58
3.1.5. XRD Analysis for β-CD Oxidation.....	59
3.1.6. Thermal Analysis by TGA and DSC.....	60
3.1.7. SEM Analysis for β-CD Oxidation.....	61

3.2. Nanosponge Synthesis	62
3.2.1. Optimization of NS	62
3.2.2. UV-Vis Analysis for NS Synthesis	69
3.2.3. XRD Analysis for NS Synthesis	70
3.2.4. DSC Analysis for NS Synthesis.....	71
3.2.5. SEM Analysis for NS Synthesis	72
3.2.6. TEM Analysis for NS Synthesis	73
3.2.7. pH-responsiveness of NS3:1	74
3.2.8. Stability Assessment of NS3:1	75
3.1. Dox Encapsulation and Release by Optimized NS.....	76
3.1.1. Encapsulation Efficiency and Loading Capacity for NS3:1-Dox.....	76
3.1.2. FTIR Analysis for NS3:1-Dox.....	77
3.2.2. DLS/Zeta Analysis for NS3:1-Dox.....	79
3.2.3. DSC Analysis for NS3:1-Dox.....	80
3.2.4. SEM Analysis for NS3:1-Dox	81
3.2.5. <i>In vitro</i> Drug Release	83
3.4. Folic Acid Conjugation to NS3:1.....	84
3.4.1. FTIR Analysis for NS3:1-FA Conjugate.....	84
3.4.2. UV-Vis Analysis for NS3:1-FA Conjugate	86
3.4.3. DLS/Zeta Analysis for NS3:1-FA Conjugate.....	87
3.4.4. XRD Analysis for NS3:1-FA Conjugate	88
3.4.5. Thermal Analysis for NS3:1-FA Conjugate	89
3.4.5. SEM analysis for NS3:1-FA Conjugate	90
3.4.6. TEM Analysis for NS3:1-FA Conjugate	91
3.5. Dox Loading to NS3:1-FA.....	92
3.5.1. FTIR Analysis for NS3:1-FA-Dox.....	92
3.5.2. DSC Analysis for NS3:1-FA-Dox.....	93

3.5.3. DLS/Zeta Analysis for NS3:1-FA-Dox.....	94
3.5.4. SEM Analysis for NS3:1-FA-Dox	95
3.5.5. In vitro Drug Release	97
3.6. Cell-Based Assays.....	98
3.6.1. MTT Assessment	98
3.6.2. Confocal Analysis for Internalization	105
3.6.3. Cellular Uptake Studies	106
4. Conclusion	110
5. References.....	112

LIST OF TABLES

Table 1. Differences between normal and cancer cells. Adapted with the permission from [5]. Copyright Elsevier.....	2
Table 2. Characteristics of α , β and γ -CDs. Reprinted with the permission of [49], Springer Nature.....	12
Table 3. The amount of Dia3, ADH and molar ratio of [CHO] to ADH of prepared NSs. [CHO] indicates the aldehyde molar ratio.	42
Table 4. Characteristic bands for β -CD and Dia3 with their corresponding identity.....	55
Table 5. Z-average (nm), PDI and Zeta potentials (mV) of NS3:1 in different time intervals which are recorded for the process optimization.	63
Table 6. Characteristic bands for β -CD and Dia3 with their corresponding identity.....	65
Table 7. Z-average, PDI and Zeta Potential values for the NS with different crosslinker ratio.	67
Table 8. The amount of NS, Dox, reaction volume and encapsulation efficiency (EE%) for NS3:05, NS3:1 and NS3:2.	69
Table 9. The amount of Dox loading, EE% and LC (mg/mg) for NS3:1 loaded with different amount of Dox.....	77
Table 10. Characteristic bands for Dox, NS3:1 and NS3:1-Dox with their corresponding identity.	78
Table 11. Z-average (nm), PDI and Zeta potentials (mV) of NS3:1 and NS3:1-Dox. ...	79
Table 12. Characteristic bands for FA, NS3:1 and NS3:1-FA conjugate with their corresponding identity.....	85
Table 13. Z-average (nm), PDI and Zeta potentials (mV) of NS3:1, FA and NS3:1-FA conjugate.....	88
Table 14. Z-Average (nm), PDI and Zeta potential (mV) values for NS3:1-FA and NS3:1-FA-Dox.	94
Table 15. IC ₅₀ values for Dox, NS3:1-Dox and NS3:1-FA-Dox with their corresponding free or encapsulated Dox amount as molarity against MCF-7 cells. The concentration of each specimen for defined IC ₅₀ value was also shown as $\mu\text{g/ml}$ independent of the Dox molarity.	105

LIST OF FIGURES

Figure 1. a) D-glucopyranose subunit of CD, b) truncated cone shape and localization of the hydroxyl (OH) groups in the CD molecule. Hydroxyl (OH) groups pointing outside of the CD cone shape. Hydrophobic cavity (yellow arrow) and hydrogen bonding with water (red dashed line) are also illustrated. n is the number of glucopyranose units. Reproduced from [50] under the terms and conditions of the Creative Commons Attribution (CC BY) license. Copyright 2021, MDPI.....	11
Figure 2. Chemical structure of parent α , β and γ -CDs having 6-, 7 and 8 subunits. Reprinted from [50] under the terms and conditions of the Creative Commons Attribution (CC BY) license. Copyright 2021, MDPI.....	12
Figure 3. Different stoichiometric ratios of host-guest inclusion complexes of CDs. Adapted from [55] under the terms of the Creative Commons (CC BY) license. Copyright 2022, Elsevier.....	14
Figure 4. Applications of CDs in different industrial and research areas. Reproduced from [50] under the terms and conditions of the Creative Commons Attribution (CC BY) license. Copyright 2021, MDPI.	15
Figure 5. Rules for the selective modification of CD molecules. Adapted from [63] under the terms and conditions of the Creative Commons Attribution (CC BY) license. Copyright 2023, MDPI.	16
Figure 6. Schematic representation of commercially available O-substituted CDs. Adapted from [68] under the terms and conditions of the CC BY license. Copyright 2023, MDPI.	17
Figure 7. CD polymers (pCDs) in 5 different morphology and composition. Adapted from [70] under the terms and conditions of the CC BY license. Copyright 2021, MDPI.....	18
Figure 8. Schematic representation of oxidation of β -CD with NaIO_4 . n indicates the number of oxidized units.	19
Figure 9. The use and the advantages of CD NSs in several research and industrial areas. Adapted from [75] under the terms of the CC BY. Copyright 2022, Frontiers.	21
Figure 10. Schematic representation of CD NS synthesis using β -CD and crosslinker. Adapted from [75] under the terms of the CC BY. Copyright 2022, Frontiers.	22

Figure 11. Synthesis of NSs via a) solvent method, b) ultrasound-assisted synthesis, c) emulsion-solvent diffusion and d) melting methods. Adapted from [79] under the terms of the Creative Commons Attribution-NonCommercial-No Derivatives License (CC BY NC ND). Copyright 2023, Cell Press.	24
Figure 12. Schematic representation of methods for preparing CD NS drug complexes via a) lyophilization, b) co-evaporation, and c) kneading methods. Adapted with the permission from [94]. Copyright Springer Nature.....	28
Figure 13. Schematic representation of synthesis of GSH-NS from β -CD, 2-hydroxyethyl disulfide and pyromellitic dianhydride, followed by Dox loading. Adapted with the permission from [80]. Copyright 2020, Elsevier.	33
Figure 14. a) Synthesis of dual-responsive CD NS (TsCl: p-toluenesulfonyl chloride, Ts-CD: 6-mono-(p-toluenesulfonyl)- β -CD, β -CD-NH ₂ : mono-(6-ethylenediamine-6-deoxy)- β -CD, β -CD-NH-ACy: acryloyl-6-ethylenediamine-6-deoxy- β -CD, BACy: N,N-bis(acryloyl)cystamine, AA: acrylic acid), b) TEM images of NS and Dox-loaded NS (NS-Dox), c) Confocal images A549 cells incubated with Dox- loaded NS(NS-Dox) for different time. DAPI was used to label the nucleus of the cells. Adapted with the permission from [88]. Copyright 2021, Elsevier.	35
Figure 15. The schematic representation of β -CD oxidation. 3 out of 7 glucopyranose units were oxidized with NaIO ₄ . Digital images for β -CD (left) and Dia3 (right) in water.	40
Figure 16. The schematic representation of NS synthesis through the reaction between Dia3 and ADH, forming hydrazone bonds (shown in yellow circles).....	41
Figure 17. Digital images, Z-Average (nm) and PDI values for NS3:1 at a) 48 h in blurry solution, b) after acetone addition and centrifuge, c) after placing in oven, acetone and water addition followed by scraping and dialysis and d) freeze-dried forms.	42
Figure 18. The schematic representation for FA conjugation to NS3:1.....	44
Figure 19. Calibration curve for Dox in water.....	48
Figure 20. Calibration curve for FA in DMSO.	49
Figure 21. Schematic representation of NS synthesis, FA conjugation and Dox loading.	54
Figure 22. FTIR spectra of β -CD and oxidized β -CD (namely Dia3).	55
Figure 23. UV-Vis spectrum of β -CD and Dia3.	56

Figure 24. a) The alteration in the pH of Dia3 and β -CD (as a control) that dissolves in hydroxylamine hydrochloride mixture. b) Titration and differential curves for Dia3 formulated in hydroxylamine hydrochloride solution.	58
Figure 25. $^1\text{H-NMR}$ spectra of β -CD and Dia3. The spectrums of β -CD and Dia3 were recorded in D_2O and DMSO-d_6 , respectively.	59
Figure 26. XRD spectra of β -CD and Dia3.	60
Figure 27. a) TGA analysis and b) DSC diagrams for β -CD and Dia3.	61
Figure 28. SEM micrographs for β -CD and Dia3.....	62
Figure 29. Time-dependent size distribution by intensity of NS3:1. a) peak intensity distribution by the time and b) peak values for each time interval.....	64
Figure 30. a) FTIR spectrum of Dia3 and NS3:1, b) schematic representation of NS3:1 (hydrazone bonds labelled with yellow circles), FTIR spectrum of c) Dia3, ADH, Dia3-ADH physical mixture and NS3:1, and d) NS3:05, NS3:1 and NS3:2.	65
Figure 31. Size distribution by intensity of a) NS3:05, b) NS3:1 and c) NS3:2.....	67
Figure 32. TGA analysis of a) Dia3, Dia3-ADH physical mixture (PHY) and NS3:1, b) NSs with different crosslinker ratios.....	68
Figure 33. UV-Vis spectra for Dia3 and NS3:1.....	70
Figure 34. XRD spectra of Dia3 and NS3:1.	71
Figure 35. DSC diagrams for Dia3, Dia3-ADH physical mixture (PHY) and NS3:1....	72
Figure 36. SEM micrographs for Dia3 and NS3:1.	73
Figure 37. TEM analysis of NS3:1 with different magnifications.....	74
Figure 38. Size distribution by intensity of NS3:1 suspended at pH 5.5, 6.5 and 7.4. Z-average (nm) and PDI values of corresponding specimen are also indicated.....	75
Figure 39. Z-average (nm) values of NS3:1 suspended in water and stored for 12 weeks at 4°C	76
Figure 40. FTIR spectra of a) NS3:1, NS3:1-Dox physical mixture, NS3:1-Dox and Dox, b) NS3:1, Dox and NS3:1-Dox in detail.....	78
Figure 41. Size distribution by intensity of NS3:1 and NS3:1-Dox.	80
Figure 42. DSC diagrams of NS3:1, NS3:1-Dox physical mixture (PHY) and NS3:1-Dox.	81
Figure 43. SEM micrographs of NS3:1, Dox, NS3:1-Dox physical mixture (PHY) and NS3:1-Dox samples in freeze-dried state.	82

Figure 44. <i>In vitro</i> release profile of Dox at different pHs from NS3:1 previously loaded with a) 0.5 mg Dox and b) 1 mg Dox. Dox release was calculated by considering the initial loaded amount of Dox.	84
Figure 45. FTIR spectrum for NS3:1, FA and NS3:1-FA conjugate.....	85
Figure 46. UV-Vis analysis of 25 µg/ml of FA, NS3:1-FA and NS3:1 recorded between 500 nm and 200 nm.	87
Figure 47. Size distribution by intensity of NS3:1 and NS3:1-FA.	88
Figure 48. XRD analysis for FA, NS3:1 and NS3:1-FA conjugate.	89
Figure 49. a)TGA analysis for NS3:1, FA, NS3:1-FA and NS3:1-FA physical mixture (PHY) and b) DSC diagrams for NS3:1, FA, NS3:1-FA.	90
Figure 50. SEM images of NS3:1, FA and NS3:1-FA.	91
Figure 51. TEM images of NS3:1-FA with different magnifications.	92
Figure 52. FTIR spectrum of a) NS3:1-FA, NS3:1-FA-Dox, NS3:1-FA-Dox physical mixture (PHY) and Dox, b) NS3:1-FA and NS3:1-FA-Dox.....	93
Figure 53. DSC diagrams for NS3:1-FA, NS3:1-FA-Dox and Dox.	94
Figure 54. Size distribution by intensity of NS3:1-FA and NS3:1-FA-Dox.	95
Figure 55. SEM images of Dox, NS3:1-FA, NS3:1-FA-Dox physical mixture (PHY) and NS3:1-FA-Dox.....	96
Figure 56. <i>In vitro</i> release profile of Dox at different pHs from NS3:1-FA-Dox formulation.....	98
Figure 57. MTT assays for MCF-7 cells treated with a) Dox, NS3:1-Dox, NS3:1-FA-Dox, b) NS3:1 and NS3:1-FA. For an 8 µM concentration, 8 µM free Dox (4.6 µg/ml), 8 µM encapsulated Dox (equivalent to 80 µg/ml for NS3:1-Dox and 96 µg/ml for NS3:1-FA-Dox), and an equal amount of blank NSs (80 µg/ml of NS3:1 and 96 µg/ml of NS3:1-FA) were utilized in MTT assay as higher concentration. *p < 0.05; ***p < 0.0001 by ANOVA.....	100
Figure 58. MTT assays for L929 cells treated with Dox, NS3:1-Dox, NS3:1-FA-Dox and blank NS3:1 and NS3:1-FA for 24 h. For an 8 µM concentration, 8 µM free Dox (4.6 µg/ml), 8 µM encapsulated Dox (equivalent to 80 µg/ml for NS3:1-Dox and 96 µg/ml for NS3:1-FA-Dox), and an equal amount of blank NSs (80 µg/ml of NS3:1 and 96 µg/ml of NS3:1-FA) were utilized in MTT assay as higher concentration. *p < 0.05; **p < 0.005 by ANOVA.....	101
Figure 59. MTT assays for MCF-7 cells treated with a) Dox, NS3:1-Dox, NS3:1-FA-Dox, b) blank NS3:1 and NS3:1-FA. For an 8 µM concentration, 8 µM free Dox (4.6 µg/ml), 8	

μM encapsulated Dox (equivalent to $80 \mu\text{g/ml}$ for NS3:1-Dox and $96 \mu\text{g/ml}$ for NS3:1-FA-Dox), and an equal amount of blank NSs ($80 \mu\text{g/ml}$ of NS3:1 and $96 \mu\text{g/ml}$ of NS3:1-FA) were utilized in MTT assay as higher concentration. *** $p < 0.0001$ by ANOVA. 102

Figure 60. MTT assays for MCF-7 cells treated NS3:1-Dox and NS3:1-FA-Dox at neutral and acidic pH. For an $8 \mu\text{M}$ concentration, $8 \mu\text{M}$ free Dox ($4.6 \mu\text{g/ml}$) and $8 \mu\text{M}$ encapsulated Dox (equivalent to $80 \mu\text{g/ml}$ for NS3:1-Dox and $96 \mu\text{g/ml}$ for NS3:1-FA-Dox) were utilized in MTT assay as higher concentration. * $p < 0.05$; ** $p < 0.005$. *** $p < 0.0001$ by ANOVA. 103

Figure 61. MTT assays for L929 cells treated with a) Dox, NS3:1-Dox, and blank NS3:1 and b) Dox, NS3:1-FA-Dox and NS3:1-FA for 48 h. For an $8 \mu\text{M}$ concentration, $8 \mu\text{M}$ free Dox ($4.6 \mu\text{g/ml}$), $8 \mu\text{M}$ encapsulated Dox (equivalent to $80 \mu\text{g/ml}$ for NS3:1-Dox and $96 \mu\text{g/ml}$ for NS3:1-FA-Dox), and an equal amount of blank NSs ($80 \mu\text{g/ml}$ of NS3:1 and $96 \mu\text{g/ml}$ of NS3:1-FA) were utilized in MTT assay as higher concentration. *** $p < 0.0001$ by ANOVA..... 104

Figure 62. Confocal microscopy images of MCF-7 cells treated with Dox formulations for 2 h and 6 h. 106

Figure 63. Cellular uptake of Dox, NS3:1-Dox and NS3:1-FA-Dox after 2 h and 6 h incubation with the MCF-7 cells. * $p < 0.05$; ** $p < 0.005$. *** $p < 0.0001$ by ANOVA. 108

LIST OF SYMBOLS AND ABBREVIATIONS

AA - Acrylic acid

ADH - Adipic acid dihydrazide

BET - Brunauer-Emmett-Teller

BACy - N,N-bis(acryloyl)-cysteinamine

CaCl₂ - Calcium chloride

CD - Cyclodextrin

CHS - Cholesterol hydrogen succinate

CLSM - Confocal laser scanning microscopy

CM-β-CD - Carboxymethyl-β-cyclodextrin

DLS - Dynamic light scattering

DMAP - 4-(Dimethyl amino) pyridine

DMEM - Dulbecco's modified Eagle's medium

DMF - Dimethyl formamide

DMSO - Dimethyl sulfoxide

DNA - Deoxyribonucleic acid

DPBS - Dulbecco's phosphate buffer saline

DPC - Diphenyl carbonate

DSC - Differential scanning calorimetry

Dox - Doxorubicin

ECM - Extracellular matrix

EDC - N-(3-Dimethylaminopropyl)-N'-ethyl carbodiimide hydrochloride

EE - Encapsulation efficiency

EPR - enhanced permeability and retention

FA - Folic acid

FBS - Fetal bovine serum

Fe₃O₄ - Magnetite

FTIR - Fourier transform infrared spectroscopy

HCl - Hydrochloric acid

¹H-NMR - Proton Nucleic Magnetic Resonance

HP-β-CD - Hydroxypropyl-β-cyclodextrin

IC₅₀ - The half-maximal inhibitory concentration

LC - Loading capacity

MIP - Molecularly imprinted polymer

MTT - Thiazolyl blue tetrazolium bromide

M-β-CD - Methyl-β-cyclodextrin

NaIO₄ - Sodium periodate

NaOH – Sodium hydroxide

NIR - Near infrared

NP - Nanoparticle

NS - Nanosponge

PBS- Phosphate buffer saline

pCDs - Cyclodextrin polymers

PDI - Polydispersity index

PEG – Polyethylene glycol

pen/strep - Penicillin-streptomycin

PMDA - Pyrometric dianhydride

ppm - Parts per million

SBE- β -CD - Sulfobutylether- β -cyclodextrin

SEM - Scanning electron microscopy

TEM - Transmission electron microscopy

TGA - Thermogravimetric analysis

Ts-CD - 6-mono-(p-toluenesulfonyl)- β -cyclodextrin

TsCl - p-toluenesulfonyl chloride

XRD - X-ray diffraction

β -CD-NH₂ - mono-(6-ethylenediamine-6-deoxy)- β -cyclodextrin

β -CD-NH-ACy : Acryloyl-6-ethylenediamine-6-deoxy- β -cyclodextrin,

1. Introduction

1.1. Cancer

Cancer is defined as a group of diseases arising from uncontrollable growth and division of cells, which may originate from any part of the human body. Cancer cells, along with other cells and their extracellular matrix (ECM), form tumors [1]. Tumors can be benign or malignant, and malignant tumors have the potential to spread to other tissues and organs. The main causes of cancer are genetic, but external factors such as physical, chemical, and biological carcinogens are also strongly associated with cancer formation [2].

Cancer arises when there is a mutation in the genes that control the main events in cancer progression, such as avoiding apoptosis, supporting mutations and gene instability, and enhancing the signals for cells to multiply. Most of these mutations are associated with either loss-of-function in tumor suppressor genes or gain-of-function in oncogenes (or proto-oncogenes) [3]. Specific classes of genes in cells, known as cancer genes or drivers of cancers, play a crucial role in promoting cancer in any type of cell within the body. Cancer genes encode oncogenes, phosphatases, tumor suppressor genes, transcription factors, kinases, and cell surface receptors [4]. Table 1 illustrates the distinct characteristics that cancer cells acquire from somatic cells. lose sensitivity to signals sent by nearby cells and do not differentiate [5]. Currently, researchers have identified 727 cancer genes that drive 41 distinct cancer varieties in humans [4].

Table 1. Differences between normal and cancer cells. Adapted with the permission from [5]. Copyright Elsevier.

	Normal cells	Cancer cells
Size and shape	Regular, small and uniformly shape	Irregular, large and variable shape
Nucleus	Small and single nucleus	Large and multiple nucleus
Genome	Integrity genome	Lack of integrity genome with difference mutations
Growth and proliferation	In control	Self-renewable (non-controllable)
Cell Function	Normal	Lose some or all differentiated functions of their parent cells
Blood Supply	Angiogenesis during repair	Tumor Angiogenesis
Membrane Composition	The normal polar surface with the regular receptors	Lose polarity, over-expression of some proteins and receptors as markers
Environmental pH	Intracellular pH is generally ~7.2 and lower than the extracellular pH of ~7.4	Higher intracellular pH of >7.4 and a lower extracellular pH of ~6.7–7.1
Death	Mortal	Immortal
Nutrient source	Glucose	Fat, ketone, Serine, Glycine, Glucose and etc.

Cancer cells form solid tumors, also known as neoplasms. The characteristics of the tumor microenvironment are quite different than those of normal tissues. Along with the cancer cells, other cells, including immune cells, fibroblasts, and other stromal cells, are located in the tumor niche [6]. Moreover, the altered metabolism of the tumor cells leads to hypoxia and acidification of the tumor microenvironment, a phenomenon known as the Warburg effect [7]. Tumor cells rely on glycolysis for their energy metabolism, in contrast to oxidative phosphorylation, which generates lactic acid and causes acidification in

nearby tissues. During tumor formation, the remodeling of the ECM causes the tumor to be stiffer than the normal tissue [8]. Altered physicochemical properties of this new ECM play a crucial role in cancer progression and metastasis, as well as the response to the therapeutics [9]. Neovascularization, a phenomenon where newly developed blood vessels emerge in the tumor niche, also links tumor progression. Neovascularization occurs just after angiogenesis, an important step for tumor spreading. Tumors abnormally generate blood vessels more quickly than normal blood vessels, supporting tumor ingrowth and metastasis [5,10].

The classification of human cancers primarily depends on the tissues and organs involved. For instance, epithelial cells form carcinomas, while bone or soft tissues form sarcomas. Bone marrow contains leukemias, while B or T cells harbor lymphomas. Other classifications include specific types of cancer, cancer grade according to the World Health Organization, and cancer spread according to the Tumor Node Metastasis system [11].

Every year, cancer, the second deadliest disease in the world, claims the lives of millions of people due to its metastasis [5]. According to the International Agency for Research on Cancer, approximately 19.3 million cancer cases and 10.0 million deaths by cancer took place in 2020 in 185 countries [12]. The American Cancer Society reported 1.96 million new cancer cases and 0.61 million cancer deaths in the United States in 2023 [13]. However, if detected in the early stages and properly cured, most cancers have a high survival rate. There are multiple diagnostic tests for cancer in the clinic, from blood tests to the screening and molecular analysis [14]. Early application of various cancer treatment strategies can lead to a higher survival rate compared to late stages. These strategies include surgery, radiation, chemotherapy, immunotherapy, gene therapy, and nanomedicine, as well as their combinations [15].

1.1.2. Cancer Treatment

During the last decades, with the advancement of technologies, researchers have been able to understand cancer formation and progression, which eventually led to the development of various strategies to fight against it. However, there are certain

characteristics of cancers that limit the use of treatment strategies. These circumstances include the various mutations in the genes, heterogeneity inside and outside of the cancer cells, and the dynamic structure of the cancer. Unlike these drawbacks, traditional and next-generation therapies are applied for the treatment of cancer [5].

The traditional modalities include surgery, chemotherapy, radiation, and proton therapy. Surgery involves removing cancer tissue. Surgery entails the removal of the tumor, a method that is invasive, location-dependent, and carries a high risk of tumor recurrence. Radiation therapy uses high-energy radiation to kill tumor cells while damaging the nearby cells and tissues [15]. On the other hand, proton therapy, a highly precise form of radiation therapy, employs protons to destroy cells, but it is only effective against specific cancer types and necessitates the use of an expensive device [5]. Chemotherapy employs cytotoxic drugs to eliminate tumor cells, but its non-specific nature also causes damage to normal cells [15]. Cytotoxic drugs target cells with a high proliferation rate, such as cancer cells, as well as the skin, hair, bone marrow, and other tissues, ultimately leading to cardiotoxicity, infertility, and neurotoxicity [5].

Conversely, new therapies arise to reduce the drawbacks of the traditional methods. These ground-breaking therapies include photodynamic therapy, photothermal therapy, gene therapy, and targeted drug delivery with nanoparticles (NPs) [5]. Photodynamic therapy uses a cancer-specific photosensitizer drug. A defined wavelength activates the photosensitizer at the target, generating reactive oxygen species that kill cancer cells. Activating the photosensitizer also affects the blood vessels in the tumor area, thereby facilitating the immune system [16]. These photosensitizers can include cyanine dyes, titanium oxide, quantum dots, certain metallic NPs, and up-conversion NPs. This technique offers low toxicity, non-invasiveness, and high recovery from the disease [5].

Photothermal therapy benefits the heat intolerance of cancer cells. In this method, tumor tissue is heated with an external source of magnetic field, microwaves, ultrasound, or radiofrequency. This temperature increase results in the loosening of the cancer cells from the surrounding tissue, eventually leading to the death of cancer cells. Photothermal agents are used to heat selectively to prevent damage to the surrounding tissues. Photothermal agents absorb near-infrared light and convert this energy into heat [17]. These photothermal agents include near-infrared dyes, porphyrins, and some carbon-based and metal-based nanomaterials. This treatment is limited due to unknown

information about these NPs after the heat is generated. Plus, some NPs heat up to 60 °C, which eventually harms the nearby tissues [5].

Gene therapy aims to modify the genetic material of cancer cells. Gene therapy has three forms, i.e., immunotherapy, oncolytic viro therapy, and gene transfer [5]. Immunotherapy uses vaccines, cytokines, monoclonal antibodies, and lymphocytes to activate the immune system against cancer cells [18]. Vaccine therapy has limited applications due to the inconsistency of the studies. However, antibody therapy showed promising results. In antibody therapy, tumor antigens are recognized by monoclonal antibodies, such as monoclonal human IgG. These monoclonal antibodies are applicable in different forms, such as monoclonal antibodies that can be used as targeting moiety or can be active to induce cellular toxicity [19]. Antibody therapy has promising results compared to other gene therapy methodologies. Oncolytic viro therapy using viral vectors causes viral replication or translation of toxic proteins, resulting in lysis of the target cells [20]. This application has serious safety problems, reducing its potential for cancer treatment. Gene transfer methods directly interfere with the genome of cancer cells. Gene transfer can be completed by viral and non-viral vectors. The limitation for this technique is the complexity of the cancer cell genome as well as the requirement of a higher delivery rate of the target gene sequence [5,21]. Along with the mentioned therapies, exosome-based and stem cell therapies are applied as next-generation treatment strategies against cancer [16].

The last strategy for cancer treatment comprises the use of NP systems to deliver the cytotoxic drugs to the cancer cells. This strategy will be explained in more detail in the following paragraphs.

1.1.3. Nanoparticle-based Drug Delivery Systems for Cancer Treatment

This strategy utilizes the precise delivery of the cytotoxic drugs to the tumor site using several NPs. Chemotherapy drugs possess several disadvantages in cancer treatment. They have poor aqueous solubility and low biodistribution. Additionally, they exhibit unsuitable pharmacokinetics and easily undergo metabolism before reaching their

target [22]. Since they usually interfere with DNA-related events, they are not selective and disrupt normal tissues as well. Therefore, a huge number of carriers for these drugs in nano size were developed in order to achieve precise delivery, minimize side effects, enhance pharmacokinetics, pharmacodynamics, bioavailability, and biodistribution. Hence, they also increase the solubility of the drugs as a first step for the development of carriers [5,23]. For cancer treatment, NPs ranging from 10 to 200 nm are regarded as the gold standard. In this range, NPs can easily accumulate to the tumor site through passive extravasation. Enhanced permeability and retention effects and disrupted lymphatic drainage encourage NPs to accumulate at the tumor site [24]. In order to increase the accumulation and bioavailability of NPs, coating of the NP surface, adding ligands or targeting moieties, altering the surface charge, and adding functional groups to the surface are applied [25]. In some cases, NPs are designed for patients in order to maximize therapeutic efficiency [26]. Accordingly, NP drug systems can be generated in several ways. A drug can be covalently conjugated or incorporated into the NP backbone. Not only drugs but also imaging agents and genetic materials can be carried by these NPs. Plus, some NPs without cargo are able to destroy the cancer cells [5].

NPs are classified in several ways. They can be classified according to their origin, composition, and dimension/morphology. One can prepare NPs from natural, synthetic, or their blends or composite materials. According to the composition, organic, inorganic, and carbon-based materials are utilized to generate NP systems. Organic materials include polymeric and lipid-based ones as well as viral NPs, while inorganic materials include metals and their oxides, ceramics, and semiconductors. Dimensionally, NP systems can be 0-D, 1-D, 2-D, or 3-D, and therefore, they can exhibit various morphological characteristics such as spherical, cylindrical, flat, conical, or irregular shapes [27–29].

Polymeric NPs are one of the main classes of NP systems. The main advantage of using polymer-based NP is the variety of polymers and monomers that are available for use [30]. They also enable design in any shape, size, and charge. Their versatility also includes the incorporation of any type of chemical or biological functional group as well as stimuli-responsiveness [31]. Natural or synthetic polymers can be used to synthesize polymeric NPs. Natural polymers are biocompatible and degradable; however, it is usually challenging to process them and add functional groups compared to the synthetic counterparts. The development of new polymer synthesis techniques enables precise generation of any type of polymer with desired molecular weight, degradability, and

functional groups, enabling us to overcome the limitations related to these polymers. Polymers can be classified according to their type. The types of polymers that are used in nanoparticle preparation include poly (amino acids) and proteins, polysaccharides, glycopolymers, polyesters, phosphate-based polymers, vinyl polymers, polyethylene imine and polyethylene glycol derivatives, and stimuli-responsive polymers [30].

Stimuli-responsive polymers change their structure when there is alteration in the surrounding pH, temperature, redox, or encounter with light, magnetic field, or enzymes. Stimuli-responsive polymers or crosslinkers are used to prepare stimuli-responsive NPs, which are designed to release the cargo upon stimulus [30]. For example, in order to generate pH-responsive polymeric nanoparticles, hydrazone, imine, ortho ester, and acetal/ketal bonds are generated inside the NP system [32]. Polymeric NPs can be prepared with several techniques, including self-assembly, nanoprecipitation, dialysis, emulsion-based self-assembly, emulsion-polymerization, ion gelation/sol-gel method, polymerization-induced self-assembly, spray drying, and templated assembly [30]. The drug loading to prepared NPs can be passive loading or chemical linkages between drug and carrier. The most prominent polymeric NPs are in the shape of spheres. Spherical NPs include micelles, core-shell NPs, polyion complexes, polymersomes, nanogels, stars, and hyperbranched polymers. Except for the spherical NPs, their architecture can be rod-shape, disk, worms, and fibers [30].

Lipid-based NPs are another class of drug carriers with a wide range of applications and versatility. These NPs are able to protect the drugs from elimination before reaching the site, enhance their solubility, provide controlled release in the site of action, and allow loading of both hydrophilic and hydrophobic small molecules. Lipid NPs are composed of four parts: phospholipids, cholesterol, cationic or ionizable lipids, and PEGylated lipids. They are able to pass cell membranes easily due to their resemblance to the cell membrane. The types of lipid-based NPs include liposomes, nanoemulsions, solid-lipid nanoparticles, nanostructured lipid carriers, and their hybrids with polymers as well as extracellular vesicles. Various methods, including nanoprecipitation, single/double emulsification, non-solvent emulsification, thin film hydration, microfluidic processes, and impingement jet mixing, are used to synthesize lipid NPs [33,34].

Inorganic NPs are composed of inorganic materials such as metals, metal oxides, or semiconductors, typically ranging from 1 to 100 nm in size. These NPs exhibit large

surface area, controllable structures, diverse surface chemistry, and unique optical and magnetic properties, making them valuable in medicine, electronics, and environmental science. In biomedicine, inorganic NPs such as gold, silver, iron oxide, and quantum dots are extensively researched for their potential in diagnostics, drug delivery, and therapeutic applications. Their small size allows for easy penetration and distribution within biological systems, while their customizable surface properties enable targeted interactions with specific cellular structures or molecules [28,35]. Inorganic NPs are widely utilized in cancer treatment [36]. For instance, gold NPs can be engineered to selectively accumulate in tumor tissues due to the enhanced permeability and retention effect, allowing for targeted drug delivery or hyperthermia treatment, where the particles are heated to kill cancer cells. Similarly, iron oxide NPs are utilized in magnetic resonance imaging as contrast agents, providing high-resolution images of biological tissues. Additionally, quantum dots, which are semiconductor NPs, are used in fluorescent imaging due to their superior brightness and stability compared to traditional dyes, enabling precise tracking of biological processes at the cellular level. These applications highlight the versatility and potential of inorganic NPs to revolutionize diagnostic and therapeutic strategies in modern medicine [37,38].

Carbon nanomaterials have unique electronic, optical, thermal, and mechanical properties, versatile functionalization chemistry, and apparent biocompatibility and safety compared to metal-based nanomaterials. Graphene, fullerenes, carbon nanotubes, and carbon quantum dots are widely utilized in cancer therapy. These materials have been rendered biocompatible through covalent or non-covalent modifications, such as introducing hydroxyl, carboxyl, or amino groups on their surface, followed by conjugation with protective biopolymers like PEG. Non-covalent modifications involve loading amphiphilic molecules. Over the years, carbon nanomaterials have been proven to efficiently load various bioactive molecules and exhibit promising photosensitizing properties. Furthermore, they can be functionalized for active targeting and tumor homing, although they have also demonstrated antitumor effects through passive targeting. Their inherent optical properties have also spurred research into their use in cancer imaging and sensing, positioning them as promising materials for future bioimaging applications [39,40].

Inorganic and carbon-based NPs present several disadvantages. Inorganic NPs can pose challenges related to potential toxicity, immunogenicity, and water dispersity. The small

size and large surface area of these NPs can lead to increased reactivity and potential interactions with biological systems. Moreover, the biodistribution and clearance of inorganic NPs from the body can vary widely depending on their size, shape, surface chemistry, and route of administration, which may complicate their use in biomedical applications [41,42]. Similarly, carbon-based NPs also have inherent drawbacks, such as the fact that carbon nanotubes can induce inflammation and granuloma formation in biological tissues. Furthermore, concerns persist regarding the biodegradability of carbon-based nanoparticles in physiological environments, potentially leading to accumulation and persistence in tissues over time. These factors underscore the importance of thorough characterization and rigorous testing to assess the safety and efficacy of both inorganic and carbon-based nanoparticles before their clinical translation, ensuring that their benefits outweigh potential risks in medical and pharmaceutical applications [43].

Along with the conventional NPs for drug delivery, new delivery systems, including niosomes, nanobubbles, nanosponges (NSs), exosomes, virosomes, and cyclodextrin (CD), are also utilized in such areas [5]. Niosomes, composed of non-ionic surfactants and cholesterol or amphiphilic molecules with sizes ranging from 10 to 1000 nm, are self-assembled vesicles. They allow the incorporation of both hydrophilic and hydrophobic drugs. Compared to liposomes, they are more stable and are simple to synthesize. They are able to enhance the pharmacokinetic properties of the drug molecules, as well as the toxicity related to them. They can also be functionalized with various functional groups and ligands, allowing them to deliver the tumor site more precisely [44]. Nanobubbles are NPs containing gas inside their cavity, having sizes ranging from 150 to 500 nm. They are composed of a gas core and shell, and the shell can be made up of proteins, polymers, phospholipids, or surfactants. Both hydrophobic and hydrophilic compounds, as well as the targeting ligands, can be incorporated into them, allowing them to be used in cancer therapy and diagnosis [23]. NSs are another class of next-generation NPs with nano-sized cavities, allowing drug incorporation. NSs have various types, including titanium-based, carbon-coated metal-based, hyper crosslinked polystyrene-based, silica-based, and CD-based NSs. They allow the delivery of drugs in a controlled manner at the site of action. They possess low toxicity and are safe for use in cancer treatment [45]. Exosomes are lipid-based NPs derived from the cell membrane, while virosomes are reconstructed viral

particles [46,47]. In the following paragraphs, CD and their derivatives as alternatives to NP systems will be mentioned in detail.

1.2. Cyclodextrins

1.2.1. Definition, Structure and Properties of Cyclodextrins

CDs are cyclic oligosaccharides formed by the α -(1, 4) glycosidic bonding of D-glucopyranose units. CDs are obtained by the enzymatic degradation of starch via the glucosyltransferase enzyme. In general, three CDs, namely α -CD, β -CD, and γ -CD having 6-, 7-, and 8-units, have been synthesized and purified, dominating the market value of CDs [48].

CDs were first discovered in 1891 by Villiers as crystals named cellulose along with the reducing dextrans when starch was degraded with a bacteria called *Bacillus amylobacter*. From 1903 to 1911, Schardinger studied these celluloses using different bacteria called *Bacillus macerans*, which are able to generate huge amounts of these crystalline dextrans from starch and identify them as cyclic oligosaccharides. Therefore, his enormous contribution to the field led to the term "Schardinger's dextrans" for CDs. In the following years, the purification of CDs was successfully achieved by Freudenberg and co-workers, and the structure of CDs was revealed. In 1948, the structure of γ -CD was clarified with X-ray crystallography. After this discovery, another important feature of the CDs was discovered: the ability to form inclusion complexes, which was first depicted by Schlenk in 1949. Except for the common CDs, other CDs, including δ -CD (9 units), ϵ -CD (10 units), ζ -CD (11 units), and η -CD (12 units), were depicted in 1961 [49].

CDs are formed by the D-glucopyranose units, and each unit in CDs possesses 4C_1 chair conformation (Figure 1.a). This conformation allows CDs to form truncated cone shapes, not regular cylinders (Figure 1.b). In CDs, the hydroxyl groups are located at the wide and narrow ends. C_2 and C_3 hydroxyl groups are located at the wide end, while the C_6 hydroxyl group is at the narrow end. These hydroxyl groups allow CDs to form hydrogen bonds, therefore making them hydrophilic. The inner section of the CDs is hydrophobic

due to the presence of non-polar groups such as ethers and aliphatic-like groups (Figure 1.b). CDs have a flexible structure to be able to change their cavity diameter slightly under specific circumstances [50].

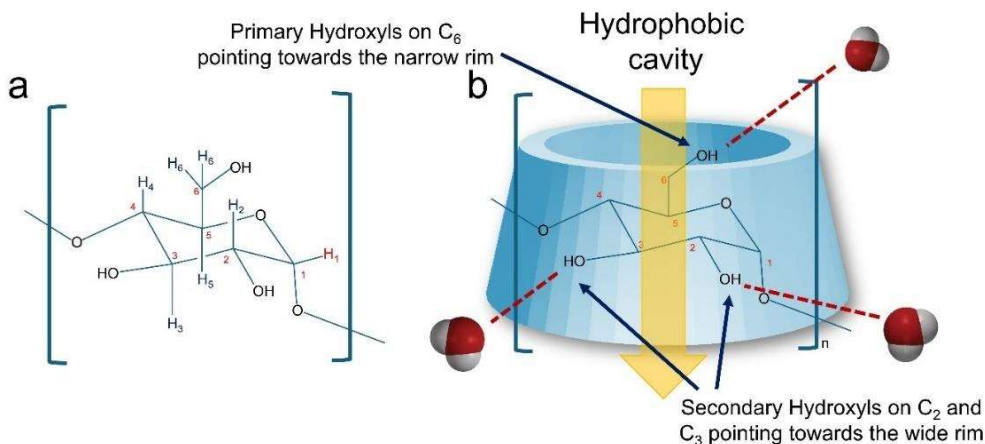


Figure 1. a) D-glucopyranose subunit of CD, b) truncated cone shape and localization of the hydroxyl (OH) groups in the CD molecule. Hydroxyl (OH) groups pointing outside of the CD cone shape. Hydrophobic cavity (yellow arrow) and hydrogen bonding with water (red dashed line) are also illustrated. n is the number of glucopyranose units. Reproduced from [50] under the terms and conditions of the Creative Commons Attribution (CC BY) license. Copyright 2021, MDPI.

Common CDs with the number of 6-, 7-, and 8-D-glucopyranose units are α -CD, β -CD, and γ -CD (Figure 2). Each of these parent CDs possesses unique features in terms of physical and chemical characteristics, which are listed in Table 2.

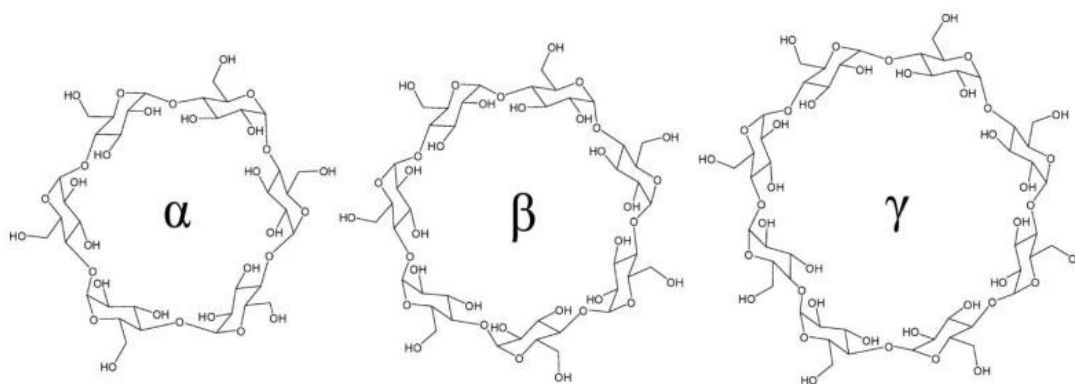


Figure 2. Chemical structure of parent α , β and γ -CDs having 6-, 7 and 8 subunits. Reprinted from [50] under the terms and conditions of the Creative Commons Attribution (CC BY) license. Copyright 2021, MDPI.

Table 2. Characteristics of α , β and γ -CDs. Reprinted with the permission of [49], Springer Nature.

Properties	α	β	γ
Number of glucose units	6	7	8
Molecular weight	972	1135	1297
Solubility in water (g/100 ml) 25 °C	14.5	1.85	23.2
Cavity diameter (°A)	4.7-5.3	6.0-6.5	7.5-8.3
Height of torus (°A)	7.9 ± 0.1	7.9 ± 0.1	7.9 ± 0.1
Diameter of outer periphery (°A)	14.6 ± 0.4	15.4 ± 0.4	17.5 ± 0.4
Approx. cavity volume (°A ³)	174	262	427
Approx. cavity volume in 1 mol CD (ml)	104	157	256
Approx. cavity volume in 1 g CD (ml)	0.10	0.14	0.20
Crystalline forms (from water)	Hexagonal plates	Monoclinic parallelograms	Quadratic prisms
Crystal water, wt %	10.2	13.2-14.5	8.13-17.7
Diffusion constant at 40 °C	3.443	3.224	3.000
Relative permittivity at pH 5.3, 25 °C (on incorporating the toluidinyl group of 6- <i>p</i> -toluidinyl naphthalene 2-sulphonate)	47.5	52.0	70.0

(On incorporating the naphthalene group)	^a	29.5	39.5
Partial molar volumes in solution (ml/mol)	611.4	703.8	801.2
Adiabatic compressibility in aqueous solutions ml (mol ⁻¹ bar ⁻¹) × 10 ⁴	7.2	0.4	-5.0
^a Naphthalene group is too bulky for the α-CD cavity			

The physicochemical properties of cyclodextrins are very well defined in Table 2. Except for those, CDs are stable in water and alkaline solutions; however, in acidic solutions, glycosidic bonds are hydrolyzed, revealing their subunits [50]. They are mostly soluble in water (Table 2), while their solubility increases parallel to the surrounding temperature. When subjected to the thermal analysis, CDs start to decompose after 270 °C, and melting is observed around 300 °C [51]. Plus, CDs are safe to use (generally recognized as safe listed by the Food and Drug Administration), comprising no toxicity to living systems. The orally administered CD showed no toxicity since their adsorption is negligible in the gastrointestinal tract. Plus, they cannot permeate through biological membranes due to the huge number of hydrogen donors and acceptors [52].

Through parent CD molecules, β-CD has great use in industry and biotechnology, despite its low water solubility. It has a rigid structure, and its hydroxyls tend to form hydrogen bonds with each other rather than with their surroundings. The rigid structure also boasts an appropriate inner size for most pharmaceutical drugs, facilitating their incorporation more effectively than other CDs [50]. Plus, β-CD is more available in the market and considered cheap because of the production and purification method; therefore, it is frequently preferred in industry [53].

The remarkable property of CDs is the ability to encapsulate hydrophobic guest molecules into their inner cavities, forming host-guest complexes. These complexes are formed by hydrophobic, electrostatic, and dipole-dipole interactions, or Van der Waals, and dispersion forces [52]. Host-guest interactions allow CDs to form inclusion complexes, enhancing the solubility of guest molecules while protecting them from unwanted degradation. This information is mostly applied in drug delivery. CDs increase the solubility of poorly soluble drugs, as well as their stability and permeability to biological barriers [54]. Inclusion complexes are mostly stable, and the complex formation is dependent on the size and shape of the CD cavity, complex formation or aggregation,

physicochemical features of guest molecules, and the parameters of the inclusion preparation method [50]. CDs are able to form inclusion complexes with different stoichiometric ratios, which also depend on the parameters for inclusion complex preparation (Figure 3). Another property of CDs is their favorable chemical structure, which allows chemical modification mostly through their hydroxyl groups. The modifications of CDs will be further evaluated in the following sections.

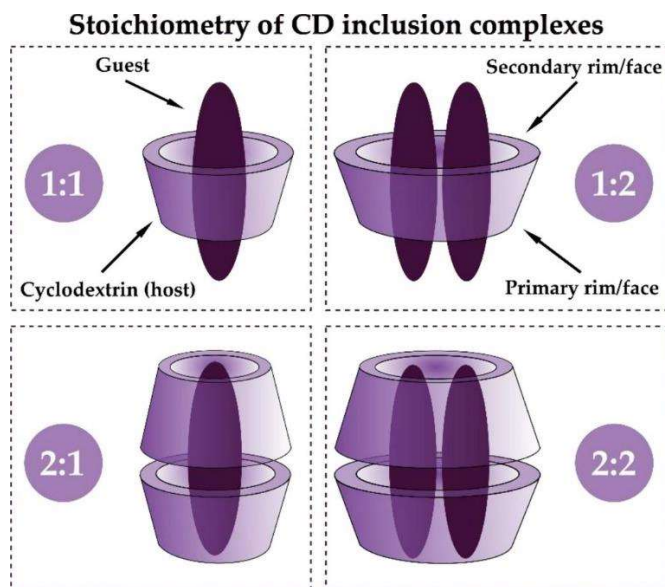


Figure 3. Different stoichiometric ratios of host-guest inclusion complexes of CDs. Adapted from [55] under the terms of the Creative Commons (CC BY) license. Copyright 2022, Elsevier.

Unique properties of CDs make them ideal for several research and industrial areas (Figure 4). They are able to form stable complexes with several organic molecules, thus enhancing their scope. The textile industry employs CDs as leveling agents, enhancing the quality of the organic dyes used in the dyeing process [56]. Additionally, they serve as treatments for wastewater and textile finishing. In cosmetics, CDs are used to enhance stability and control the odor when cosmetics are processed from liquid to solid forms [57]. In the food industry, CDs form complexes with volatile compounds such as flavors, thus enhancing the taste of the food as well as color and taste. They also improve the shelf life of consumables [58]. CDs are known to participate in preparation, processing, and packaging in the food industry [59]. They are also able to form complexes with cholesterol, reducing the amount of cholesterol in the animal-derived consumables [50].

In agriculture, CDs are able to form complexes with several organic molecules, such as growth factors, as well as herbicides, fungicides, and pesticides, thus enhancing the yield of crop production [60]. During the separation processes, CDs facilitate the separation of chemical enantiomers and catalyze and detoxify chemical reactions [61]. And finally, in bioremediation, CDs play a crucial role in the removal of organic pollutants and heavy metals, which form stable complexes favoring their use in bioremediation [62].



Figure 4. Applications of CDs in different industrial and research areas. Reproduced from [50] under the terms and conditions of the Creative Commons Attribution (CC BY) license. Copyright 2021, MDPI.

1.2.2. Modifications of Cyclodextrins

Although native CDs are good excipients in several industrial and research areas, they face some problems, including solubility issues and stable complexations. The solubility problem may cause some nephrotoxicity, which could be related to the renal accumulation of CD crystals. Over 11 thousand CD derivatives have been reported by incorporating amines, amino acids, peptides, polymers, and aromatic rings into the CD molecules or supramolecular assemblies generated by the CDs [63]. In these systems, β -CD is mostly utilized since α -CD has a smaller cavity size and γ -CD has a high production cost with a

low production yield [64,65]. On the other hand, β -CD has a perfect cavity size for most guest molecules, and it can be produced in higher amounts with low production costs while holding low water solubility. Therefore, the modification of CDs is mostly completed on β -CD through the hydroxyl groups. The substitution of functional groups specifies the physicochemical properties of CD use in a defined area.

The functionalization of CD mostly resulted in the conversion of hydroxyl groups to the other functional groups. Among hydroxyl groups, the hydroxyl at C₆ is commonly modified. This is due to the increased nucleophilicity of it. On the other hand, hydroxyl at C₂ is more acidic, and hydroxyl at C₃ is hard to reach (less reactive) (Figure 5) [66]. These substitutions produce mono-6-substituted CDs, per-6-substituted CDs, per-substituted CDs, and random substituted CDs. The mono-substituted CDs possess one functional group per CD ring, which is attached through the oxygen atom at C₆ position. In per-6-substituted CD, functional groups are added through the oxygen atom at position C₆ in each glucose unit in the CD ring. Per-substitution means addition of functional groups to the oxygen atoms of CD at C₆, C₂ and C₃ positions, which could be random substitution as well. In deoxy CDs, the hydroxyl groups are completely replaced by new functional groups, such as thiols or halogens [67].

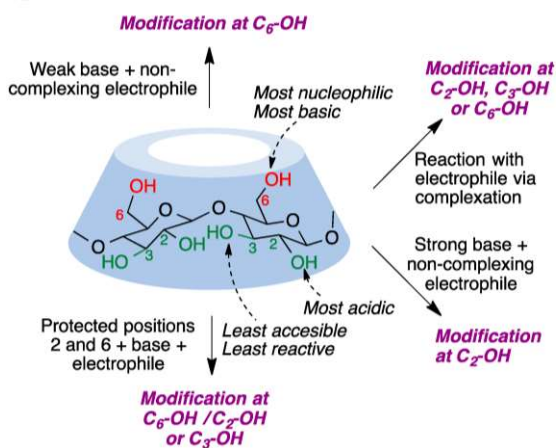


Figure 5. Rules for the selective modification of CD molecules. Adapted from [63] under the terms and conditions of the Creative Commons Attribution (CC BY) license. Copyright 2023, MDPI.

The modifications of β -CD are mostly completed to enhance the solubility through the O-substitution reaction, where some β -CD derivatives are commercially available. These

are methyl- β -CD (M- β -CD), hydroxypropyl- β -CD (HP- β -CD), carboxymethyl- β -CD (CM- β -CD), and sulfobutylether- β -CD (SBE- β -CD) (Figure 6) [68]. For example, the water solubility of β -CD is 18.5 mg/ml, while the solubility of SBE- β -CD is ≤ 500 mg/ml. HP- β -CD also has high complexation ability and a low toxicity profile, compared to commercially modified CDs [67]. The molecular weight also increases upon substitution, altering the other physicochemical properties [69]. The O-substitution reaction is also used for esterification, where the hydroxyl group is reacted with the carboxylic acid group of the other reactant. This strategy is mostly utilized to conjugate drugs or target moieties to the CDs to enhance drug solubility and CD internalization, respectively. These OH groups also offer possible condensation reactions whereby HP- β -CD is obtained by the reaction between CD and propylene oxide. CDs can be polymerized by polymerization condensation reactions with epichlorohydrin or poly-epoxy compounds, resulting in branched polymers [67].

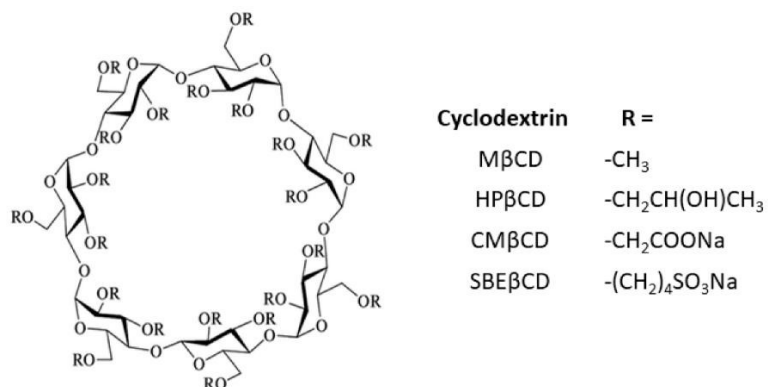


Figure 6. Schematic representation of commercially available O-substituted CDs. Adapted from [68] under the terms and conditions of the CC BY license. Copyright 2023, MDPI.

The hydroxyl groups on CDs also make it easy to attach polymers or macromolecules to them. When suitable polymers or macromolecules are conjugated to CDs, CD-copolymers can self-assemble into core-shell nanoparticles. There are 5 different types of polymer-conjugated CDs, including crosslinked CDs, linear CDs, fixed CDs, CD inclusion compounds, and hyperbranched CDs (Figure 7) [70]. A β -CD molecule contains 21 hydroxyl groups, and modifying just one of these with linear polymers can produce linear CD copolymers. CDs and polymers can be connected through various linkages, and

targeting ligands can be incorporated into CD-grafted linear copolymers to efficiently deliver drugs. Besides, cyclodextrin serves as an ideal core for synthesizing star-shaped polymers. In addition to the unique properties of star-shaped polymers, CD-based star polymers offer the added benefit of encapsulating hydrophobic drugs within their lipophilic cavity through host-guest interactions. As a result, CD-based star polymers hold significant potential for biomedical applications. CDs can be crosslinked with polymers or directly with crosslinking agents to create network structures. These CD-based crosslinked networks can be further developed into hydrogels, or NSs, serving as carriers for anticancer drugs [71].

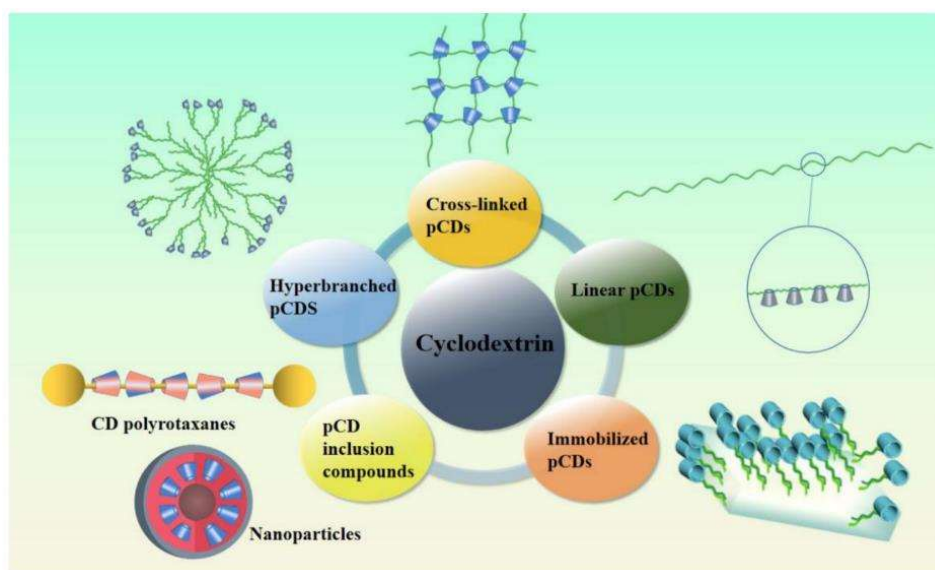


Figure 7. CD polymers (pCDs) in 5 different morphology and composition. Adapted from [70] under the terms and conditions of the CC BY license. Copyright 2021, MDPI

CDs can be further modified by the oxidation reaction. In this reaction, sodium periodate (NaIO_4) oxidizes vicinal diols in the D-glucopyranose unit, leaving the dialdehyde cyclodextrin (Figure 8) [72]. Dialdehyde CDs are reported as having superior water solubility and imparting antibacterial activity. However, the stability of the ring structure and complexation ability are negatively affected [73].

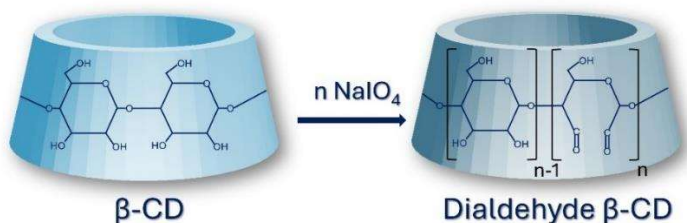


Figure 8. Schematic representation of oxidation of β -CD with NaIO_4 . n indicates the number of oxidized units.

Finally, the polymerization of CD units generates CD NSs, which will be further explained in the following section.

1.3. Cyclodextrin Nanosponges

1.3.1. Definition and Properties of Cyclodextrin Nanosponges

Nanomaterials with nanometer-sized pores are called NS. The term NS refers to the nanoparticles having nanopores inside, which are provided by the central cavity of CD molecules. Therefore, crosslinked CD polymers are called CD NS [52]. NSs are insoluble (form nanosuspension in water) networks and can be synthesized from either organic or inorganic materials. Due to their unique structure, NSs are able to absorb a wide variety of molecules as well as release loaded or encapsulated small molecules [74].

CD NSs are a wide class of nanoporous materials synthesized by the covalent crosslinking of CDs (CD polymers). Since CDs have hydroxyl groups at the wider and narrower rim, it is possible to crosslink them via a broad range of crosslinkers. The physicochemical property of the final product is strongly influenced by the type of the CD and crosslinker, as well as the degree of crosslinking, solvent type, reaction time, and synthesis procedure [52,74].

The as-prepared CD NSs are able to hold both hydrophilic and hydrophobic molecules. Since CDs have slightly hydrophobic cavities, it is possible to make inclusion complexes

with hydrophobic molecules. Once CD molecules crosslink, a void between CD and crosslinker, which is called interstitial space, is generated. This space is surrounded by the remaining hydroxyl groups and the crosslinker itself and is slightly hydrophilic compared to the inner cavity of CD. Thus, interstitial space allows the encapsulation of hydrophilic or high-molecular-weight molecules [52]. This unique behavior of CDs allows the loading of both hydrophilic and hydrophobic molecules, which are eventually released via diffusion in a controlled manner, which makes them suitable for drug delivery purposes [74]. Crosslinking also enhances the stability of the CDs. They are also safe, non-toxic, biocompatible, and biodegradable, promoting their use in biomedical research [52]. Plus, their insolubility is derived from the amorphous structure, which allows recovery of them once they are used to remove pollutants from waste waters. Instead, they are able to hold huge amounts of water in their structure [52].

CD NSs have a diameter of less than 1 μm and a low polydispersity index (PDI) (<0.7). They usually exhibit spherical shape and negative surface potential. They are able to swell in water. They have mostly amorphous structures, meaning that they are dispersed in water and not dissolved. However, water-soluble CD polymers are also synthesized. Their unique, tiny-mesh-like structure allows incorporation of various hydrophilic and lipophilic molecules, increasing their stability. CD NSs are thermally stable; their melting usually starts after 300 $^{\circ}\text{C}$ when subjected to the thermal analysis. They are also resistant to most organic solvents [75].

CD NSs are versatile materials in several research and industrial applications. Especially they are employed in biomedical and pharmaceutical areas, sensors, environmental remediation, and catalysis. Figure 9 outlines the use and advantages of CD NSs. There are a number of benefits to using CD NSs for environmental remediation because of their 3D structure. A variety of exceptionally organized sorbent materials can be synthesized thanks to the decreasing cost and ease of modification of CDs and their analogs. By forming host-guest complexes, diffusing via pores, and interacting at active spots on the NS surface, CD NSs can eliminate heavy metals, dyes, and pesticides from waste waters. CD NSs can serve as direct or indirect sensor materials by activating or deactivating fluorescence through host-guest complexation or molecular assembly with fluorescent or luminescent molecules, providing selectivity and low detection limit. CD NSs, being porous materials with extensive active surface areas and multiple active sites, are seen as

viable candidates for heterogeneous catalysis [75]. The use of CD NSs in the pharmaceutical area will be outlined in the following sections.

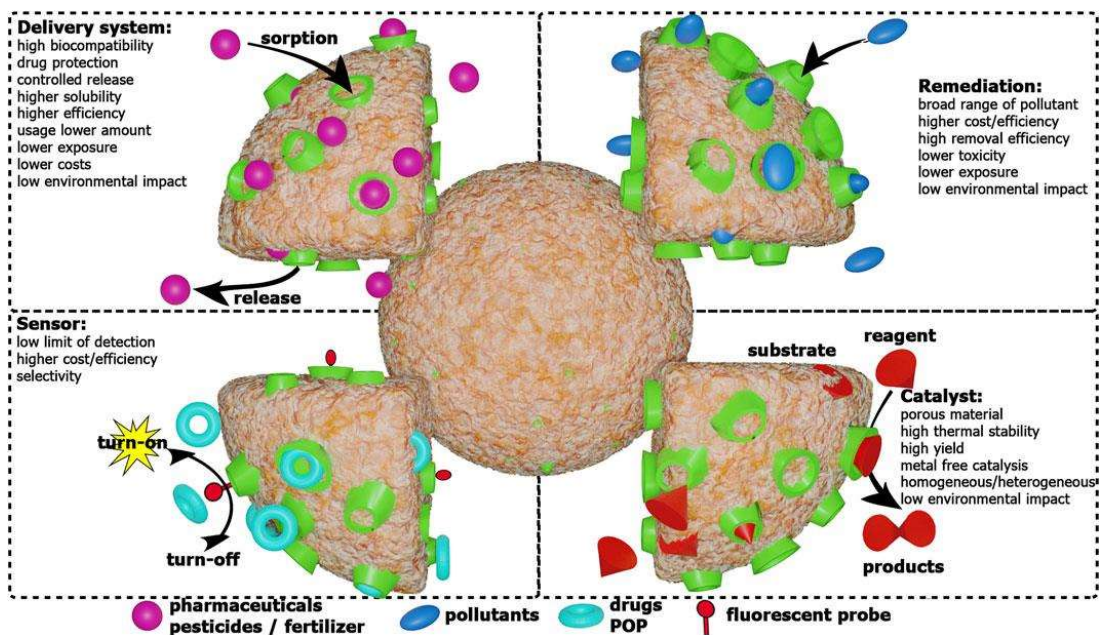


Figure 9. The use and the advantages of CD NSs in several research and industrial areas. Adapted from [75] under the terms of the CC BY. Copyright 2022, Frontiers.

1.3.2. Synthesis of Cyclodextrin Nanosponges

The synthesis of CD NSs usually starts with dissolving the CDs in a solvent, followed by the addition of a catalyst (if necessary), and ends with the addition of a crosslinker (Figure 10). A crosslinker is a functional monomer that has at least two identical functional groups. Then different strategies are applied to polymerize CDs with crosslinkers under different conditions. At the end, CD NSs are generated in solid form and crushed to powder. The CD NSs are washed several times using eco-friendly solvents like ethanol or water before being collected. Even simple dehydration methods are used to generate CD NSs. This method involves dissolving CD, crosslinker, and catalyst in water and allowing them to react for a while. Then, heat treatment is used to remove excess water, and NSs was obtained as white powder. Citric acid-crosslinked CD NSs are usually generated by this way [76].

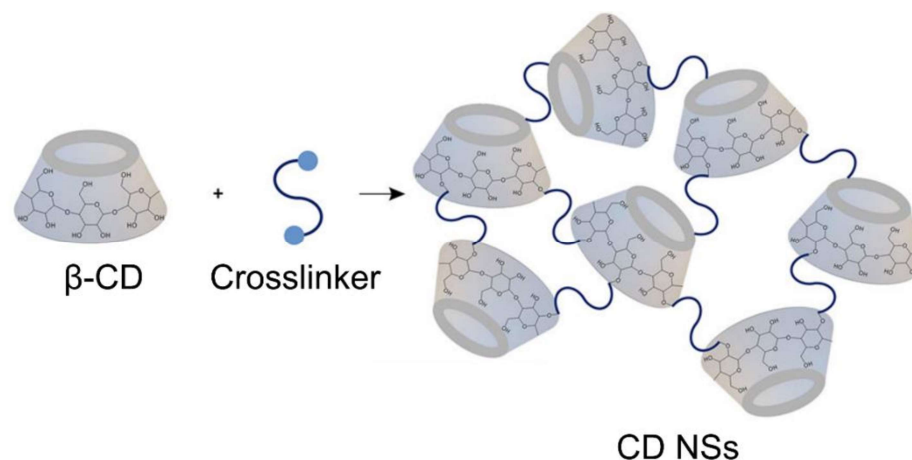


Figure 10. Schematic representation of CD NS synthesis using β -CD and crosslinker. Adapted from [75] under the terms of the CC BY. Copyright 2022, Frontiers.

There are several methods to prepare CD NSs and generate insoluble CD polymers (Figure 11). For this purpose, several crosslinkers are used, which will be explained in Section 1.3.3. The synthetic methods for CD NS synthesis use β -CD as a CD monomer due to its availability and low cost, as well as its complexation ability with most guest molecules. The choice of solvent and catalyst is dependent on the type of reaction. For the techniques, hot melting, solvent condensation, interfacial condensation, emulsion solvent diffusion, ultrasound-assisted, microwave-assisted, mechanochemical, and chain-growth polycondensation synthesis are utilized [75].

The hot-melt procedure uses the reaction between β -CD and usually a carbonyl linker (such as diphenyl carbonate (DPC)), homogenized at the temperature in the range of 90 °C to 130 °C for at least 5 h, followed by longer incubation to complete crosslinking [75]. After the reaction is completed, the mixture is allowed to cool down, and the white pellet is ground. This product is then washed several times with water and ethanol/acetone to remove unbound reactants and byproducts. Soxhlet extraction is used to remove acetone and ethanol for the drying process. The technique is solvent-free, easy, and cheap [77]. In the solvent condensation method, CD and crosslinker, as well as the catalyst (if necessary), were dissolved in dimethyl formamide (DMF), dimethyl sulfoxide (DMSO), or water, where the amount of crosslinker used is much higher compared to other techniques. After a complete reaction, a solvent (acetone, ethyl acetate, or water) might be used to precipitate CD NS. Carbonyl compounds are mostly used as crosslinkers. When the dianhydride linkers are used, additional catalysts such as triethylamine are used.

In some cases, the reaction was carried out under basic pH values, such as the reaction between CD and epichlorohydrin. In each case, the temperature of the reaction ranges from room temperature to reflux temperature of the solvent, and the time is extended to a maximum 48 h. After the complete reaction, the product is allowed to cool down and is washed with distilled water, followed by purification with Soxhlet extraction using ethanol [78]. Interfacial condensation and emulsion solvent diffusion methods are rarely used in CD NS synthesis.

The process of ultrasound-assisted synthesis involves mixing CD and crosslinker in a flask, then placing it in an ultrasonic bath at 90 °C. The procedure generates NSs with uniform size distribution. Heat is used in microwave-assisted synthesis to conduct crosslinking reactions, and this strategy is superior to hot-melt and ultrasound methods due to the controlled heating process. It also reduces the reaction time and enhances the scalability of the reaction. A solvent is usually used, and a catalyst is used when required. Mechanochemical synthesis is a solvent-free method that uses the crosslinking of CD with the help of mechanical energy. Twin screw extruder systems are used in order to overcome the limitations of ball-milling in mechanochemical synthesis [75].

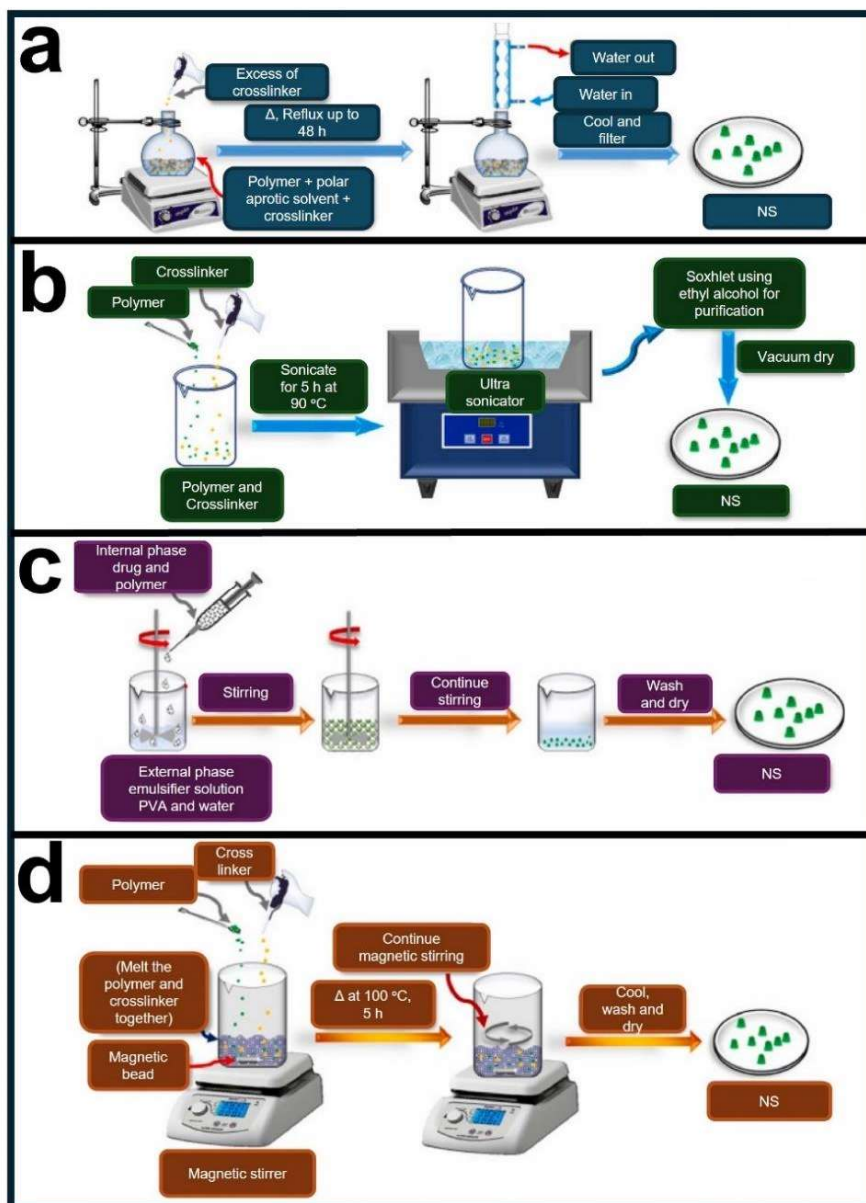


Figure 11. Synthesis of NSs via a) solvent method, b) ultrasound-assisted synthesis, c) emulsion-solvent diffusion and d) melting methods. Adapted from [79] under the terms of the Creative Commons Attribution-NonCommercial-No Derivatives License (CC BY NC ND). Copyright 2023, Cell Press.

1.3.3. Types of Cyclodextrin Nanosponges

CD NSs can be classified into four main groups based on their structure and features. 1st generation NSs are plain NSs, simply formed by crosslinking of CD units with a

crosslinker, and they are divided into four subgroups based on the chemical reaction that they utilized: urethane, carbonate, ester, and ether NSs. The addition of desired features to the plain NSs generated 2nd generation NSs. The 3rd generation NSs are stimuli-responsive and alter their structure against environmental changes. The last group, 4th generation NSs, are molecularly imprinted polymers that specifically detect target molecules [74].

Urethane NSs are generated by crosslinking with diisocyanates and characterized by their rigid structure and low swelling capacity. They are also resistant to chemical degradation and are mostly utilized for the removal of organic pollutants from wastewater. Carbonate NSs have similar physicochemical properties with urethane NSs and are generated by the crosslinking of CDs with DPC, 1,1'-carbonyldiimidazole, or triphosgene. Unlike the urethane-based NSs, carbonate NSs are widely utilized in biomedical areas, including the delivery of hydrophobic and hydrophilic drugs and natural flavonoids, as well as antifungal and anti-inflammatory agents. Ester NSs are generated by the reaction between CDs and dianhydrides or poly carboxylic acids. The common crosslinkers are pyrometric dianhydride (PMDA) and citric acid. Due to the presence of an ester bond in their structure, they are able to hold huge amounts of water and are labile to hydrolysis. These NSs are utilized for the delivery of small molecules and heavy metal absorption. Ether NSs are produced by the crosslinking of CD units with epoxides such as epichlorohydrin. Ether NSs can be water-soluble or insoluble, according to the synthesis parameters, and they are usually resistant to the chemical agents. These NSs are applied in separation processes and biomedical applications [74].

2nd generation CD NSs are generated by the addition of functional groups or moieties to the plain NSs in three different ways. A moiety can be introduced to the NS before (pre-crosslinking), during, and after (post-crosslinking) the synthesis. Homogenous distribution of moieties to the NS structure was obtained with the first two strategies, whereas only the surface is functionalized when post-crosslinking is used to decorate the NS. These functionalities could be the covalent attachment of fluorescent molecules, hydrophobic side groups, or embodying electrical charges [74].

3rd generation CD NSs are composed of a series of stimuli-responsive polymers that alter their structure when exposed to the alteration of the environment. These NSs will be explained in detail in Section 1.3.4.

As the final group, the 4th generation CD NSs are made of molecularly imprinted polymers (MIPs). In the MIP strategy, a polymer network, specifically the MIP, selectively interacts with the target molecule. During crosslinking, CD monomers, crosslinkers, and target molecules, which act as templates with hydrophobic sites, are used. After the reaction is completed, the template molecule is removed, leaving the MIP behind. They are highly selective of their target molecules and bind them through intramolecular interactions. CD NS-based MIPs are used mostly in drug delivery and biosensing applications [74].

1.3.4. Stimuli-Responsive Cyclodextrin Nanosponges

Stimuli-sensitive materials are capable of changing their physical properties when exposed to an external stimulus. Conformational change in the nanocarrier structure as well as the disassembly of the nano system occurs when encountering external and internal changes in temperature, pH, redox status, enzyme, light, ultrasound, and magnetic field. Stimuli-responsive nano systems are engineered to release their cargo on demand with high efficacy at the tumor site while benefiting the intrinsic difference between healthy and tumor tissue. This strategy also minimizes the systematic side effects of several drug molecules. In addition to providing therapy for various conditions, this strategy offers several advantages over traditional modalities in diagnosis [24].

The advantage of using CD NSs in stimuli-responsive systems is their capability of forming host-guest interactions with various small molecules, as well as the encapsulation of hydrophilic drugs. The structure of the CD allows conjugation of various targeting moieties as well. In these systems, the encapsulated molecules are designed to be released by disintegration of CD NSs, mostly through their crosslinkers [74].

The first stimuli-responsive CD NS was generated by the reaction between β -CD, 2-hydroxyethyl disulfide, and PMDA. This NS is glutathione-responsive, destined to release drug molecules in cells with high glutathione content, such as cancer cells, aiming the disintegration of the structure inside the cells [80,81]. The synthesized NS was then used to deliver doxorubicin (Dox) [80,82,83], resveratrol [84], erlotinib [85], and strigolactone analogue, whose release was both glutathione and pH-responsive [86].

pH-responsive CD NS was generated by crosslinking of polyaminocyclodextrins with heptakis-(6-bromo)-(6-deoxy)- β -cyclodextrin [87]. Dual responsive (glutathione and pH) hyper crosslinked CD NS was generated by acryloyl-6-ethylenediamine-6-deoxy- β -Cyclodextrin and *N,N*-bis(acryloyl)-cystamine for the delivery of Dox [88]. Another pH-responsive hybrid CD NS was generated by reaction between β -CD and quantum dots for Dox delivery [89]. Another hybrid system composed of CD NS and gold nanorods for potential near infrared (NIR) delivery was developed for dual drug delivery and showed enhanced activity [90]. These NS will be further evaluated in detail in Section 1.5.

1.4. Cyclodextrin Nanosponges in Drug Delivery

CD NSs, which are crosslinked CD units with nano-sized pores, enable the incorporation of hydrophobic drugs within the CD cavity and hydrophilic drugs in the interstitial space [78]. Applying CD NSs as drug carriers often results in high inclusion stability and encapsulation efficiency. They increase the solubility of anticancer drugs and eliminate fast degradation in the bloodstream, providing enhanced bioavailability. They also protect light-labile compounds. They are also non-toxic and easily produced, which makes them excellent alternatives to the other nanovesicles. The preparation parameters, such as crosslinker type and ratio, type of parent CD and drug, and other parameters, strongly influence the drug loading capacity. The CD NSs incorporated various types of drugs, such as anti-cancer, anti-inflammatory, anti-viral, anti-fungal, and antioxidants, as alternatives to other carriers. Besides, CD NSs allow incorporation of two drugs, one hydrophobic and the other hydrophilic, enhancing the therapeutic efficacy [91]. Thus, they also provide sites for the covalent attachment of targeting ligands, making them suitable as high-efficiency drug carriers [92]. The type of parent CD and crosslinker, their ratio, and the type of drug significantly influence the loading capacity of CD NSs [93].

CD NS-drug complexation can be completed by several methods, shown in Figure 12 [94]. Usually, NS is suspended in aqueous media and mixed with drug solution, allowed to stir for 24 h. Then, the complex is collected and purified, followed by lyophilization to stabilize the complex. The co-evaporation method requires the removal of organic solvent from the drug before the drying process. The kneading method involves mixing NS and

drug powder in a mortar with a suitable amount of solvent, followed by a drying process to obtain a stable complex [94].

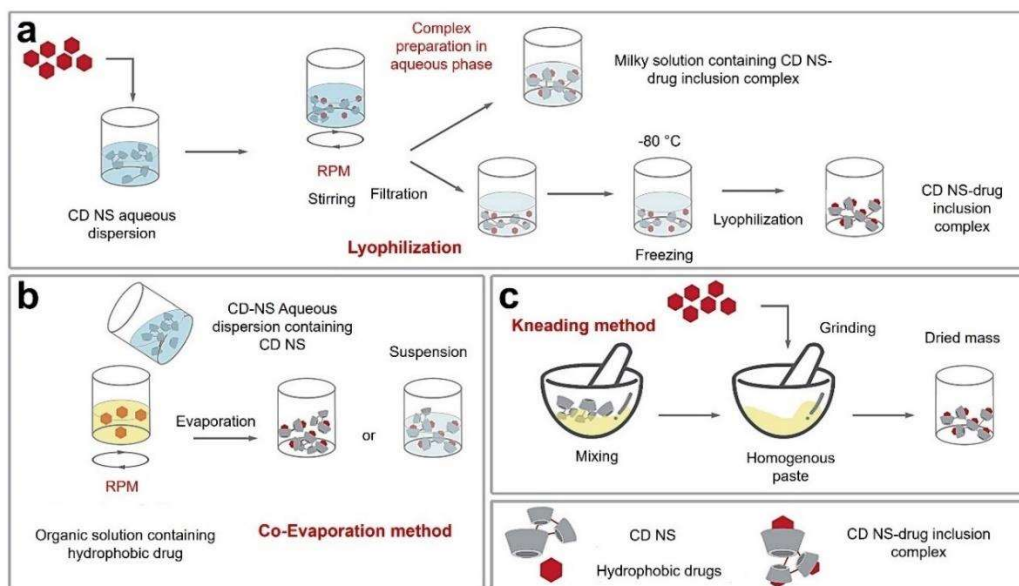


Figure 12. Schematic representation of methods for preparing CD NS drug complexes via a) lyophilization, b) co-evaporation, and c) kneading methods. Adapted with the permission from [94]. Copyright Springer Nature.

Most anti-cancer drugs are hydrophobic, which causes the recrystallization of the drug molecules. They are also small molecules that usually metabolize before reaching the site of action in vivo. Most drugs are not target-specific and generate several side effects. Paclitaxel is a small hydrophobic anticancer drug that has poor solubility (0.5 mg/l) and low bioavailability. For the delivery of paclitaxel, DPC crosslinked β -CD NSs were used. These NSs exhibited high paclitaxel loading capacity, near 99% and the payload of paclitaxel was 500 mg per g of dry NS. Compared to Taxol[®], NS-paclitaxel showed a 3-fold increase in paclitaxel bioavailability when orally administered to the rats [95]. Paclitaxel was also delivered by the carbonyl imidazole crosslinked β -CD NSs as an alternative to the Cremophor EL. NSs did not show hemolytic activity and are non-toxic. They are able to increase the solubility of paclitaxel from 0.5 mg/ml to 2 mg/ml and prevent the recrystallization of it. Encapsulation of paclitaxel reduced the IC50 of paclitaxel while providing enhanced paclitaxel entry to cells. No burst drug release was observed; however, NSs released all encapsulated paclitaxel within 2 h [96]. In another

report, DPC crosslinked β -CD NSs were generated, and paclitaxel was loaded. Similar to previous results, CD NSs enhanced the toxicity of paclitaxel when applied to the MCF-7 breast cancer cell line [97].

Camptothecin, as a plant alkaloid, is another hydrophobic compound exhibiting anticancer activities. It has limited application in cancer therapy due to poor solubility and an unsteady lactone ring. NSs were prepared by reacting β -CD with DPC. NSs exhibited uniform size distribution with the range of 400 nm to 600 nm, and surface potential was found near -22 mV. Encapsulation by NSs provided the protection of the lactone ring from hydrolysis and sustained release of the drug for 24 h, as well as enhanced anticancer activity against colon cancer cells [98]. The antitumor activity of the same NSs with camptothecin was evaluated against androgen-refractory and sensitive cell lines of prostate cancer. The inhibition of topoisomerase I as well as the increased DNA damage and cell cycle arrest compared to bare camptothecin were reported [99]. Increased antiangiogenic and antiproliferative activity of camptothecin-loaded NSs compared to pure camptothecin was also recorded when they were applied *in vivo* [100]. The inhibition of tumor cell adhesion as well as the migration was reported when encapsulated camptothecin was applied to anaplastic thyroid cancer on orthotopic xenograft [101].

Tamoxifen is an anticancer drug used to treat breast cancer that has very limited solubility. Carbonyl imidazole crosslinked β -CD NSs were used to encapsulate tamoxifen. The pharmacokinetic properties of tamoxifen are higher in the encapsulated version compared to tamoxifen citrate. When orally administered, the increase in tamoxifen amount in plasma was obtained compared to tamoxifen citrate alone. Thus, encapsulation by NSs enhanced the toxicity of tamoxifen in MCF-7 breast cancer cells [102].

Temozolomide is a pro-drug and simultaneously activated, exhibiting anticancer activities in gliomas and melanomas. DPC crosslinked β -CD NSs were used to encapsulate temozolomide. The loading of temozolomide into NSs was successfully achieved; however, cell studies against glioma cells revealed no significant difference in viability between encapsulated and pure drugs [103].

Dimethyl carbonate crosslinked β -CD NSs were used to deliver curcumin [104]. Curcumin is a polyphenol that has anticancer activity and has very low solubility. The complexation of curcumin with NSs greatly enhanced the solubility from 0.40 $\mu\text{g/ml}$ to 20.89 $\mu\text{g/ml}$. The prepared complex exhibited 487 nm particle size and -27 mV zeta

potential, resulting in prolonged release of curcumin over time [105]. However, only a slight difference in viability of MCF-7 cells treated with curcumin and NS-curcumin complex was recorded [105]. The effect of crosslinker was also studied for curcumin-loaded NSs. For this purpose, DPC and PMDA were chosen as crosslinkers [106]. Both NSs have nano-sized pores, enabling curcumin entrapment. The solubility increased by 16-fold and 5-fold for diphenyl carbonate crosslinked NSs and PMDA crosslinked NS, respectively, compared to pure curcumin. PMDA crosslinked NS enhanced the photostability of curcumin. *In vitro* studies against MCF-7 cells indicated enhanced toxicity when PMDA was chosen as a crosslinker [107]. Once the amount of PMDA increased, the complexation efficiency and solubilization were decreased in curcumin-loaded NSs [108]. Co-delivery of curcumin with resveratrol was achieved by PMDA crosslinked CD NSs for synergistic anticancer activity against MCF-7 cells. NSs enhanced the release by 10-fold and 2.5-fold of curcumin and resveratrol, respectively. Once incorporated inside the hydrogel base, further enhancements in protection from light degradation and permeation were reported, which can be used in transdermal delivery [109].

Sorafenib is a class II drug used to treat renal cells and hepatocellular carcinomas clinically, which has low bioavailability (8.5%) and solubility (9.86 ng/ml). Epichlorohydrin crosslinked CD was used to encapsulate sorafenib, which significantly increased sorafenib solubility. The complex reduced the proliferation of tumor cells as well as the free drug while reducing the *in vivo* tissue toxicity of free sorafenib [110].

Dox is an anthracycline anticancer drug, having moderate solubility and widely utilized in breast cancer treatment with several side effects, including cardiotoxicity and drug resistance. Therefore, PMDA crosslinked β -CD NSs were used for delivery of Dox. Encapsulation of Dox by NSs activated apoptosis and reduced cancer cell proliferation compared to free Dox. Encapsulation reduced the amount of Dox 5 times lower compared to pure Dox in the reduction of breast cancer when administered to mice. Encapsulation also targeted the tumor tissue, reducing cardiotoxicity [111].

Bortezomib is an anticancer drug that is used to treat myelomas, lymphomas, and breast cancer. Carbonyl imidazole crosslinked NSs were produced with different crosslinker ratios and used to deliver bortezomib. The slow and prolonged drug release was achieved

through encapsulation. NSs also enhanced the permeability of bortezomib through the rat intestine about 5.8-times compared to pure bortezomib [112].

Erlotinib is an anticancer drug and acts as a tyrosine kinase inhibitor, having poor solubility and bioavailability. Carbonyl imidazole crosslinked β -CD NSs with a molar ratio of β -CD to crosslinker of 1:4 was generated to enhance solubility, dissolution, toxicity, and bioavailability of erlotinib. Complexation enhanced the dissolution of erlotinib 2 times compared to pure erlotinib. Cellular uptake of drugs and toxicity increased by the complexation against pancreatic cells, as well as the oral bioavailability of erlotinib [113].

Acetyl salicylic acid, an anti-inflammatory drug that has rapid hydrolysis in the bloodstream, was complexed with PMDA crosslinked β -CD NSs. NS formulations enabled prolonged and slow release of acetyl salicylic acid [114]. This NS was also used to deliver meloxicam, enhancing its solubility and wettability, as well as the increased dissolution. The NS-meloxicam complex was stable up to three months [115]. Acyclovir as an antiviral drug was complexed with carbonyl imidazole-crosslinked CD NSs, which further decorated with carboxyl groups. Decorated NSs exhibited high drug loading and release as well as high anti-viral activity against clinical isolates of Herpes Simplex Virus-1 compared to plain NS [116]. Carbonyl diimidazole and PMDA crosslinked β -CD NSs were used to deliver rilpivirine against Human Immunodeficiency Virus infections. The dissolution rate was enhanced, and a nearly 2-times increase in oral bioavailability of rilpivirine was recorded [117]. DPC crosslinked β -CD NSs were complexed with efavirenz. NSs were able to enhance the solubility of antiviral drugs with high loading capacity. This stable complex showed a 3-fold increase in *in vitro* dissolution and a 2-fold increase in oral bioavailability [118]. This NS also applied with itraconazole delivery, enhancing its solubility almost 50-fold [119]. DPC crosslinked NSs loaded with clotrimazole and placed into an in situ gelling system against vaginal candidiasis. The system provided prolonged drug release compared to the other formulations, enhanced the solubility of the drug, and high in vivo antifungal activity [120]. PMDA crosslinked β -CD NSs were used for the delivery of imiquimod, enhancing its anti-proliferative effect on keratinocyte cells compared to free imiquimod, which could be useful for the treatment of post-burn injuries [121], limiting the proliferation of fibroblasts [122].

Quercetin is a flavonoid found in most vegetables, acting as a strong antioxidant. It also possesses low water solubility and lability to light due to its aromatic structure. CD carbonate NSs with different ratios were used for quercetin complexation. These complexes exhibit ideal sizes (40–100 nm) with uniform size distribution. Encapsulation enhanced the dissolution of quercetin, as well as protecting it from degradation from light while enhancing the antioxidant activity [123,124]. Carbonate CD NSs are functionalized with lactoferrin and loaded with fisetin against breast cancer. NS-fisetin complex exhibited size around 54 nm, a low PDI, and positive Zeta potential (24 mV) due to coating. The encapsulation efficiency was 93% and provided sustained release. Coating further enhanced oral bioavailability and anti-cancer activity compared to blank NS and pure fisetin [125].

1.5. Examples of Smart Cyclodextrin Nanosponges in Drug Delivery

Stimuli-responsiveness is the ability of a material to respond to the presence of stimuli. These stimuli can be light, temperature, magnetic field, ultrasound, enzymes, or chemicals that alter the conformation of materials, yielding re-assembly, swelling, shrinking, or disintegration [126]. This phenomenon is specifically useful for the designing of cancer therapeutics and diagnostics, whereby the tumor niche has different biological and physicochemical properties than the normal tissues.

Over the last years, CD NSs have been generated as stimuli-responsive materials. The first example of responsive CD NS is glutathione-responsive NS (GSH-NS). GSH-NS was synthesized in a one-step reaction between β -CD, 2-hydroxyethyl disulfide, and PMDA (Figure 13) [83]. Then, Dox was incorporated into this sponge as a model drug and proposed to release Dox in cells with high GSH content by cleaving the disulfide bond in GSH-NS provided by 2-hydroxyethyl disulfide. These NSs were also prepared by the different sulfur content by varying the amount of 2-hydroxyethyl disulfide. However, the content of sulfur was less than the expected value in GSH-NS, due to the different reactivity of β -CD and 2-hydroxyethyl disulfide against PMDA. Dox release was reported to be GSH-dependent, as the amount of released Dox was directly proportional to the amount of GSH used. The cell viability assay was performed on different tumor cells. These cells exhibit different GSH content (μg per mg protein) as

7.02 for HCT15, 11.52 for HepG2, and 5.64 for A2780. Higher cell inhibition was observed when GSH-NS-Dox was used against HepG2 cells due to enhanced cellular GSH content. Cell viability was also reported to be concentration- and time-dependent. Low drug doses of free Dox and GSH-NS-Dox were found to be more effective at killing the cells for prolonged time compared to high doses [82]. The potential of GSH-NS-Dox was further evaluated with DU145 and PC-3 prostate cancer cells and HCT116 and HT-29 colon cancer cells. Compared to free Dox, GSH-NS-Dox was able to enhance DNA damage and reduce topoisomerase II activity, clonogenic growth, and cell viability in cells with high GSH content, such as DU145 and HCT116. Dox-GSH-NS was able to increase the internalization of Dox compared to free Dox in all cells revealed by the confocal measurement. Dox-GSH-NS was tested *in vivo* against DU145 xenograft tumor. Results pointed out that GSH-NS-Dox was able to inhibit tumor growth compared to free Dox, reducing the cardiotoxicity of free Dox when administrated to the mice [83]. The effectiveness of GSH-NS-Dox was also proved by using multicellular spheroids of HCT116 and DU145 cells having high GSH content [81]. Hepatotoxicity of GSH-NS was tested against human HepG2, and *ex vivo* rat precision-cut liver slices. It was proved that GSH-NS-Dox has comparable hepatotoxicity than the free Dox [80].

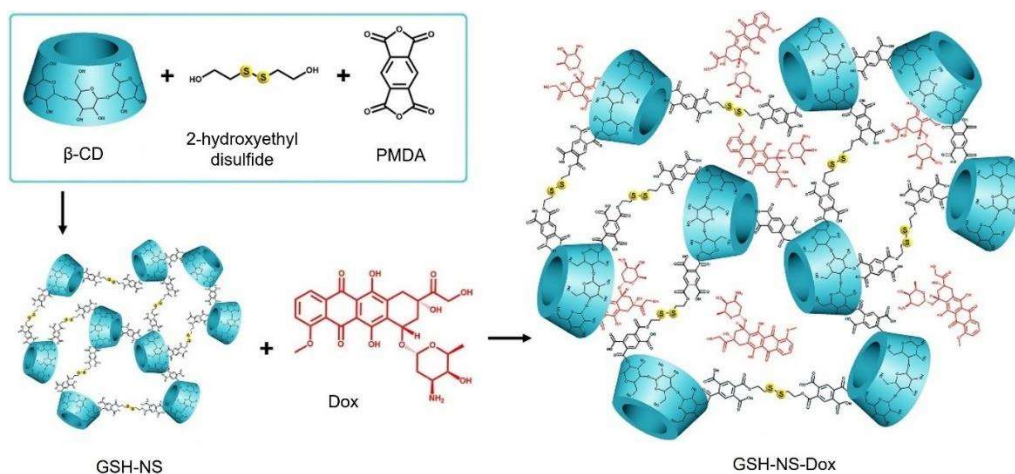


Figure 13. Schematic representation of synthesis of GSH-NS from β -CD, 2-hydroxyethyl disulfide and pyromellitic dianhydride, followed by Dox loading. Adapted with the permission from [80]. Copyright 2020, Elsevier.

Resveratrol-loaded GSH-NS were generated in order to enhance the therapeutic efficiency of resveratrol. GSH-NS showed high drug encapsulation (81.64%), and

resveratrol release was dependent on the external GSH content. Blank GSH-NS were not toxic to the human fibroblasts, which is dose-independent, and they are internalized mainly through tumor cells exhibiting the selective toxicity of GSH-NS-resveratrol [84]. Erlotinib-loaded GSH-NS were tested against lung cancer cells, namely A549 cells. GSH-NS was able to increase the toxicity of erlotinib, and tumor inhibition was recorded to be enhanced by almost 2-fold compared to free erlotinib when applied to the BALB/c mice [85]. GSH-NS was also used to deliver strigolactone analogues, and the release of both drugs was both glutathione and pH-responsive [86].

A new type of polyaminocyclodextrins was introduced by the reaction between polyaminocyclodextrins and heptakis-(6-bromo)-(6-deoxy)- β -CD. The ability of this type of NS was investigated in terms of adsorption of small molecules, where the adsorption was dependent on the pH of the environment. This type of NS was not studied for the drug delivery [87]. Dual responsive (pH and GSH) CD NSs were generated by the reaction between acryloyl-6-ethylenediamine-6-deoxy- β -CD (β -CD-NH-ACy), acrylic acid (AA), and *N,N*-bis(acryloyl)-cysteinamine (BACy). The synthesis of β -CD-NH-ACy was completed in 3 steps, and the synthesis of BACy was done in 2 steps. After that, β -CD-NH-ACy, BACy, and AA were polymerized to obtain hyper-crosslinked CD polymers (Figure 14.a). Chemical characterizations were conducted on NS, showing successful synthesis as well as the Transmission Electron Microscopy (TEM) analysis (Figure 14.b). Dox was incorporated into this system (NS-Dox) in order to test responsive drug delivery, whereby the release of Dox was altered by both GSH and pH change. The internalization of Dox-NS was evaluated with A549 cells, showing the accumulation of Dox through the nucleus of the cells over time (Figure 14.c.) [88].

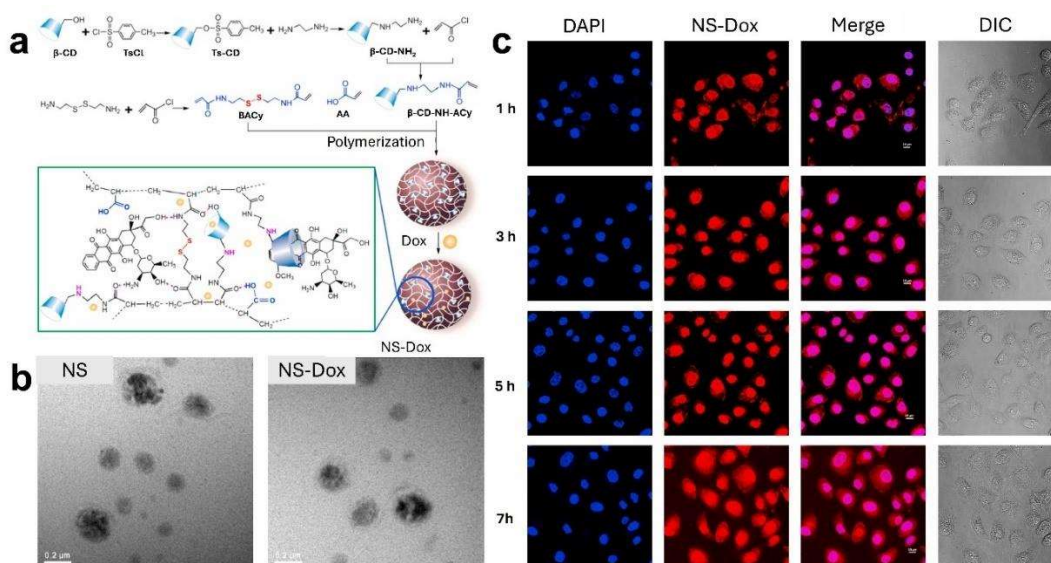


Figure 14. a) Synthesis of dual-responsive CD NS (TsCl: p-toluenesulfonyl chloride, Ts-CD: 6-mono-(p-toluenesulfonyl)- β -CD, β -CD-NH₂: mono-(6-ethylenediamine-6-deoxy)- β -CD, β -CD-NH-ACy: acryloyl-6-ethylenediamine-6-deoxy- β -CD, BACy: N,N-bis(acryloyl)cystamine, AA: acrylic acid), b) TEM images of NS and Dox-loaded NS (NS-Dox), c) Confocal images A549 cells incubated with Dox- loaded NS(NS-Dox) for different time. DAPI was used to label the nucleus of the cells. Adapted with the permission from [88]. Copyright 2021, Elsevier.

A different type of pH-responsive CD NS was generated by the polymerization of quantum dots with β -CD. pH-responsive controlled release of Dox was achieved. This NS was internalized by the HepG2 cells, and Dox accumulation to nuclei was reported [89]. Another hybrid system composed of CD NS and gold nanorods for potential NIR delivery was developed for controlled dual drug delivery (melphalan and curcumin) [90].

Another type of smart NP system is composed of targeted NP, specifically having functional molecules on their surface for specific delivery of the cargo. These NPs can effectively and efficiently transport a variety of anti-cancer drugs, nucleic acids, imaging molecules, photosensitizers, photothermal agents, and other biomolecules. They can be customized to transport their load to the tumor site through diverse surface functionalization, tumor microenvironment-responsive mechanisms, or intrinsic targeting capabilities. Consequently, the application of tumor-targeting NPs facilitates increased drug concentration at the targeted location, improved penetration into cancer cells, and

augmented therapeutic efficacy, resulting in elevated cytotoxicity towards tumor tissues while minimizing harm to healthy tissues [127].

For CD NSs, folic acid (FA) and cholesterol decorations were applied to enhance the therapeutic efficiency. FA serves as one of the most effective ligands for the selective localization of therapeutic or diagnostic agents within cancer cells due to the overexpressed folate receptors on various cancer types. A novel theranostic system was developed utilizing CD NS linked to the surface of magnetite (Fe_3O_4) NPs, subsequently functionalized with FA as a targeting agent (Fe_3O_4 -CD NS-FA) and used for delivery of curcumin. The synthesized NS has uniform size distribution and a spherical shape. It was reported that curcumin release was sensitive to environmental pH; an increase of 1.67-fold of curcumin was found when pH was switched from 7.4 to 5.5. The toxicity assays revealed that blank Fe_3O_4 -CD NS-FA has negligible toxicity, while the Fe_3O_4 -CD NS-FA-Curcumin complex had significant toxicity against folate-overexpressing cancer cells [128].

In another report, cholesterol functionalization was applied to enhance uptake of CD NS through cells. DPC crosslinked CD NSs was generated, followed by cholesterol hydrogen succinate (CHS) grafting (CD NS-CHS). Dox was entrapped with CD NS-CHS as a model drug. CHS modification enhanced cellular uptake of CD NS-CHS-Dox in HeLa cells since cholesterol is available on the surface of all cell types[129].

1.6. Aim of the Study

The aim of this study is to develop novel smart targeted pH-responsive cyclodextrin nanosponges. For this purpose, oxidized β -CD was crosslinked with adipic acid dihydrazide via nucleophilic addition, forming pH-responsive CD NS for the first time. With this novel strategy, pH-labile hydrazone bonds were generated inside the CD NS, which degraded under acidic pH values. Such smart systems can be designed to delivery drugs in tumor niche with several stimuli; however, pH-responsive systems benefit intrinsic physiological property of tumor microenvironment and eliminates the use of external stimuli. The potential of pH-responsive CD NS in doxorubicin delivery was evaluated. To enhance specific uptake of NS by cancer cells, folic acid was conjugated to

the surface of NS. The physicochemical properties of the fabricated sponge were then assessed using different analyses, including FTIR, DLS/Zeta, UV-Vis, SEM, TEM, XRD, TGA, and DSC. After that, the amounts of drug loading and release pattern (in two different conditions) were evaluated as well. In the final part, biological features of the fabricated system were assessed via determining its effect on viability of cells (both cancer and normal cell lines) and cellular uptake mechanism.

2. Materials and Methods

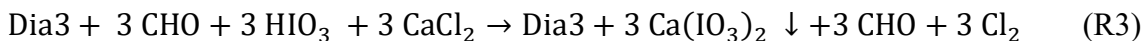
2.1. Materials

β -cyclodextrin hydrate (β -CD, CAS number: 68168-23-0, 23387) and doxorubicin hydrochloride (Dox, CAS number: 25316-40-9, 15007) were received from Cayman, Michigan, USA. Sodium periodate (NaIO_4 , CAS number: 7790-28-5, S1878), adipic acid dihydrazide (ADH, CAS number: 1071-93-8, A0638), tissue culture grade water (CAS number: 7732-18-5, W3500), ethylene glycol (anhydrous, CAS number: 107-21-1, 324558), folic acid (FA, CAS number: 59-30-3, F8890) and *N*-(3-Dimethylaminopropyl)-*N'*-ethyl carbodiimide hydrochloride (EDC, CAS number: 25952-53-8, E6383) were received from Sigma-Aldrich, Missouri, USA. 4-(Dimethyl amino) pyridine (DMAP, CAS number: 1122-58-3, 107700), hydroxylamine hydrochloride (CAS number: 5470-11-1, 159417), calcium chloride dihydrate (CaCl_2 , CAS number: 10035-04-8, 223506), dimethyl sulfoxide (DMSO, CAS number: 67-68-5, 472301), phosphate buffer saline tablets (PBS, OmniPur[®], Calbiochem, UNSPSC Code:12161700, 6500OP), sodium hydroxide (NaOH, CAS number: 1310-73-2, 221465), and thiazolyl blue tetrazolium bromide (MTT, CAS number: 298-93-1, M5655) were supplemented from Merck, Darmstadt, Germany. 500 Da cut-off dialysis membrane (MD25) was from Janques labware, China, while 6-8 kDa cut-off dialysis membrane (Spectra/Por[®]1, 1326555) was from Repligen, Massachusetts, USA. Dulbecco's modified Eagle's medium (DMEM, P04-03590), fetal bovine serum (FBS, P30-3306), penicillin-streptomycin (pen/strep, P06-07050), trypsin-EDTA (P10-0231SP), Dulbecco's PBS (DPBS, P04-36500) were received from PAN Biotech, Aidenbach, Germany. MCF-7 and L929 cell lines were gifted from Nanotechnology Research & Application Center, Sabanci University, Istanbul, Turkey.

2.2. Methods

2.2.1. Synthesis of Oxidized β -Cyclodextrin

The vicinal diols of β -CD were transformed into aldehydes by interacting with NaIO_4 to complete the oxidation of β -CD (Figure 15) [72]. To this end, 200 mg of β -CD was dispersed in 2.2 ml of distilled water, followed by the addition of 66.4 mg of NaIO_4 to the reaction mixture. The reaction tube was sealed with aluminum foil to prevent light-induced degradation of NaIO_4 . The reaction was conducted for 1 h at ambient temperature with continuous stirring at 800 rpm. Upon completion of the reaction, 528 μl of ethylene glycol was introduced to terminate the reaction. Following 20 min of stirring, 29.1 mg of CaCl_2 was introduced to the reaction mixture to facilitate the precipitation of iodate. After 10 min, the supernatant was separated by centrifugation at 15,000 rpm for 10 min and then dialyzed against distilled water for 4 h using a 500 Da cut-off dialysis membrane, with the water being replenished every hour. The sample was subsequently freeze-dried at -96°C at 0.001 atm pressure for 48 h in order to future utilization and stored at -20°C . The oxidized β -CD was designated as Dia3, indicating dialdehyde β -CD with 3 oxidized units out of 7, with a molar ratio of β -CD to NaIO_4 of 1:3. The molar ratio of NaIO_4 to ethylene glycol to CaCl_2 was 1:1:1. The reactants and products for the oxidation process are listed in Reactions 1-3.



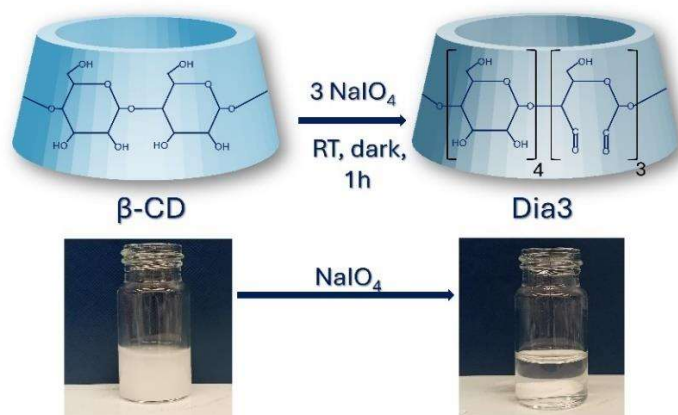


Figure 15. The schematic representation of β -CD oxidation. 3 out of 7 glucopyranose units were oxidized with NaIO_4 . Digital images for β -CD (left) and Dia3 (right) in water.

2.2.2. Synthesis of Nanosponges

CD NSs were produced through the interaction between the aldehyde of Dia3 and the hydrazide groups of ADH (Figure 16) [130]. This is a nucleophilic addition process that generates hydrazone bonds, which are cleaved under acidic pH [131]. Simply, 50 mg of Dia3 was dissolved in 1 ml of tissue culture-grade water and stirred for 10 min. Concurrently, ADH was dissolved in 4 ml of water and then added to the Dia3 solution. The reaction was performed for 48 h at a stirring speed of 1000 rpm. For the optimization of the production process, NS with the same molar ratio of aldehyde to ADH was chosen (named as NS3:1). NS3:1 was prepared by reacting 50 mg Dia3 and 32.6 mg Dia3 as indicated above. After mixing at room temperature and stirring at 1000 rpm, in each time intervals (0 h as start point followed by 2 h, 4 h, 6 h, 8 h, 10 h, 24 h, 30 h, 45 h, 48 h), the hydrodynamic size (Z-average, nm), PDI and Zeta potential of the NS3:1 were recorded using ZetaSizer and outlined in Table 5 in Section 3.2.1.

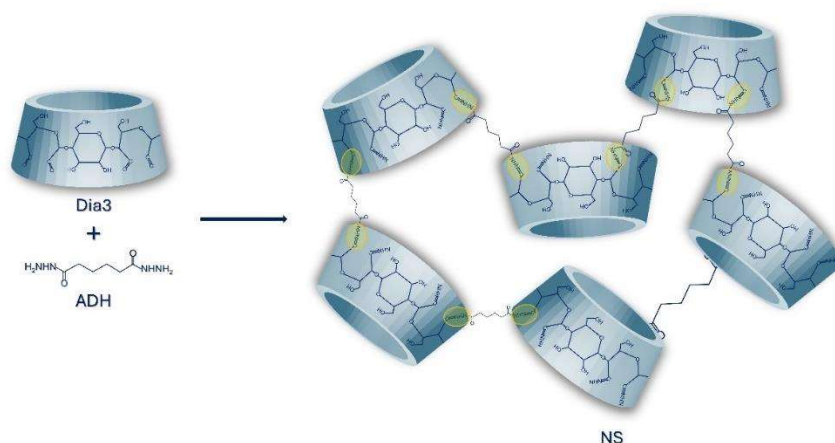


Figure 16. The schematic representation of NS synthesis through the reaction between Dia3 and ADH, forming hydrazone bonds (shown in yellow circles).

After 48 h, a cloudy solution of NS3:1 formed (Figure 17.a). The reaction was then concluded using several steps. First, acetone (in a 4:1 ratio to the reaction mixture) was added to precipitate NS3:1. This method was chosen because acetone effectively precipitates crosslinked CD polymers, a technique similarly used in the synthesis of epichlorohydrin crosslinked CD NS [132]. The sample was then centrifuged at 15,000 rpm for 15 min to separate NS3:1, which settled at the bottom of the tube (Figure 17.b). Next, the precipitate of NS3:1 was transferred to a glass dish and placed in an oven at 110 °C for 30 min to evaporate any remaining acetone and water, a method also applied in the synthesis of citric acid-crosslinked CD NS [133]. Afterwards, the resulting white powder was scraped from the glass dish, by adding 1 ml of acetone followed by 4 ml of water. This NS3:1 solution was then dialyzed for 24 h in distilled water using 6-8 kDa cut-off dialysis membrane to remove unbound reactants (Figure 17.c). After dialysis, the sample was subsequently freeze-dried at -96 °C at 0.001 atm pressure for 48 h for long-term storage at 4 °C (Figure 17.d). At each step, the hydrodynamic size (Z-average, nm) and PDI of NS3:1 were measured using a ZetaSizer and displayed alongside the corresponding steps in Figure 17. Before measurement, samples were diluted 1:10 with distilled water, while a 1 mg/ml dispersion was prepared for dry samples. Each specimen was sonicated for 30 min and filtered through 0.22 µm filter. Hydrodynamic size and PDI were recorded using disposable cuvettes.

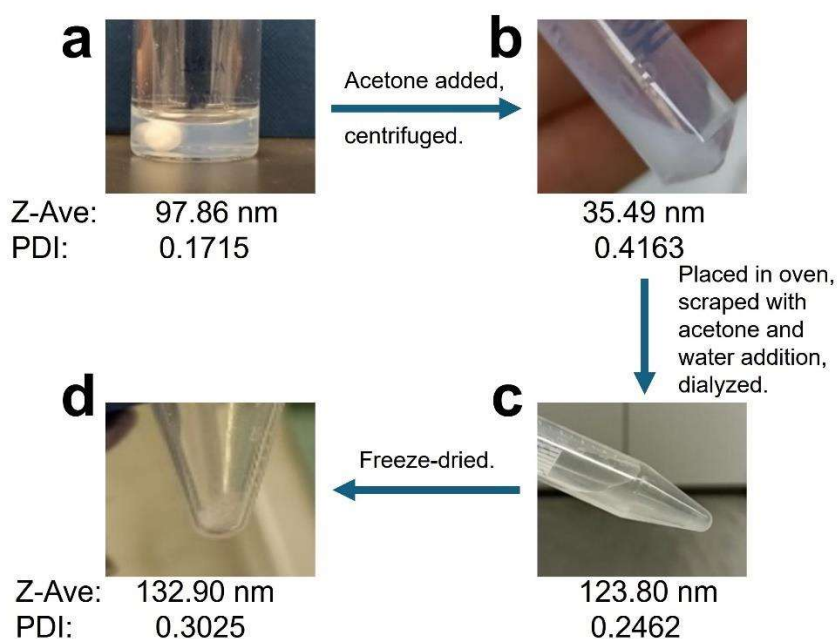


Figure 17. Digital images, Z-Average (nm) and PDI values for NS3:1 at a) 48 h in blurry solution, b) after acetone addition and centrifuge, c) after placing in oven, acetone and water addition followed by scraping and dialysis and d) freeze-dried forms.

After the optimization of production process, NS with different crosslinker ratio was generated using same method. The amount of the Dia3 and ADH used for these sponges are outlined in Table 3.

Table 3. The amount of Dia3, ADH and molar ratio of [CHO] to ADH of prepared NSs. [CHO] indicates the aldehyde molar ratio.

NS	[CHO]:ADH ratio	Dia3, mg	ADH, mg
NS3:05	1:0.5	50	16.3
NS3:1	1:1	50	32.6
NS3:2	1:2	50	65.2

2.2.3. Doxorubicin Loading to the NSs

Dox was loaded into the NS with varying ratios. Initially, a Dox-to-NS weight ratio of 2:5 was selected [134]. The amount of Dox was then reduced from 2 mg to 1 mg and 0.5 mg per 5 mg of NS. This reduction was necessary due to Dox's solubility characteristics: although Dox is water-soluble at 10 mg/ml, its solubility is limited in a PBS:DMSO mixture (0.5 mg/ml), where it tends to form precipitates through dimerization in PBS [135]. Additionally, our NS formulations also precipitate in PBS. Since drug loading and release studies are conducted in PBS, any free but precipitated Dox could introduce inaccuracies, while a higher drug load (e.g., 2 mg in our study) might further impact the release behaviour. Dox loading was carried out in DMSO:PBS mixture by dispersing the NS sample (5 mg) in 3 ml of PBS and dissolving Dox (0.5, 1 and 2 mg) in 2 ml 1:4 DMSO:PBS mixture. The Dox solution was added to the NS suspension and stirred at high rpm under dark conditions at room temperature for 24 h. The Drug-loaded NSs were then collected by centrifugation (15,000 rpm, 15 min) and meticulously washed three times with distilled water, with centrifugation performed after each wash. The supernatant was collected and analyzed for Dox content to determine the amount of encapsulated Dox. The precipitate was subsequently freeze-dried to enhance the stability of the complex and stored at -20 °C. The concentration of Dox in PBS was quantified using an RF-6000 Spectrofluorophotometer (Shimadzu, Japan) with a standard curve for the Dox. The excitation and emission wavelengths for Dox were established at 480 nm and 595 nm, respectively [80].

Encapsulation efficiency (EE%) and loading capacity (LC, mg/mg) for NS was determined by Equations 1 and 2, as described below [111]:

$$EE\% = \frac{(\text{Amount of total Dox} - \text{amount of free Dox})}{\text{Amount of total Dox}} \times 100 \quad (1)$$

$$LC = \frac{(\text{Amount of total Dox} - \text{amount of free Dox})}{\text{Amount of NS}} \quad (2)$$

2.2.4. Folic Acid conjugation to NS3:1

FA was conjugated to the optimized NS (i.e., NS3:1). The conjugation is done to enhance cellular uptake of the NS via receptor mediated endocytosis of cancer cells, which embody folate receptors all over their surface [136]. NS3:1 was reacted with FA through esterification reaction, which the free hydroxyls on the β -CD units of NS3:1 was reacted with carboxylic acid groups of FA via DMAP and EDC [89,137] (Figure 18). For this reason, 8 mg FA was dissolved in 1 ml DMSO. 8 mg NS3:1, 8 mg EDC and 30 mg DMAP were dissolved in distilled water and added to the FA solution.

The reaction vessel was covered with aluminum foil and allowed to stir for 48 h at room temperature in dark. Upon completion of the reaction, the solution was centrifuged and washed with DMSO to remove unbound FA followed by washing with distilled water to eliminate residual impurities. The supernatant was collected and analyzed for unbound FA using a T80+ UV-Visible Spectrophotometer (pg instruments, UK). The conjugate was then dialyzed against distilled water for 48 h and subsequently freeze-dried for further use.

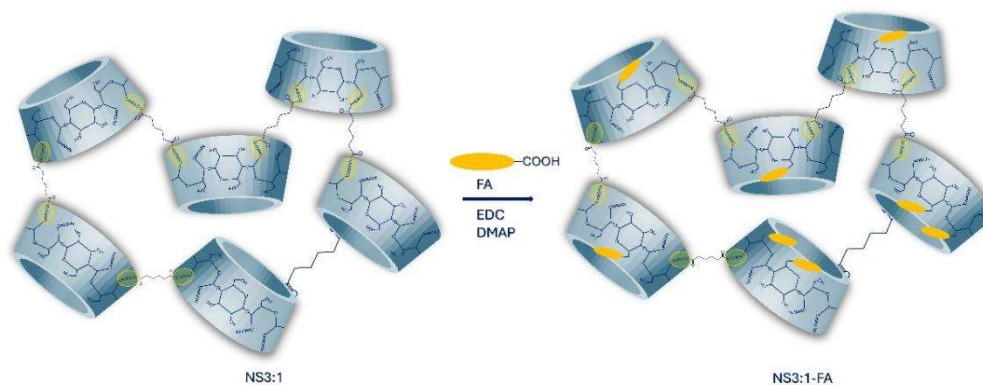


Figure 18. The schematic representation for FA conjugation to NS3:1.

2.2.5. Preparation of Physical Mixtures

Physical mixtures of the specimens were prepared by mixing the same amount of reactants before their interaction, using mortar and pestle. Each physical mixture was prepared just before the analysis.

2.2.6. Aldehyde Content Determination

The potentiometric titration method was used to determine aldehyde concentration of Dia3. Aldehyde groups react with hydroxylamine hydrochloride, generating hydrochloric acid (HCl), which is then titrated with a NaOH solution [72]. Briefly, 12.5 ml of hydroxylamine hydrochloride solution (0.25 mol/ml) was used to dissolve 50 mg of Dia3, and the mixture was continuously stirred for 2 h. A 0.05 M NaOH solution was used to titrate the solution until the pH reached 5.0. A titration curve was plotted with pH on the ordinate and the volume of NaOH consumed on the abscissa. The first derivative of the curve was calculated, and the volume of NaOH used was identified by the curve's peak value. The aldehyde content was determined by Equation 3:

$$[\text{CHO}] = \frac{V_{\text{NaOH}} C}{m} \quad (3)$$

Where [CHO] is the aldehyde content (mmol/g), V_{NaOH} is the volume of NaOH where the peak value of differential curve, C is the concentration of NaOH (mol/l), and m is the mass of Dia3 (g) [72].

2.2.7. ¹H-NMR Analysis

Proton Nucleic Magnetic Resonance (¹H-NMR) spectra of β-CD and Dia3 were obtained in D₂O and DMSO-*d*₆, respectively, using Varian VNMRs 600MHz NMR Spectrophotometer (USA). MestReNova software was used to analyze the spectra, and chemical shifts are expressed in parts per million (ppm) with respect to the reference standard of the residual solvent peaks.

2.2.8. FTIR Analysis

Fourier Transform Infrared (FTIR) analysis was performed using an IRAffinity-1S Fourier Transfer Infrared Spectrophotometer (Shimadzu, Japan) equipped with an Attenuated Total Reflectance (ATR) unit. Dry samples were positioned, and spectra were

recorded in the range of 4000 cm^{-1} to 600 cm^{-1} . The scan count and resolution were set to 32 and 4 cm^{-1} , respectively.

2.2.9. Size and Zeta Potential Measurements

The size and Zeta potential of the samples were measured using the Dynamic Light Scattering (DLS) technique with a Zetasizer Pro (Malvern Panalytical, UK) instrument. The samples were prepared by dispersing dry samples in distilled water (1 mg/ml) or by diluting the suspensions (1:10), followed by sonication for 30 min. The samples were then filtrated using a $0.45\text{ }\mu\text{m}$ filter prior to measurement. Disposable cuvettes were used for DLS measurements, and electrophoretic cells were employed for Zeta potential analysis. Each measurement was performed in triplicate.

2.2.10. XRD Analysis

X-ray diffraction (XRD) analysis was conducted on dry samples using a Bruker D8 X-ray diffractometer (Germany) set to operating parameters of 40 kV and 40 mA. Spectra were recorded from 10° to 60° (2θ) with the increment of 2° per min and step size of 0.02° . Eva software was used to analyze the data.

2.2.11. TGA Analysis

Thermogravimetric analysis (TGA) was conducted on the specimens using a Shimadzu DTG-60H (Japan) instrument to evaluate the thermal behavior of the samples. To this end, 2-3 mg of dry specimen was loaded into the alumina crucible and placed in the device. Each analysis was performed under a nitrogen atmosphere (100 ml/min), from 25°C to 500°C with an increment of $10^\circ\text{C}/\text{min}$.

2.2.12. DSC Analysis

Differential Scanning Calorimetry (DSC) was performed using a Thermal Analysis MDSC TAQ2000 (USA). Dry samples were placed in aluminum hermetic pans, and DSC analysis was carried out under a nitrogen atmosphere with a 50 ml/min flow rate. Measurements were performed over a temperature range from 25 °C to 500 °C, with a heating rate of 10 °C/min.

2.2.13. TEM Analysis

Transmission Electron Microscopy (TEM) analysis was carried out via a JEOL-JEM ARM200CFEG UHR-TEM (Japan). Prior to the analysis, 10 µl of NS suspension (just after the synthesis) in water was added onto a lacey copper grid with a 200-mesh size and allowed to dry at room temperature for 1 day. Imaging was performed at an accelerating voltage of 200 kV.

2.2.14. SEM Analysis

Scanning Electron Microscopy (SEM) analysis was performed using a Zeiss Leo Supra 35VP SEM-FEG (Germany). Briefly, freeze-dried samples were mounted onto carbon tape affixed to an SEM pin. The samples were then coated with gold-palladium using a Cressington 108 sputter coater at 40 mA for three 40-second cycles. Secondary electron micrographs were acquired at an accelerating voltage of 3.00 kV using an IN-Lens detector.

2.2.15. Fluorescence Spectroscopy

The concentration of Dox was measured using an RF-6000 Spectrofluorophotometer (Shimadzu, Japan). In brief, 100 µl of Dox solution was added to a fluorometer quartz

cuvette and placed in the instrument. The excitation and emission wavelengths were set to 480 nm and 595 nm, respectively [138]. A calibration curve (Figure 19) was generated and utilized to quantify the unknown concentration of Dox.

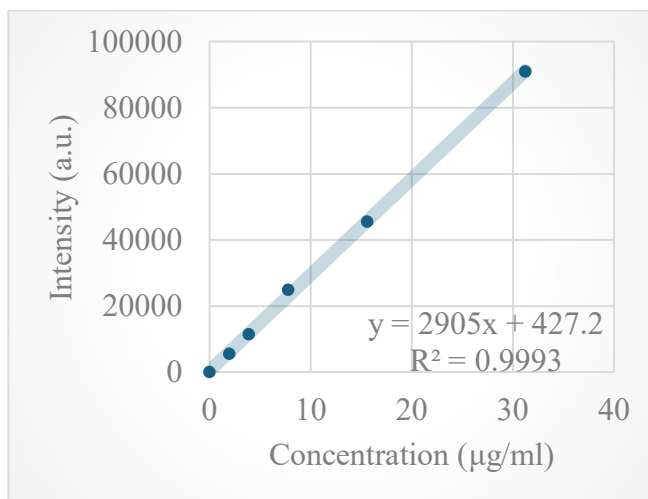


Figure 19. Calibration curve for Dox in water.

2.2.16. UV-Vis Analysis

UV-Vis analysis was performed in order to determine the conjugation ratio of FA. The analysis was performed using a T80+ UV-Visible Spectrophotometer (pg Instruments, UK). 1 ml of solution was placed in a semi-quartz cuvette, followed by the measurements. A calibration curve for FA was generated (Figure 20) to determine the amount of FA. For the calibration curve, FA was dissolved in DMSO, and absorbance was recorded at 288 nm [139].

Conjugation ratio for FA was calculated with Equation 4, by measuring the amount of free FA in supernatant [140].

$$\text{Conjugation ratio} = \frac{(\text{The Amount of Used FA} - \text{The Amount of Free FA})}{\text{The Amount of Used FA}} \times 100 \quad (4)$$

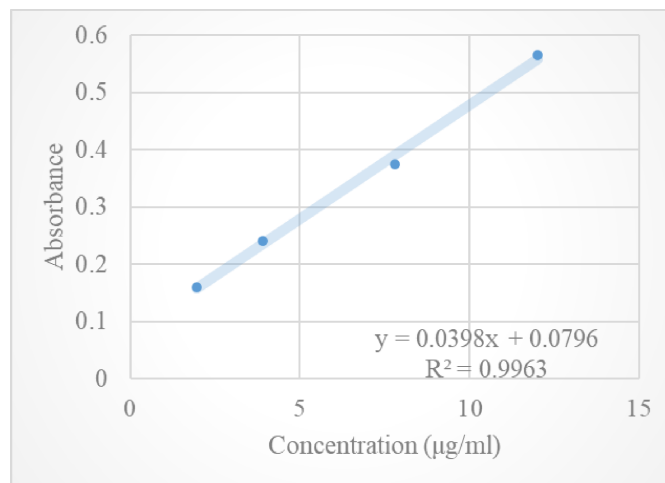


Figure 20. Calibration curve for FA in DMSO.

2.2.17. pH-responsiveness and long-term stability of NS3:1

pH-responsiveness of NS3:1 was assessed by measuring the hydrodynamic size of the samples at varying pH levels. For this purpose, 1 mg of NS was suspended in 2 ml of PBS at pH values of 7.4, 6.5, and 5.5, then incubated at 37 °C for 48 h in a shaking incubator set to 200 rpm. DLS measurements were subsequently performed [141]. Long-term stability of NS3:1 was carried out by measuring the hydrodynamic size of NS3:1 suspended in water (1 mg/ml) and stored at 4 °C over weeks. In predetermined time intervals, DLS measurements were carried out to determine hydrodynamic size. Prior to measurements, samples were sonicated for 30 min, followed by filtration using a 0.45 µm filter. Disposable cuvettes were used for DLS measurements. Each measurement was performed in triplicate.

2.2.18. Drug Release Investigations

In vitro drug release was conducted using the centrifuge technique [142]. For this purpose, 0.5 mg of NS-Dox was dispersed in 2 ml of PBS with corresponding pH values (7.4, 6.5, and 5.5). For the release, samples were placed into a shaking incubator (37 °C, 180 rpm) and allowed to release the Dox. In predefined time intervals (1, 2, 4, 8, 12, 24, 48, and 72

h), samples were centrifuged (15,000 rpm, 5 min), and the supernatant was replaced with fresh PBS [143]. Supernatants were collected and measured using a fluorescence spectrophotometer for Dox content. The amount of released drug (%) was calculated by the ratio of released drug to encapsulated drug.

2.2.19. *In vitro* MTT Assay

The MTT assay was performed on MCF-7 human breast cancer cells and L-929 mouse fibroblast (with the passage number ranging from 20 to 25). Prior to analysis, each cell line was cultured in DMEM containing 10% FBS and 1% pen/strep, passaged using Trypsin-EDTA, and maintained at 37 °C under a 5% CO₂ atmosphere. For the MTT analysis, cells were seeded in a 96-well plate at a density of 10,000 cells per well and allowed to grow for 16 h at 37 °C with 5% CO₂. The NS3:1, NS3:1-FA, NS3:1-Dox, and NS3:1-FA-Dox formulations, along with Dox, were dispersed or dissolved in cell media at concentrations corresponding to free and encapsulated Dox (ranging from 8 to 0.125 μM). Media containing the samples were added to the wells, followed by 24 h and 48 h incubation periods, after which the MTT assay was performed. For this purpose, a 5 mg/ml MTT solution was prepared in DPBS. Cells were washed twice with DPBS, and 100 μl of fresh DMEM was added to each well. Then, 10 μl of MTT solution was added to each well, and the plates were covered with aluminum foil before incubation for 4 h at 37 °C. Following incubation, the MTT-containing media was removed, and 100 μl of DMSO was added to each well to dissolve formazan crystals, and the plates were incubated for an additional 30 min to solubilize formazan crystals. Each well was gently mixed by pipetting, and the absorbance was measured at 570 nm using an Infinite M200 PRO plate reader (Tecan, Sweden) [144,145]. The half-maximal inhibitory concentration (IC₅₀) for each specimen was determined by plotting cell viability (%) on the y-axis and concentration on the x-axis [111].

2.2.20. Confocal Microscopy

Confocal Laser Scanning Microscopy (CLSM, LSM 710, Axio Observer, Zeiss, Oberkochen, Germany) equipped with Zeiss Zen Software (version 2010) was used to visualize cellular internalization of free and encapsulated Dox formulations in MCF-7 cells. For this purpose, cells were seeded at a density of 100,000 cells/ml onto a confocal dish and incubated overnight at 37 °C under 5% CO₂ to allow for attachment and growth [111]. Cells were then treated with 1 μM free Dox (0.575 μg/ml) or encapsulated Dox (10 μg/ml for NS3:1-Dox and 12 μg/ml for NS3:1-FA-Dox) in complete media. After 2 h and 6 h of incubation periods at 37 °C under 5% CO₂, cells were washed three times with DPBS. Subsequently, a 5 μg/ml Hoechst solution in DPBS was added to cover the cells, followed by a 30 min incubation in the dark to stain the nuclei [146]. After incubation, cells were washed and imaged using CLSM via Plan Apochromat 20X/0.8 M27 objective. Excitation and emission wavelengths were set to 405/491 nm for Hoechst and 488/543 nm for Dox.

2.2.21. Cellular Uptake Studies

Spectroscopic measurements of cellular uptake of Dox formulations were performed on MCF-7 cells. This technique enables us to quantify the amount of free Dox and encapsulated Dox internalized by the cells. For this reason, cells were seeded on 96-well plate having 10,000 cells per well, allowed to grow for 16 h at 37 °C with 5% CO₂. Cells were then treated with 1 μM free Dox (0.575 μg/ml) or encapsulated Dox (10 μg/ml for NS3:1-Dox and 12 μg/ml for NS3:1-FA-Dox) in complete media. After 2 h and 6 h of incubation periods at 37 °C under 5% CO₂, cells were washed three times with cold-PBS 3 times and lysed with DMSO (200 μl per well) [147]. After lysis for 30 min, the cell lysates were collected and centrifuged at 14,000 rpm for 20 min. The fluorescence intensity of Dox was measured with fluorescence spectrophotometer and excitation and emission wavelengths were set to 480 nm and 595 nm, respectively. Meanwhile, the lysates of untreated cells were also obtained to eliminate background fluorescence and to obtain calibration curve for Dox, NS3:1-Dox and NS3:1-FA-Dox in cell lysate in order to determine precise amount of Dox formulations in cell lysates [148]. Furthermore, the

number of the cells at 2 h and 6 h was also counted in both control and sample treated wells, and the change in the cell number was reported to be negligible (data not shown). After acquisition of fluorescence data and processing with individual calibration curves, the amount of Dox accumulation (Dox cellular uptake,%) was calculated by dividing the amount of Dox (free and encapsulated) in cell lysate to initial amount of free or encapsulated Dox added to cell media [149].

2.2.22. Data Analysis

The data shown represents the mean values of multiple replicates (n=3). Statistical analysis was performed using one-way ANOVA with Tukey's post hoc test in GraphPad Prism software, considering *p < 0.05; **p < 0.005; ***p < 0.0001.

3. Results and Discussion

In this thesis, pH-responsive CD NS was developed in a two-step process for Dox delivery, with FA conjugation incorporated to improve therapeutic effectiveness (Figure 21). To avoid complexity, the results are organized into six sections: synthesis of oxidized β -CD, synthesis and optimization of NS, Dox loading and release, FA conjugation, Dox loading and release by FA-conjugated NSs, and cell-based assays.

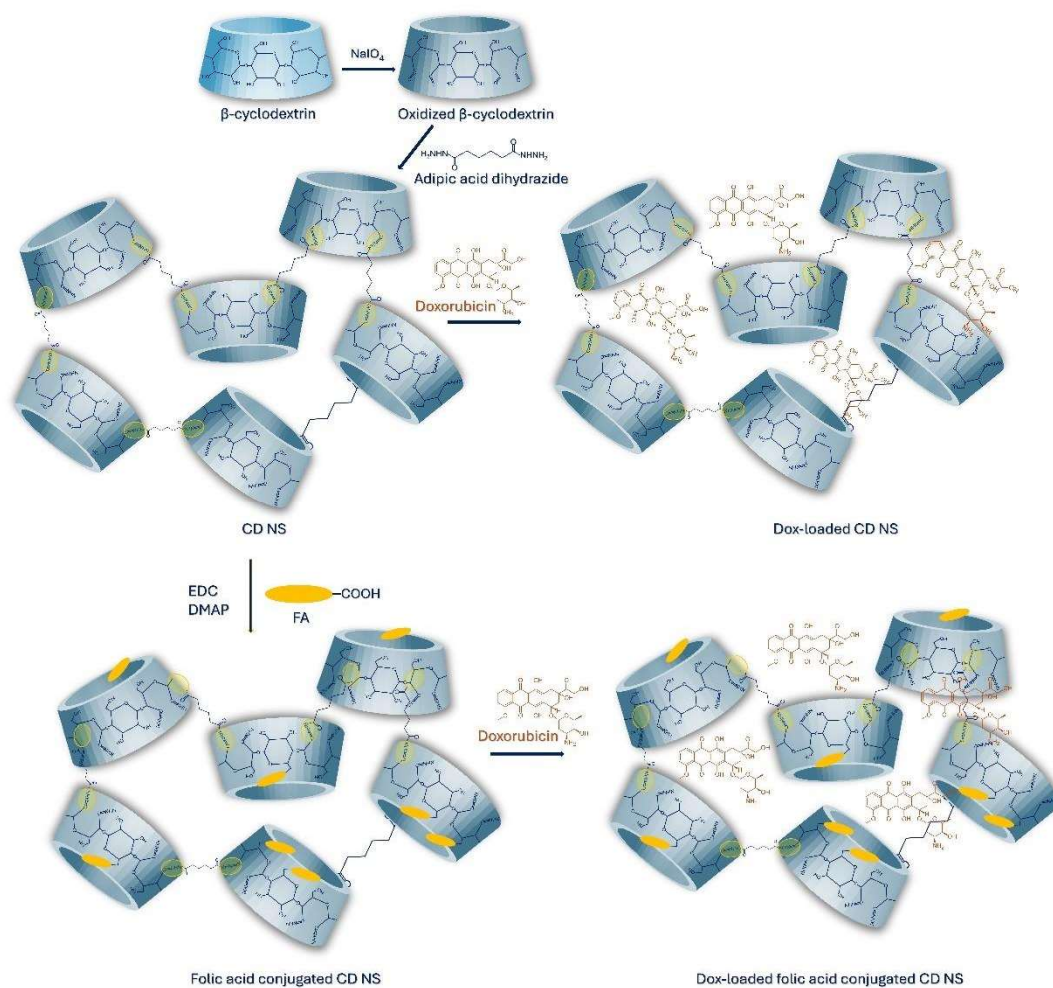


Figure 21. Schematic representation of NS synthesis, FA conjugation and Dox loading.

3.1. Synthesis of Oxidized β -CD

The oxidation reaction for β -CD was analyzed using various techniques, including FTIR, UV-Vis spectroscopy, potentiometric assays for aldehyde content determination, $^1\text{H-NMR}$, XRD, TGA, DSC and SEM.

3.1.1. FTIR Analysis for β -CD Oxidation

FTIR analysis was carried out on the dried samples to investigate the functional groups of the materials and to assess chemical composition changes resulting from oxidation reaction. Figure 22 shows the FTIR spectra of β -CD and Dia3. Both specimens exhibited characteristic bands at 3400 cm^{-1} , 2930 cm^{-1} , 1640 cm^{-1} , 1155 cm^{-1} and 1030 cm^{-1} . The identity of each band explained in Table 4 [150]. Additionally, the conversion of vicinal diols in β -CD to dialdehydes in Dia3 was confirmed by the recognition of aldehyde-specific bands at 2860 cm^{-1} , 1720 cm^{-1} , and 875 cm^{-1} in the spectra of Dia3 [73,151–153]. The identity of each band for Dia3 was also explained in both Figure 22 and Table 4. These results demonstrate that the oxidation of β -CD was successfully achieved using NaIO_4 .

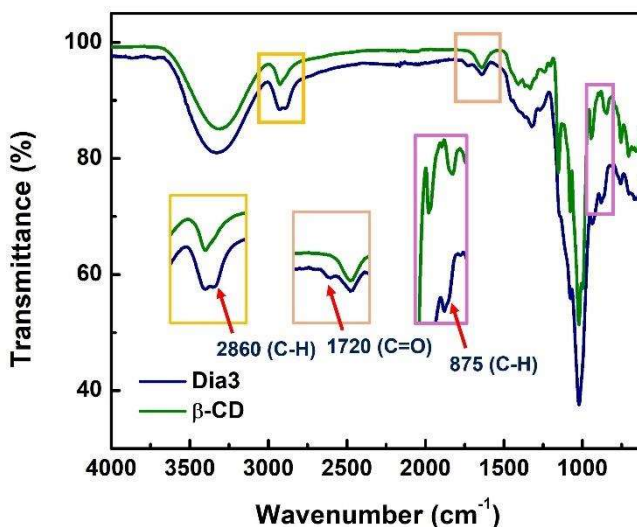


Figure 22. FTIR spectra of β -CD and oxidized β -CD (namely Dia3).

Table 4. Characteristic bands for β -CD and Dia3 with their corresponding identity.

Sample(s)	Wavenumber, cm^{-1}	Identity
β -CD, Dia3	3400	O-H stretching vibration
β -CD, Dia3	2930	C-H stretching vibration
β -CD, Dia3	1640	H-O-H bending vibration

β -CD, Dia3	1155	Asymmetric stretching vibration of C-O-C
β -CD, Dia3	1030	Symmetric stretching vibration of C-O-C
Dia3	1720	C=O stretching (carbonyl, aldehyde)
Dia3	2860	C-H stretching vibration (aldehyde)
Dia3	875	C-H bending vibration (Hemiacetal or hydrated)

3.1.2. UV-Vis Analysis for β -CD Oxidation

UV-Vis analysis was performed on β -CD and Dia3 samples to reveal structural differences induced by the presence of aldehydes, which can be detected through UV-Vis absorption spectroscopy [154]. The UV-Vis spectra of β -CD and Dia3 are shown in Figure 23. As observed in the spectra, β -CD exhibited no absorption peaks within the examined wavelength range [155]. Conversely, Dia3 displayed a distinct absorption peak at 240 nm, which corresponds to the π - π^* transition of the C=O groups in its aldehydes moieties [156]. This result confirmed the presence of aldehydes in Dia3 as opposed to β -CD, thereby verifying the successful oxidation of β -CD.

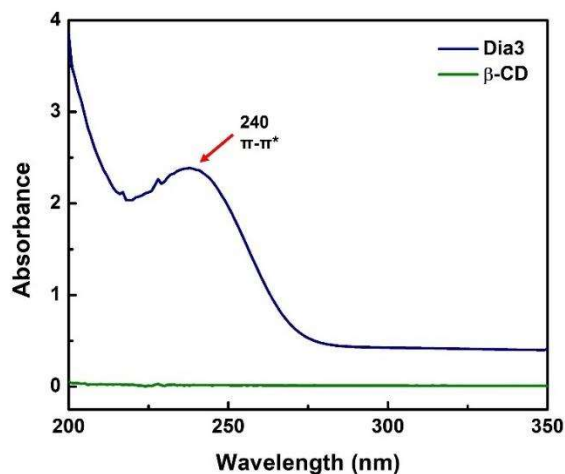


Figure 23. UV-Vis spectrum of β -CD and Dia3.

3.1.3. Aldehyde Content Determination

The aldehyde concentration in Dia3 was determined using a potentiometric titration technique to validate the oxidation reaction by quantifying the aldehyde content. This approach involves the reaction of aldehyde groups with hydroxylamine hydrochloride, which generates HCl, subsequently titrated with a standard NaOH solution. Figure 24 displays the results of this potentiometric measurement. As shown in Figure 24.a, the pH values of both β -CD and Dia3 solutions in hydroxylamine hydrochloride gradually increased with the addition of NaOH. Notably, the initial pH of the Dia3 solution (1.85) was significantly lower than that of the β -CD solution (3.38), indicating a greater amount of HCl production in the Dia3 solution and, consequently, a lower pH. The pH values of the β -CD solution and the blank hydroxylamine hydrochloride solution were identical (data not shown), confirming the existence of aldehyde groups in Dia3 and the successful oxidation of β -CD [72]. Titration was continued until the pH reached 5.0, after which the differential titration curve for Dia3 was generated (Figure 24.b). The peak's maximum corresponds to the NaOH volume used [157]. The aldehyde content of Dia3 was calculated as 3.75 ± 0.125 mmol/g, as per Equation 3. Although the theoretical aldehyde concentration of Dia3 is 5.29 mmol/g, the measured value of 3.75 mmol/g suggested a partial loss of NaIO_4 's oxidative capacity during the reaction, as well as a tendency for aldehydes to form hemiacetals in aqueous environments. The observed lower aldehyde concentration, consistent with previous studies [72], confirms the effective oxidation of β -CD using NaIO_4 .

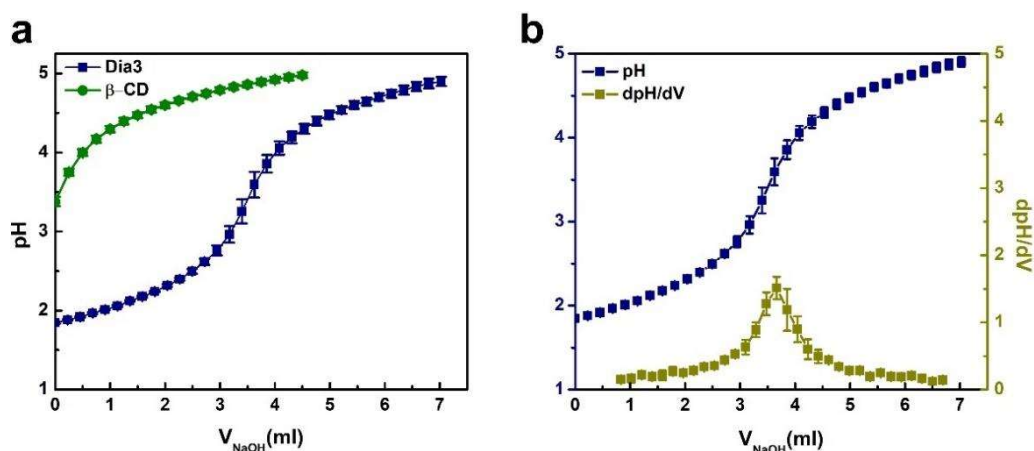


Figure 24. a) The alteration in the pH of Dia3 and β -CD (as a control) that dissolves in hydroxylamine hydrochloride mixture. b) Titration and differential curves for Dia3 formulated in hydroxylamine hydrochloride solution.

3.1.4. Proton NMR Analysis

In order to determine and validate the chemical compositions of β -CD and Dia3, $^1\text{H-NMR}$ analysis was conducted. For this analysis, Dia3 was dissolved in $\text{DMSO-}d_6$, while β -CD was dissolved in D_2O . Dia3 was specifically not dissolved in D_2O because its aldehyde groups react rapidly with hydroxyl groups in water, leading to the formation of hemiacetals and, consequently, the near disappearance of aldehyde peaks. Hence, Dia3 was dissolved in $\text{DMSO-}d_6$, and spectra were subsequently recorded. Figure 25 represents $^1\text{H-NMR}$ spectra of both β -CD and Dia3. The β -CD signals were observed at 4.86 ppm (H1), 3.37 ppm (H2), 3.76 ppm (H3), 3.46 ppm (H4), 3.67 ppm (H5), 3.78 ppm (H6a,b), and 4.61 ppm (D_2O). The OH signals of β -CD were not detected due to the interaction with the solvent. In contrast, the spectrum of Dia3 clearly displayed chemical shifts corresponding to the hydrogens, in addition to those of OH groups. For Dia3, the signals were recorded at 5.67 ppm (OH2), 5.71 ppm (OH3), 4.42 ppm (OH6), and 2.45 ppm ($\text{DMSO-}d_6$). The aldehyde proton signal in Dia3 was observed around 9.55 ppm, which was absent in β -CD. The proton peak of aldehydes was diminished due to the formation of hemiacetal. New peaks at 6.45 ppm and 6.88 ppm corresponded to the protons of CH and OH in the hemiacetals, as aldehydes were unstable in nucleophilic

solutions. These results were consistent with previous analysis and confirm the successful oxidation of β -CD using NaOI_4 [72,158,159].

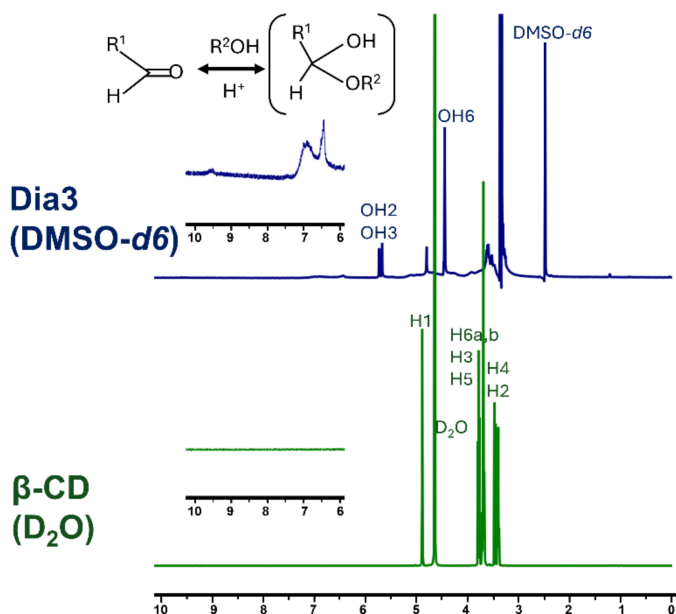


Figure 25. $^1\text{H-NMR}$ spectra of β -CD and Dia3. The spectrums of β -CD and Dia3 were recorded in D_2O and $\text{DMSO-}d_6$, respectively.

3.1.5. XRD Analysis for β -CD Oxidation

XRD analysis was utilized to examine the crystal structure of the materials, providing valuable insights into the structural changes induced by chemical processes. Studies on the structure of β -CD hydrates have shown that CDs exhibit a crystalline structure [160]. They form hydrates with water, leading to a denser structure, reduced crystallinity, and distortion of the cyclodextrin macrocycles as water molecules occupy the cavity of the cyclodextrin molecule [161]. Therefore, changes in the crystalline structure or crystallinity can provide insights into the oxidation reaction of β -CD. Figure 26 displays the XRD spectra of β -CD and Dia3. As reported in the literature, β -CD exhibited distinct crystalline peaks at 2θ values of 9.5° , 10.8° , 12.8° , 13.4° , 18.2° , 22.8° , and 27.1° , confirming its crystalline nature [72]. Upon oxidation, these peaks were significantly reduced, indicating the successful oxidation of β -CD and its transition to more amorphous

structure. The oxidation process disrupted the ordered crystalline structure of β -CD, facilitating its transformation into an amorphous state. Furthermore, modest quantities of NaIO_4 contributed to reduced crystallinity, possibly due to the deterioration of the crystalline regions, resulting in the formation of semicrystalline compounds [162]. These findings also confirmed the successful oxidation of β -CD using NaIO_4 .

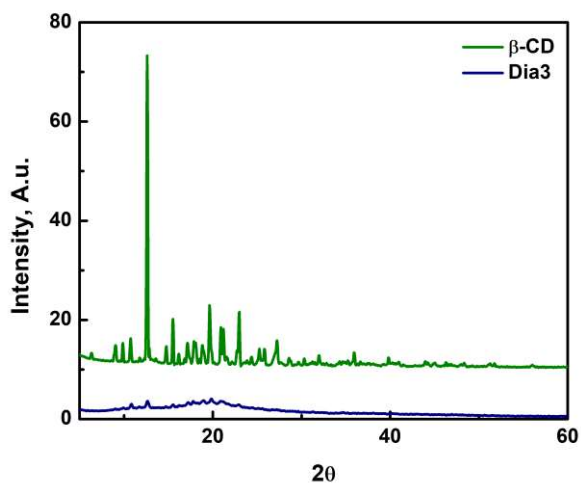


Figure 26. XRD spectra of β -CD and Dia3.

3.1.6. Thermal Analysis by TGA and DSC

TGA was performed on the samples in order to assess their thermal durability, decomposition behaviour, and provide insights into their composition [129,163]. Figure 27.a shows the TGA results for β -CD and Dia3. β -CD exhibited an initial weight loss at approximately 80 °C, corresponding to water evaporation. The initial degradation of β -CD occurred between 300-350 °C, followed by char degradation up to 500 °C, resulting in a total weight loss of 96.16% [164]. Dia3, on the other hand, lost water around 75 °C and started decomposing around 220 °C, which may be associated with the chain disruption caused by oxidation, leading to reduced thermal stability and a total weight loss of 98.13% [131].

The thermal behaviour of the materials was further examined using the DSC technique to ascertain their physical changes during heating. DSC provides insights into the structure

of the materials [165]. Figure 27.b shows the DSC diagrams of the samples. For β -CD, two endothermic peaks at 117 °C and 322 °C represented water loss and melting, respectively, while an exothermic peak at 219 °C corresponded to crystallization [166]. In the case of Dia3, water loss occurred at 100 °C, and crystallization was observed at 158 °C. Following oxidation, the initial endothermic peak shifted to 100 °C, while the crystallization peak decreased to 158 °C. These changes suggested that oxidation deteriorates a portion of the isoform unit, reflecting a modification in the original crystalline structure, as also confirmed by the XRD results [162]. Since the predefined orientation within a structure requires energy, it is expected that the crystallization temperature of an amorphous material was less than that of a crystalline or semicrystalline material.

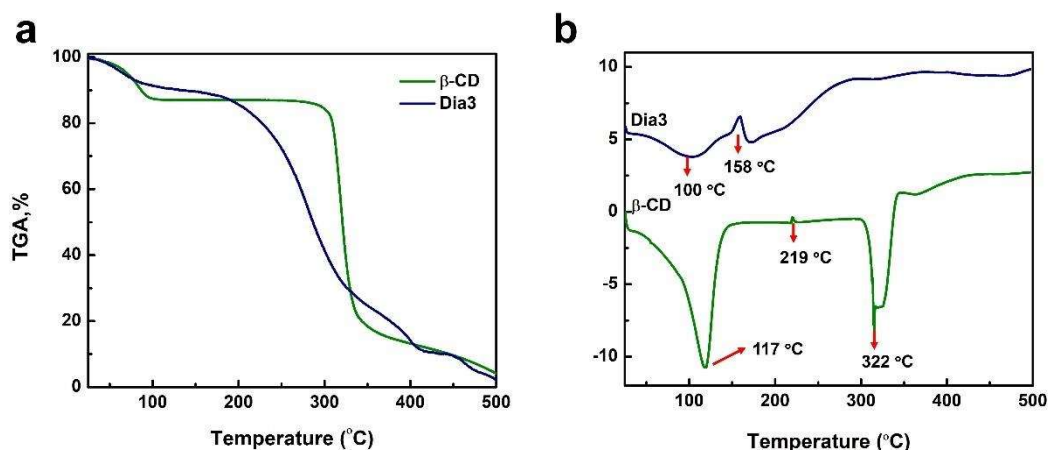


Figure 27. a) TGA analysis and b) DSC diagrams for β -CD and Dia3.

3.1.7. SEM Analysis for β -CD Oxidation

SEM analysis was performed to investigate the morphology of the materials, providing additional insights into their homogeneity. The SEM analysis was conducted on freeze-dried materials, as shown in Figure 28. The SEM images revealed distinct morphological differences between β -CD and Dia3, although both exhibit irregular patterns. β -CD possesses a disordered structure [158,167]. Following oxidation with NaIO_4 , Dia3 showed morphological changes, as observed in the SEM analysis [162]. These findings were consistent with previous characterizations, including XRD and thermal studies.

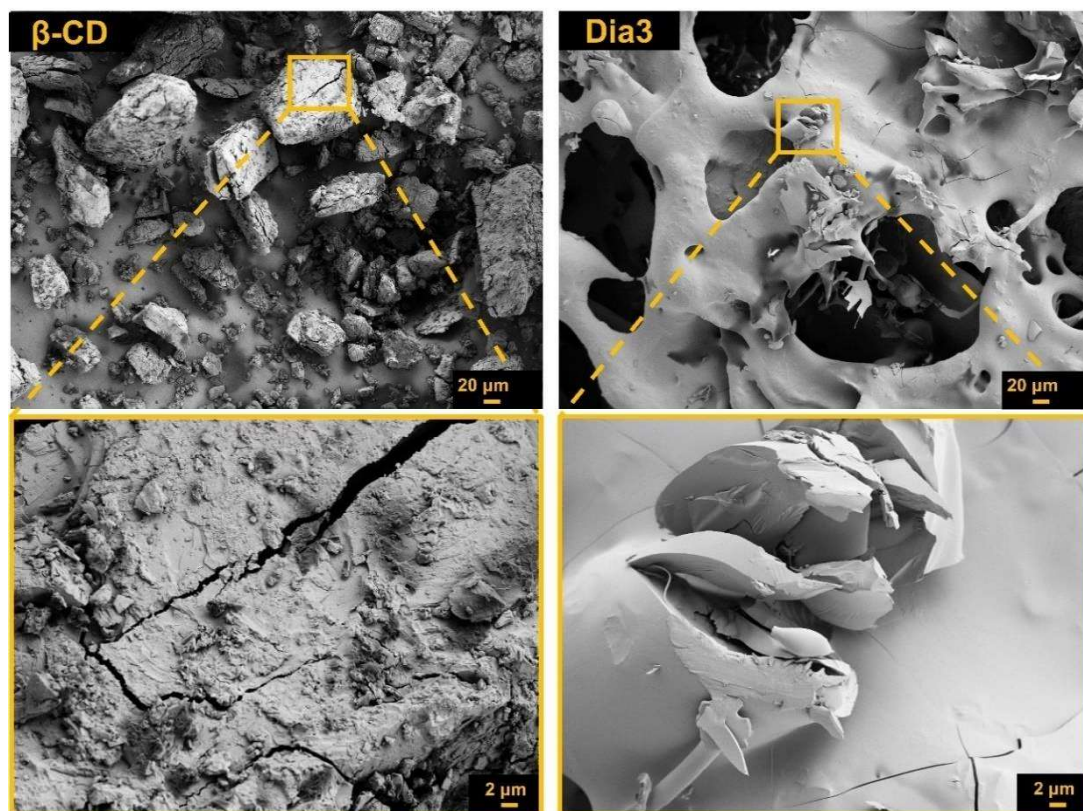


Figure 28. SEM micrographs for β -CD and Dia3.

3.2. Nanosponge Synthesis

NSs were synthesized through the reaction between Dia3 and ADH. At first, NSs with different crosslinker ratios were generated. These NSs were characterized by FTIR, DLS/Zeta analysis, TGA and Dox loading. The optimized NS was further characterized by UV-Vis, XRD, DSC, SEM, TEM, pH-responsiveness and long-term stability assessments.

3.2.1. Optimization of NS

In this section, DLS and Zeta potential measurements at different time intervals for NS3:1 synthesis will be explained (Table 5, Figure 27). Then, FTIR, DLS, Zeta potential, TGA

and encapsulation efficiency analyses for NSs having different crosslinker ratios will be evaluated.

NS3:1 synthesis was conducted in water by the reaction between aldehydes of Dia3 and hydrazides of ADH. After mixing Dia3 and ADH solutions, DLS and Zeta measurements were carried out to optimize NS formation. Table 5 illustrates Z-average (nm), PDI and Zeta potential of reaction mixture of NS3:1 in order to optimize the time for obtaining NS3:1 and end the reaction. As can be seen, Z-average (nm) and PDI values indicated that NS formation was time-dependent. Before 24 h, the reactants require time to solubilize which is also supported by Figure 29.a and Figure 29.b showing two distinct peaks of size inside the reaction mixture. Therefore, it was concluded that the reaction for NS formation continued for 48 h and ended at this time point.

Table 5. Z-average (nm), PDI and Zeta potentials (mV) of NS3:1 in different time intervals which are recorded for the process optimization.

Time, h	Z-average, nm	PDI	Zeta potential, mV
0	96.78 ± 47.46	0.8017 ± 0.48	-1.586 ± 1.89
2	60.20 ± 66.80	0.6344 ± 0.40	-1.354 ± 0.88
4	169.60 ± 15	0.2687 ± 0.08	-5.906 ± 8.06
6	9.82 ± 0.02	0.6322 ± 0.01	-0.957 ± 0.97
8	8.62 ± 0.14	0.4249 ± 0.01	-1.857 ± 2.04
10	9.13 ± 0.06	0.4524 ± 0.01	-
24	15.05 ± 0.14	0.3304 ± 0.01	-
30	18.58 ± 1.04	0.3009 ± 0.03	-
45	60.49 ± 0.75	0.1866 ± 0.01	-
48	97.86 ± 1.28	0.1715 ± 0.02	-0.008 ± 0.03

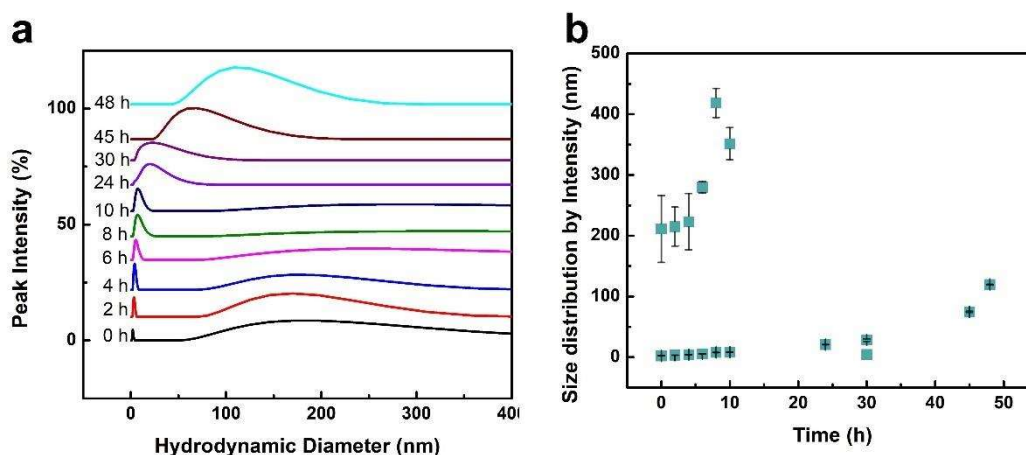


Figure 29. Time-dependent size distribution by intensity of NS3:1. a) peak intensity distribution by the time and b) peak values for each time interval.

FTIR Analysis for NS with Different Crosslinker Ratio

FTIR analysis was performed on the dry samples to investigate functional groups of the specimens, and to evaluate the differences between chemical structures to prove crosslinking reaction shown in Figure 30. Figure 30.a indicates the spectra of Dia3 and NS3:1. Dia3 had characteristic bands for aldehyde at 2860 cm^{-1} , 1720 cm^{-1} and 875 cm^{-1} for C-H, C=O and C-H stretching of aldehydes, respectively [73,151–153]. Upon crosslinking, two peaks of aldehydes disappeared, while the peak at 2860 cm^{-1} was weakened. The differences in the spectrum between Dia3 and NS3:1 was also indicated by the formation of hydrazone bonds. The bands at 1647 cm^{-1} and 1550 cm^{-1} in the spectrum of NS3:1 refer to the C=N stretching and N-H bending of amide bond, respectively [130,131,168–170], showing the successful crosslinking of Dia3 with ADH to form NS3:1. Figure 30.b shows schematic representation of hydrazone bond in NS3:1, indicated by yellow circles. Figure 30.c shows the spectra of Dia3, ADH, Dia3-ADH physical mixture and NS3:1. Accordingly, the spectra of each specimen differed from each other. Specifically, NS3:1 and Dia3-ADH physical mixture were completely different from each other, indicating the chemical reaction between Dia and ADH. Figure 30.d shows the spectra of NS3:05, NS3:1 and NS3:2, which have different crosslinker ratio. Accordingly, each NS had characteristics bands for hydrazone bond at 1647 cm^{-1} and 1550 cm^{-1} , indicating the crosslinking reaction in NSs with different ADH content.

These findings suggest successful crosslinking reaction between Dia3 and ADH, forming NS.

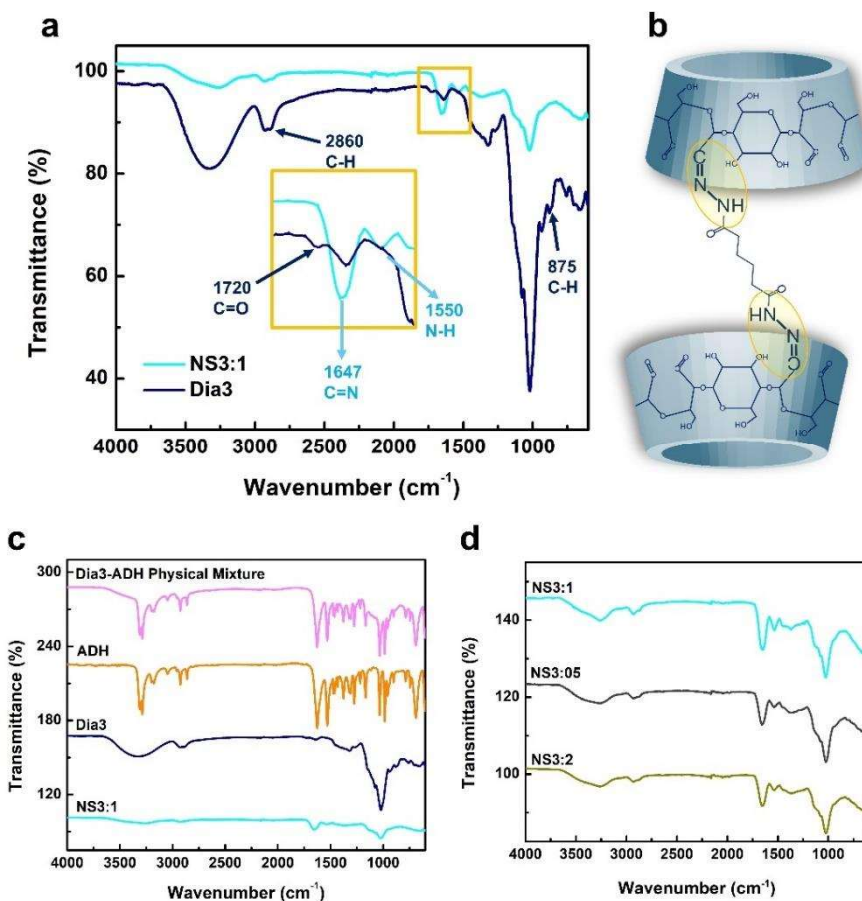


Figure 30. a) FTIR spectrum of Dia3 and NS3:1, b) schematic representation of NS3:1 (hydrazone bonds labelled with yellow circles), FTIR spectrum of c) Dia3, ADH, Dia3-ADH physical mixture and NS3:1, and d) NS3:05, NS3:1 and NS3:2.

Table 6. Characteristic bands for β -CD and Dia3 with their corresponding identity.

Sample(s)	Wavenumber, cm^{-1}	Identity
Dia3	3400	O-H stretching vibration
Dia3, NS3:05, NS3:1, NS3:2	2930	C-H stretching vibration
Dia3	1640	H-O-H bending vibration

Dia3, NS3:05, NS3:1, NS3:2	1030	Symmetric stretching vibration of C-O-C
Dia3	1720	C=O stretching (carbonyl, aldehyde)
Dia3	2860	C-H stretching vibration (aldehyde)
Dia3	875	C-H bending vibration (Hemiacetal or hydrated)
NS3:05, NS3:1, NS3:2	1647	C=N stretching vibration (amide bond)
ADH, NS3:05, NS3:1, NS3:2	1550	N-H bending vibration (amide bond)

DLS/Zeta Analysis for NSs with Different Crosslinker Ratio

DLS and Zeta measurements were carried out in water to elaborate the hydrodynamic size, Zeta potential, and PDI for the NSs with different crosslinker ratios, as shown in Table 7. According to Table 7, the Z-average (nm) values of NSs are near 100 nm, and each of them is significantly different. The Z-average (nm) value of NS3:05 is 81.81 nm and doubling the crosslinker ratio to produce NS3:1 increased the Z-average value to 123.8 nm. This increase in size with a higher crosslinker ratio suggests that the NS particles grow as more crosslinker is added [171]. However, the size of the NS reduced when the amount of crosslinker was further increased. When the amount of crosslinker was high, electrostatic interactions between ADH and Dia3 forms, limiting the expansion of NS thus forming more stiff and densely crosslinked network [172]. PDI value is crucial for determining the size distribution of NSs. Only NS3:1 has a PDI lower than 0.3, showing an acceptable size distribution, while NS3:05 and NS3:2 have a PDI higher than 0.3, which are not preferred for drug delivery purposes [173]. Wide and narrow size distributions of NSs are also shown in Figure 31. Accordingly, NS3:1 exhibits a narrower size distribution by intensity compared to NS3:05 and NS3:2. The zeta potential of all NSs was near zero mV, due to the formation of hemiacetals and acetals from free aldehydes and neighboring hydroxyls in aqueous media, which might be reducing the electronegativity of NSs, thus showing almost zero surface charge in all species [174].

Table 7. Z-average, PDI and Zeta Potential values for the NS with different crosslinker ratio.

NS	Z-Average, nm	PDI	Zeta Potential, mV
NS3:05	81.8 ± 0.73	0.4507 ± 0.01	-0.7754 ± 1.04
NS3:1	123.8 ± 1.26	0.2462 ± 0.01	-0.0377 ± 0.02
NS3:2	112.4 ± 3.44	0.3907 ± 0.01	0.0345 ± 0.01

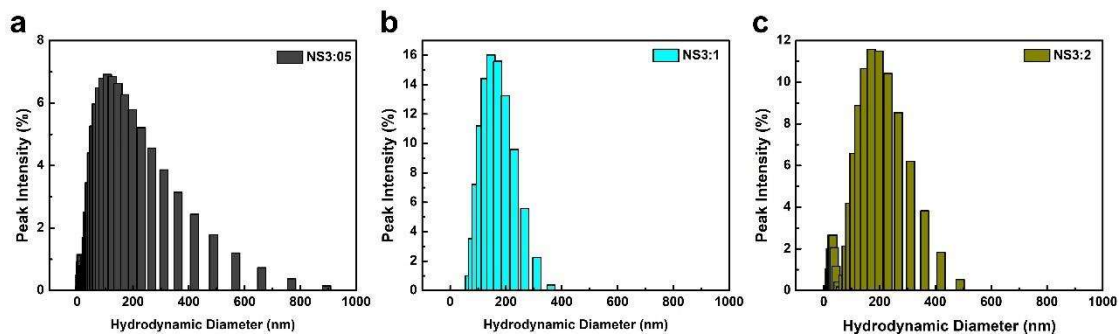


Figure 31. Size distribution by intensity of a) NS3:05, b) NS3:1 and c) NS3:2.

TGA Analysis for NSs with Different Crosslinker Ratio

TGA analysis was performed on the samples in order to evaluate the thermal stability and decomposition mechanisms and give insight into the composition of the specimens [129,163]. Figure 32.a shows TGA curves of the Dia3, Dia3-ADH PHY and NS3:1 which recorded in the range of 25 °C and 500 °C. Dia3 had water loss around 75 °C and started to degrade around 220 °C which could be linked with the chain unconformity of β -CD upon oxidation, yielding thermal instability showing total weight loss of 98.13% [131]. NS3:1 showed water loss around 75 °C and started to decompose at 215 °C showing a total of 63.95 % weight loss at 500 °C. The crosslinking of Dia3 to form NS3:1 enhanced thermal stability, by reducing the weight loss at 500 °C while both Dia3 and NS were starting to decompose at nearly same temperatures. Normally, crosslinking of oxidized specimen with ADH increases the maximum temperature value of degradation [131]. But in our case, we observed the first decomposition at nearly same temperature, and a second decomposition of Dia3 was visible while no other decomposition was recorded in defined temperature range. Therefore, we can assume that, crosslinking of Dia3 with ADH enhanced the maximum temperature for second degradation, indicating the crosslinking

reaction [131]. Accordingly, the diagram for Dia3-ADH PHY (physical mixture) was different than that of NS3:1, indicating the crosslinking reaction and enhancement of thermal stability with ADH covalent bonding. Figure 32.b illustrates TGA diagrams for NSs with different crosslinker ratio. Accordingly, all NSs experienced water loss and starting point for decomposition as 75 °C and 215 °C, respectively. The total weight loss for the samples were recorded as 59.86% for NS3:05, 63.95 % for NS3:1 and 28.96 % for NS3:2. The diagram for NS3:05 is not different than the NS3:1. This might be related to the crosslinking amount. While NS3:1 had the same molar ratio of aldehyde to ADH, while NS3:05 had half amount of ADH compared to NS3:1, thus having free aldehydes. However, since aldehydes react with free hydroxyls, this might act as second crosslinking mechanism, thus enhancing its molecular weight [175]. Once the amount of ADH increased 2-fold in NS3:2 compared to NS3:1, the weight loss was significantly lowered from 63.95% to 28.96%. This was related to the crosslinker amount that was used, which enhanced the thermal stability of the NS.

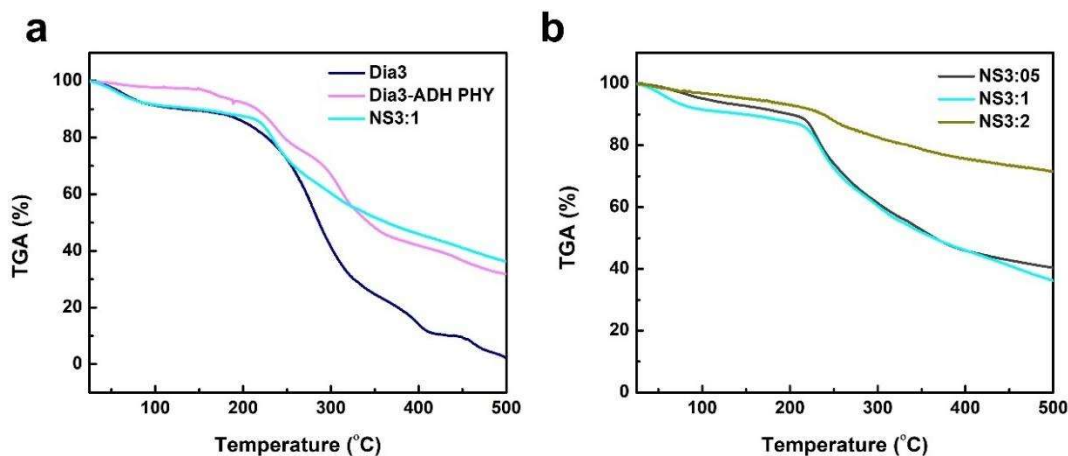


Figure 32. TGA analysis of a) Dia3, Dia3-ADH physical mixture (PHY) and NS3:1, b) NSs with different crosslinker ratios.

Dox Loading to NSs with Different Crosslinker Ratio

Dox was loaded to the NSs with different ADH content in order to evaluate the effect of crosslinker amount on drug loading efficiency. For the loading experiment, 5 mg NS and 2 mg Dox were mixed. The free Dox was determined by fluorescence spectrophotometer, and EE% and LC for each formulation were calculated by Equations 1 and 2 and mean

values are shown in Table 8. The EE% of NSs are 89.94% for NS3:1, 86.74% for NS3:05, and 87.44% for NS3:2. The slight variations in drug loading efficiencies can be attributed to the hydrodynamic sizes measured by DLS, with the largest size obtained in NS3:1 (123.8 nm), which corresponded to a higher drug loading [176].

Table 8. The amount of NS, Dox, reaction volume and encapsulation efficiency (EE%) for NS3:05, NS3:1 and NS3:2.

NS	NS amount, mg	Dox amount, mg	Reaction volume, ml	EE, %	LC
NS3:1	5	2	3	89.94	0.36
NS3:05	5	2	3	86.76	0.34
NS3:2	5	2	3	87.44	0.35

Based on the findings from the DLS analysis, which revealed the size, PDI, and Dox loading, NS3:1 was chosen for further evaluation. These two criteria are particularly crucial in the design of drug delivery systems [171].

3.2.2. UV-Vis Analysis for NS Synthesis

UV-Vis absorbance spectroscopy was conducted on Dia3 and NS3:1 in order to evaluate their structural differences as shown in Figure 33. Dia3 had an absorption band for aldehydes at 240 nm, corresponding to the π - π^* transition of the C=O groups in the aldehydes of Dia3 [156]. However, NS3:1 had no adsorption peak for aldehydes, revealing that no aldehydes were found in NS3:1 because of successful reaction between aldehydes and ADH to form NS3:1.

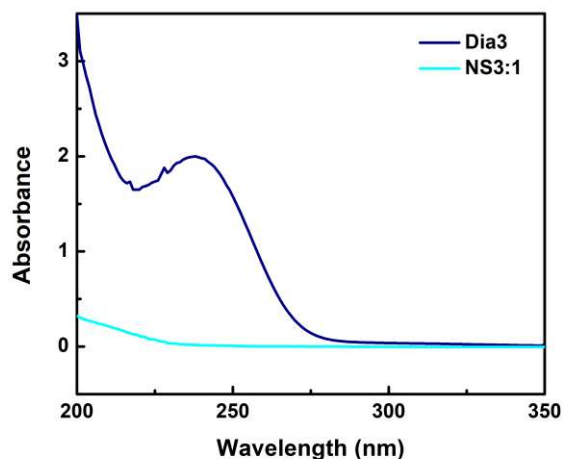


Figure 33. UV-Vis spectra for Dia3 and NS3:1.

3.2.3. XRD Analysis for NS Synthesis

XRD technique is used to evaluate the crystalline structure of the specimens. This technique provides deep insight into the structural arrangements of the materials, embodying the change crystalline structure upon chemical reactions [88]. Figure 34 shows XRD spectra for Dia3 and NS3:1. Dia3 had semicrystalline structure, having peaks at $2\theta=10.8^\circ$, 12.8° , 18.2° which were derived from β -CD backbone [72]. However, the structure of NS3:1 had a complete amorphous structure having no sharp peaks. It was concluded that, Dia3 was crosslinked with ADH, forming CD polymer that was not soluble, and no solid crystalline phases occurred in the spectra of NS3:1 [88]. It was also indicated that Dia3 molecules were evenly distributed through the NS3:1 matrix, showing no phase-separated crystal aggregates [129]. This observation was also recorded with other CD-based NSs [129,177].

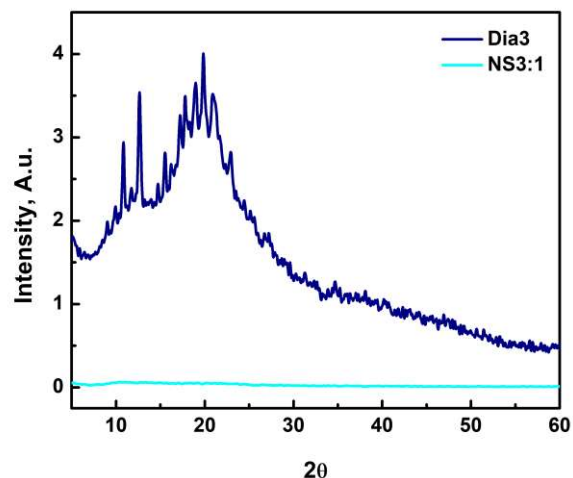


Figure 34. XRD spectra of Dia3 and NS3:1.

3.2.4. DSC Analysis for NS Synthesis

Thermal behavior of the specimens was investigated through DSC analysis, to determine their physical change in terms of thermal transitions upon heating. DSC could give information about the composition in terms of phase transitions [165]. Figure 35 shows DSC diagrams of Dia3, Dia3-ADH physical mixture and NS3:1. Dia3 has one endothermic peak at 100 °C for water loss and an exothermic peak at 158 °C for crystallization, respectively. Upon crosslinking of Dia3 forming NS3:1, the endothermic peak was lowered to 96 °C and exothermic peak reached up to 237 °C, indicating the high input of energy to organize the crystal structure of NS3:1 which is more amorphous compared to Dia3 revealed by the XRD. The peaks of NS3:1 refer to water loss and crystallization, respectively [178]. Similar observations were also reported for epichlorohydrin polymerized β -CD [179] and diphenyl carbonate crosslinked β -CD nanosponges [108]. Thus, the DSC diagram for Dia3-ADH physical mixture is quite different than the NS3:1, indicating the chemical reaction between Dia3 and ADH to form NS3:1. These findings support the oxidation β -CD and crosslinking of Dia3 are successfully achieved.

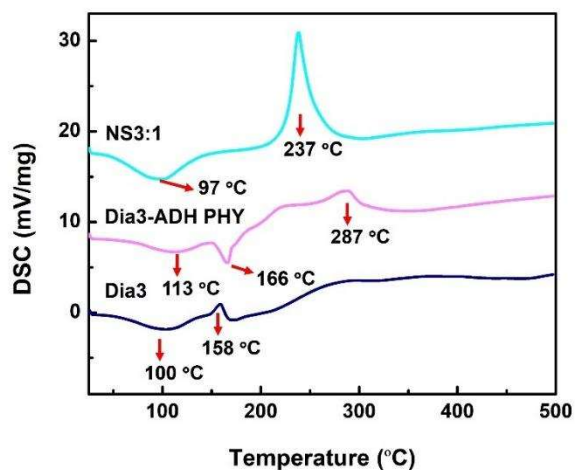


Figure 35. DSC diagrams for Dia3, Dia3-ADH physical mixture (PHY) and NS3:1.

3.2.5. SEM Analysis for NS Synthesis

SEM analysis was performed on the samples to determine their morphology. SEM analysis was completed on freeze-dried samples and showed in Figure 36. According to the SEM micrographs, Dia3 has disordered structure [162]. The crosslinking of Dia3 also reveals the change in morphology whereby the smaller sized clusters were observed in the NS3:1, which have irregular surface [107,171], indicating the NS formation [158,180].

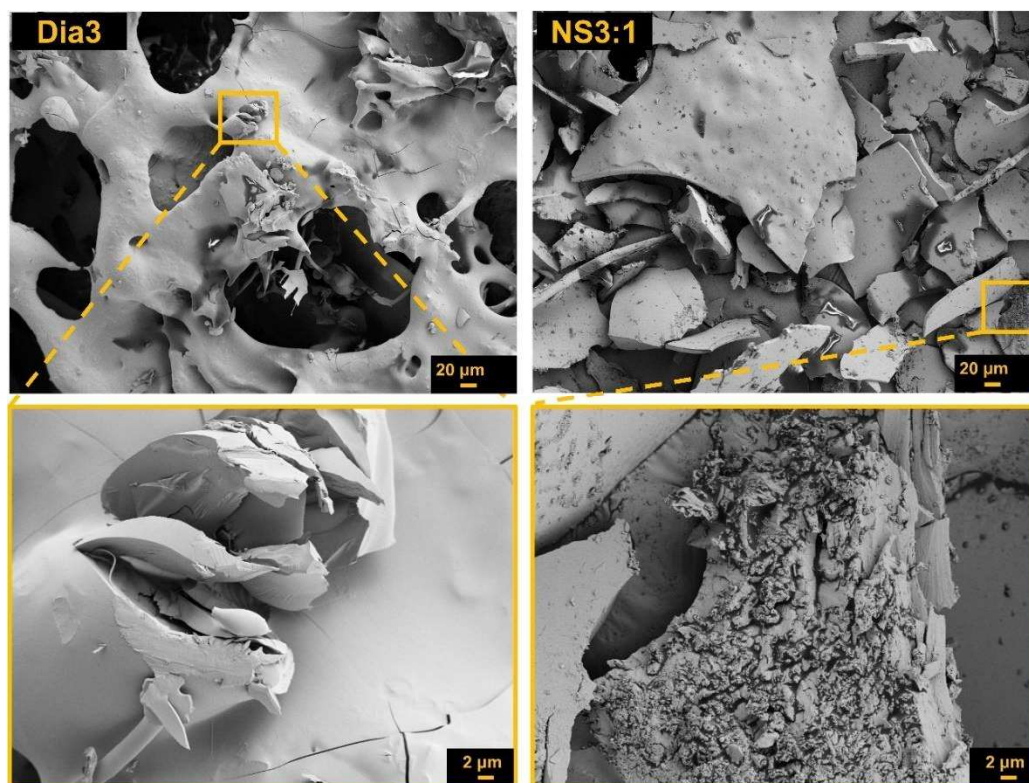


Figure 36. SEM micrographs for Dia3 and NS3:1.

3.2.6. TEM Analysis for NS Synthesis

TEM analysis was conducted on NS3:1 (48 h post-synthesis) to examine its shape and dry size. Figure 37 displays TEM micrographs of NS at varying magnifications. TEM examination indicates that NS displays a consistent spherical morphology and distinct texture with homogeneous size distribution [171]. The dry size of the NS3:1 immediately post-synthesis was approximately 36 nm. Nonetheless, the size determined by DLS is significantly larger (97.86 nm) than that observed in TEM. This is due to DLS measuring the hydrodynamic size of particles while they are suspended in water throughout the assessment. Consequently, the distinction between DLS and TEM elucidates the swelling capacity of this nanostructure, which is also associated with the porous architecture demonstrated by SEM [128]. Comparable findings have been documented for epichlorohydrin crosslinked NS [177] and pyromellitic anhydride crosslinked NS [111].

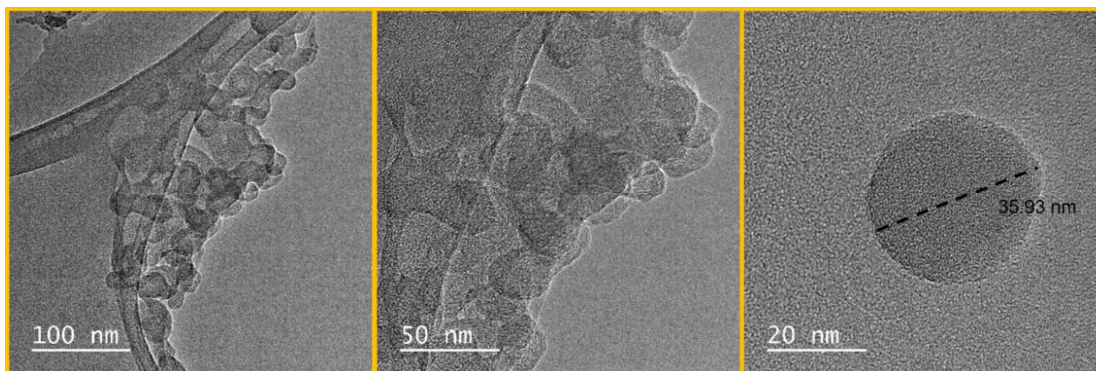


Figure 37. TEM analysis of NS3:1 with different magnifications.

3.2.7. pH-responsiveness of NS3:1

The pH-responsiveness of NS3:1 was evaluated by measuring its hydrodynamic size when dispersed in PBS at pH values of 5.5, 6.5 and 7.4. This method is particularly valuable for determining whether hydrazone bonds within NS3:1 undergo cleavage under acidic conditions [141]. Figure 38 shows the size distribution by intensity of NS3:1 in PBS across varying pH levels, along with Z-average (nm) and PDI values. DLS measurements revealed that the size of NS3:1 gradually decreased from 141.6 nm to 103.5 nm as the pH shifted from 7.4 to 6.5, suggesting hydrazone bond cleavage under acidic conditions [141]. A slight increase in hydrodynamic size (from 103 nm to 110 nm) was observed as the pH changed from 6.5 to 5.5. This increase could be associated with the reaction between free hydroxyls and aldehyde groups in NS3:1, which could involve an acid-catalyzed condensation reaction [175], thereby slightly increasing the size of NS3:1.

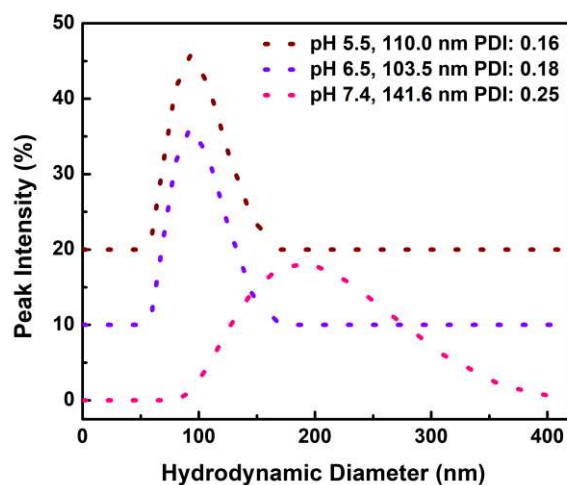


Figure 38. Size distribution by intensity of NS3:1 suspended at pH 5.5, 6.5 and 7.4. Z-average (nm) and PDI values of corresponding specimen are also indicated.

3.2.8. Stability Assessment of NS3:1

A long-term stability assessment of NS3:1 was performed by suspending in water and storing it at 4 °C for 12 weeks. The hydrodynamic size was periodically measured via DLS, with Z-average (nm) values recorded at various time intervals, as depicted in Figure 39. The size of NS3:1 increased from 123 nm to 213 nm in 8-weeks and reached a plateau in 12 weeks. This may be attributed to the instability of aldehydes in aqueous environment, thus, leading to an increase in its size [175]. CDs are recognized for their ability to self-assemble in aqueous media, forming aggregates that range from 20 nm to several micrometers. Moreover, the nearly neutral zeta potential of NS3:1 (-0.0377 + 0.02) likely accounts for its tendency to undergo self-assembly and aggregation during extended storage without agitation [181]. Consequently, the synthesized NS was stored in a freeze-dried state to preserve stability, as its size is not maintained in aqueous environments.

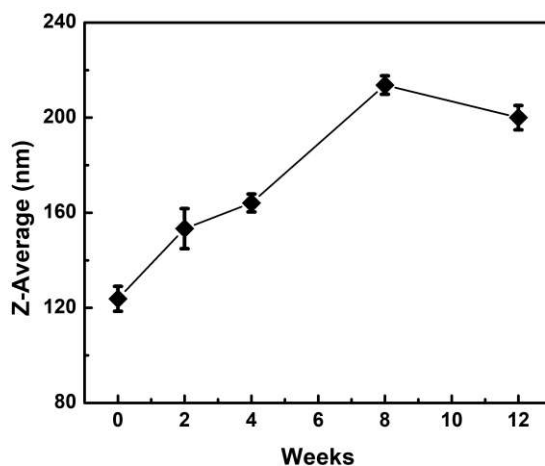


Figure 39. Z-average (nm) values of NS3:1 suspended in water and stored for 12 weeks at 4 °C.

3.1. Dox Encapsulation and Release by Optimized NS

Dox encapsulation with optimized NS (i.e., NS3:1) was assessed through EE% and LC, FTIR, DLS/Zeta measurements, DSC and SEM analysis.

3.1.1. Encapsulation Efficiency and Loading Capacity for NS3:1-Dox

Dox encapsulation for NS3:1 was achieved at various ratios, as detailed in Table 9. Due to the solubility limitations, the Dox concentration was reduced from 2 mg to 0.5 mg per 5 mg of NS3:1 to mitigate dimerization and precipitation [135]. Such aggregation compromises Dox's antitumoral efficacy, and if this occurs within delivery systems, it yields suboptimal therapeutic outcomes. Preventing Dox aggregation is therefore essential for enhancing its effectiveness against tumor cells [182]. Furthermore, nanoparticles with high Dox content are prone to aggregation [183], and lower Dox doses have been favored in certain cases [184]. As can be seen from Table 9 reducing the Dox concentration impacted EE% and LC (mg/mg). The highest drug loading was recorded at

the 2 mg level, although EE% decreased proportionally with lower Dox concentrations, with the lowest EE% recorded at a 0.5 mg Dox loading per 5 mg NS.

Table 9. The amount of Dox loading, EE% and LC (mg/mg) for NS3:1 loaded with different amount of Dox.

NS	NS Amount, mg	Dox Amount, mg	Volume, ml	EE%	LC, mg/mg
NS3:1	5	2	3	89.94	0.348
NS3:1	5	1	3	73.10	0.146
NS3:1	5	0.5	3	58.10	0.058

3.1.2. FTIR Analysis for NS3:1-Dox

FTIR analysis was conducted on dry samples to examine the functional groups of the materials and to assess the variations in the chemical structures of the specimens. Figure 40.a shows FTIR spectra of NS3:1, NS3:1-Dox physical mixture, NS3:1-Dox and Dox. The specific bands for Dox were located at 3060 cm^{-1} , 2938 cm^{-1} , 1577 cm^{-1} , 1518 cm^{-1} , 1237 cm^{-1} and 1140 cm^{-1} which the identity of each band are summarized at Table 10 [185]. The spectra of NS3:1-Dox had bands of Dox at 3064 cm^{-1} and 1234 cm^{-1} , corresponding to the N-H stretching vibrations and the skeleton vibration of the rings for Dox. Thus, the intensity of band at 2960 cm^{-1} increased in NS3:1-Dox due to the incorporation of Dox which strengthens C-H stretching vibrations (Figure 40.b) [185,186]. Thus, the spectra of NS3:1-Dox physical mixture was quite different than the NS3:1-Dox. These findings remarked on the encapsulation of Dox via NS3:1.

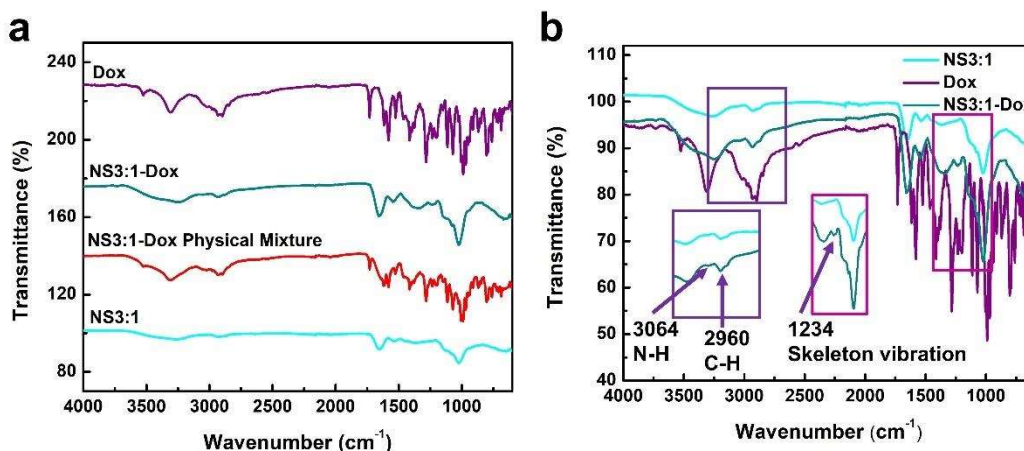


Figure 40. FTIR spectra of a) NS3:1, NS3:1-Dox physical mixture, NS3:1-Dox and Dox, b) NS3:1, Dox and NS3:1-Dox in detail.

Table 10. Characteristic bands for Dox, NS3:1 and NS3:1-Dox with their corresponding identity.

Sample(s)	Wavenumber, cm^{-1}	Identity
Dox, NS3:1-Dox	3064	N-H stretching vibration
Dox	2938	C-H stretching vibration of aromatic ring
Dox	1577	N-H bending vibration
Dox	1518	C-C stretching rings
Dox, NS3:1-Dox	1234	skeleton vibration of the rings
Dox	1140	C-O-CH ₃ of quinine groups
NS3:1, NS3:1-Dox	2960	C-H stretching vibration
NS3:1, NS3:1-Dox	1647	C=N stretching vibration (amide bond)
NS3:1, NS3:1-Dox	1550	N-H bending vibration (amide bond)

3.2.2. DLS/Zeta Analysis for NS3:1-Dox

The size and surface charge of NS3:1 were measured before and after Dox loading using a ZetaSizer, to assess changes in hydrodynamic size and surface charge upon encapsulation. Table 11 illustrated Z-average (nm), PDI and Zeta potentials (mV) of the specimens, while Figure 41 outlines the size distribution by intensity for NS3:1 and NS3:1-Dox formulations. According to Table 11 the hydrodynamic size of NS3:1 in water was 132.9 nm, whereas NS3:1-Dox exhibited a hydrodynamic size of 204.2 nm. This increase suggested a substantial enlargement of NS3:1 upon Dox incorporation. The resulting size was near 200 nm align with the requirements for enhanced permeability and retention (EPR) effect [187]. Moreover, studies suggested that NPs under 500 nm can still undergo endocytosis [188], suggesting that while the size of NS increased upon Dox loading, it remained within the optimal range for pharmaceutical applications. The PDI value for NS3:1-Dox was less than 0.3, indicating a monodisperse and uniform size distribution, which was also supported by the narrow size distribution observed in Figure 41. Table 11 also compares the Zeta potential of NS3:1 before and after the drug loading. The minimal change in surface charge following Dox loading suggested that Dox molecules were internalized within NS3:1, with negligible adsorption on the NS3:1 [189]. This observation aligned with findings from several studies [190–192].

Table 11. Z-average (nm), PDI and Zeta potentials (mV) of NS3:1 and NS3:1-Dox.

Sample	Z-average, nm	PDI	Zeta potential, mV
NS3:1	132.9 ± 0.9308	0.3025 ± 0.0215	-0.0377 ± 0.0211
NS3:1-Dox	204.2 ± 3.898	0.2653 ± 0.0123	0.0249 ± 0.0031

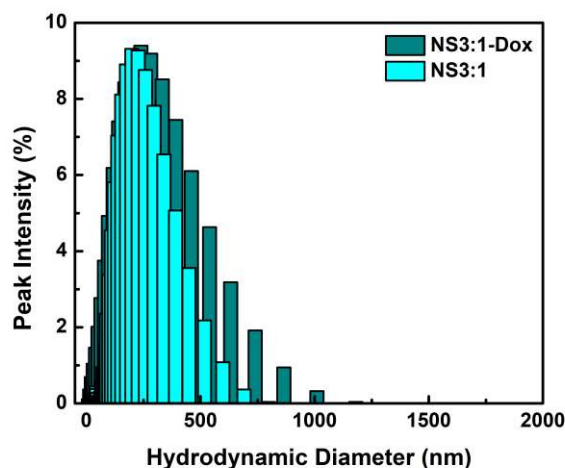


Figure 41. Size distribution by intensity of NS3:1 and NS3:1-Dox.

3.2.3. DSC Analysis for NS3:1-Dox

The thermal characteristics of the materials were examined via a DSC technique to ascertain their physical changes regarding thermal transitions during heating. DSC can provide insights into the chemical makeup and drug loading concerning phase transitions [165]. Figure 42 shows DSC diagrams for the specimens. Accordingly, NS3:1 had one endothermic peak at 96 °C and one exothermic peak at 237 °C, indicating the high input of energy to organize the crystal structure of NS3:1 due to its complete amorphous structure. These peaks of the NS3:1 referred to water loss and crystallization, respectively [178]. Dox possessed two endothermic peaks at 228 °C and 243 °C, indicating the melting points of the Dox upon heating [193]. Upon encapsulation of Dox, the endothermic peak of NS3:1 increased from 96 °C to 114 °C. The intensity of exothermic peak of NS3:1-Dox at 240 °C was reduced compared to NS at 237 °C since it was placed in the same place that endothermic peaks of Dox were. Therefore, the diagram of NS3:1-Dox physical mixture was different than the NS3:1-Dox. These findings supported the encapsulation of Dox by the NS.

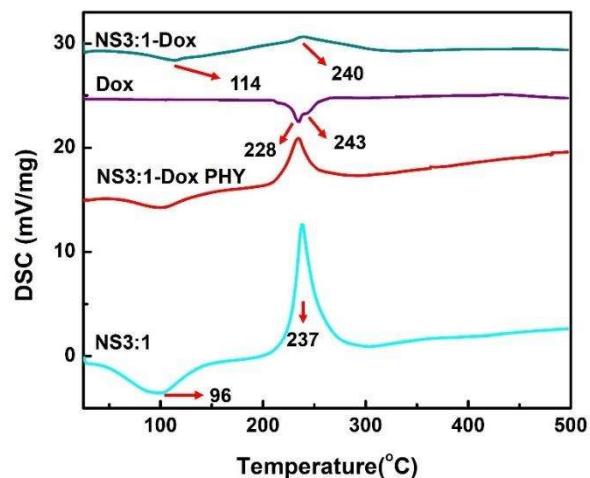


Figure 42. DSC diagrams of NS3:1, NS3:1-Dox physical mixture (PHY) and NS3:1-Dox.

3.2.4. SEM Analysis for NS3:1-Dox

SEM analysis was conducted on the materials to ascertain their morphology. Figure 43 shows SEM images of freeze-dried samples. Dox has irregular morphology and elongated with a smooth surface [194,195]. NS3:1 exhibits smaller sized clusters having irregular surface [107,158,171,180]. NS3:1-Dox PHY comprises both NS3:1 and Dox flakes. NS3:1-Dox exhibited smoother surface compared to NS3:1, indicating the entrapment of Dox through all the NS3:1, pores of NS3:1 were filled up with Dox. Thus, the morphology of NS3:1-Dox PHY was quite different than the NS3:1-Dox, indicating the encapsulation. Similar observations were recorded for resveratrol loaded carbonyl and carboxylate CD NSs [196] and nifedipine loaded carbonate NS [171] and other study for NS [90].

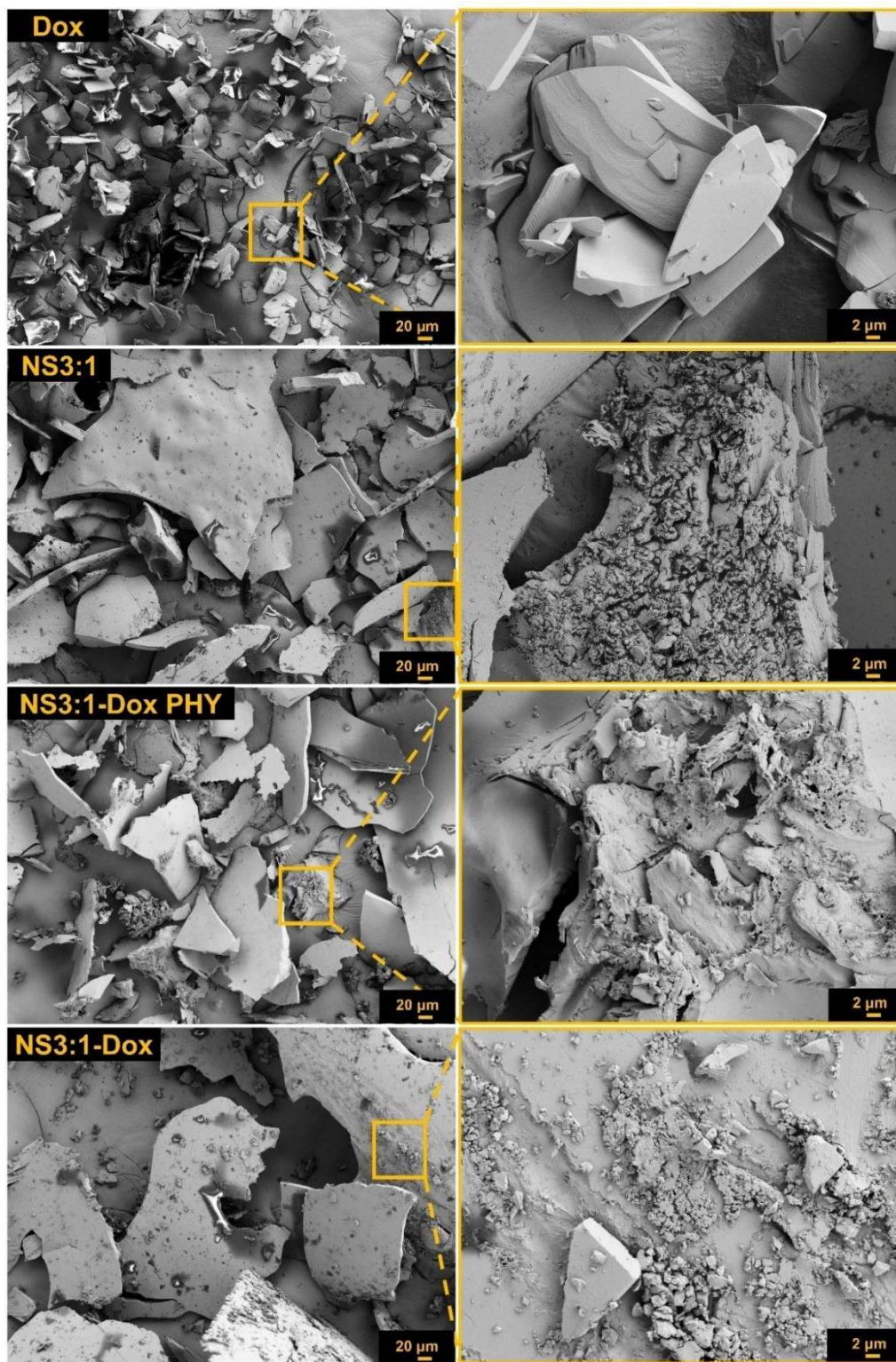


Figure 43. SEM micrographs of NS3:1, Dox, NS3:1-Dox physical mixture (PHY) and NS3:1-Dox samples in freeze-dried state.

3.2.5. *In vitro* Drug Release

Drug release assay was performed with NS3:1-Dox loaded with 0.5 mg and 1 mg Dox. This assay is especially important to investigate the released amount of drug from nano formulations to determine their pharmacokinetics. NP systems travel through blood circulation (neutral pH) and reach the tumor site (pH 6.5) via EPR effect, followed by internalization by tumor cells [197]. Since the pH of cellular organelles like lysosomes is about 5.5, high Dox release in acidic media increases cell cytotoxicity, while low Dox release at neutral pH limits blood circulation [143]. For this purpose, each formulation was assayed for pH 5.5, 6.5 and 7.4 for 72 h and shown in Figure 44. According to Figure 44.a, burst release of Dox from NS3:1-Dox (0.5 mg Dox) in each pH was observed within 8 h and the release was slowed within 12 h, and consistent release was observed until 72 h. Figure 44.b shows Dox release from NS3:1-Dox loaded with 1 mg Dox. Accordingly, Dox release experiences same pattern at pH 7.4 and 6.5, where 35% of total loaded drug were released within 72 h among which 28% was released in the first 12 h. However, once the pH was altered to 5.5, the release was improved. At pH 5.5, Dox release was recorded as 40% within 12 h and 47% within 72 h. According to Figure 44.b, higher amount of Dox loading alteration in the release behaviour of formulation, and here Dox might be released from NS3:1 via either protonation of Dox at acidic pH [143] or breaking of hydrazone bonds in NS3:1 matrix [198]. For the pH 7.4 for both formulations (Figure 44), initial burst release could be attributed to the diffusion of Dox from outer layer of the NS where the Dox was poorly entrapped. The following release could be related to the erosion of NS matrix, eventually leading the release [143]. As can be seen from Figure 44, NS3:1-Dox loaded with 0.5 mg Dox showed higher drug release, compared to the 1 mg Dox. This could be related to the increased Dox loading leads to a slower release rate due to stronger drug-drug interactions and aggregation within the delivery system [199–201]. These findings indicate that NS3:1-Dox (0.5 mg Dox) complex is able to release the encapsulated Dox at neutral and slightly acidic pH values. Drug release was improved once the pH was altered from neutral to 6.5 and 5.5. Especially, pH 5.5 showed greater release as 76% release compared to other pHs. These findings indicate that the Dox release from NS was pH-dependent and shows significantly higher release at acidic pH values (** $p < 0.0001$ by ANOVA), supported by the other pH-responsive carriers [202,203].

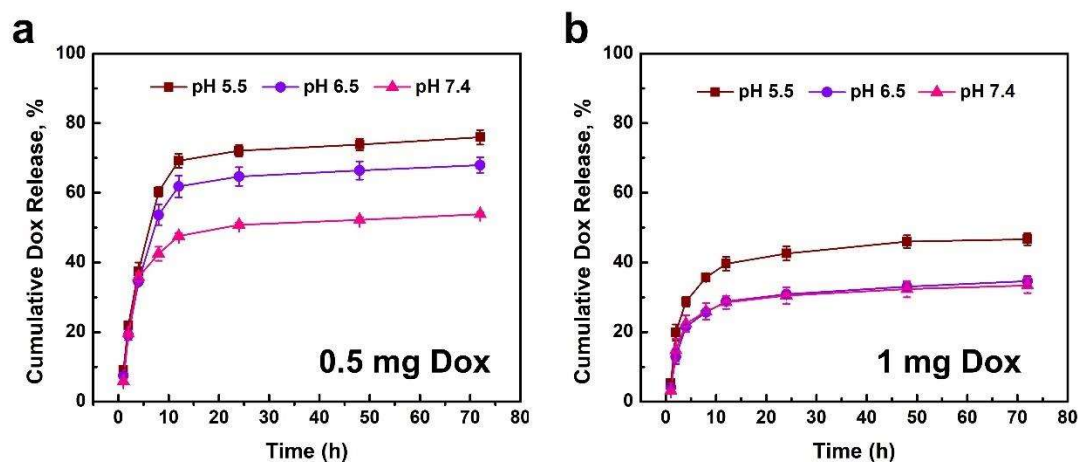


Figure 44. *In vitro* release profile of Dox at different pHs from NS3:1 previously loaded with a) 0.5 mg Dox and b) 1 mg Dox. Dox release was calculated by considering the initial loaded amount of Dox.

3.4. Folic Acid Conjugation to NS3:1

In this section, FA conjugation to NS3:1 will be evaluated by chemical and physical characterizations techniques including FTIR, UV-Vis, DLS/Zeta, TGA, XRD, SEM and TEM analyses.

3.4.1. FTIR Analysis for NS3:1-FA Conjugate

FA conjugation to NS3:1 was evaluated using FTIR analysis and illustrated in Figure 45. FA had some bands at $3101\text{-}2400\text{ cm}^{-1}$, 1694 cm^{-1} , 1635 cm^{-1} and 1603 cm^{-1} which are explained in Table 12 [204,205]. The spectrum of FA had a band of 1680 cm^{-1} , which was attributed to the free -COOH group. Upon esterification, this band shifted to 1660 cm^{-1} in the spectrum of NS3:1-FA, indicating the reaction between free -OH of β -CD and -COOH of FA [206,207]. Thus, the spectrum of NS3:1-FA had a band at 1603 cm^{-1} , which corresponded to the bending vibration of -CONH₂, indicating the free amine groups of the FA in NS3:1-FA [204]. Thus, the intensity of C-H band at 2940 cm^{-1} of NS3:1 further increased with FA conjugation, due to C-H bending of aromatic rings of the FA.

Therefore, according to the FTIR analysis, the esterification reaction between FA and NS3:1 was successfully achieved [208].

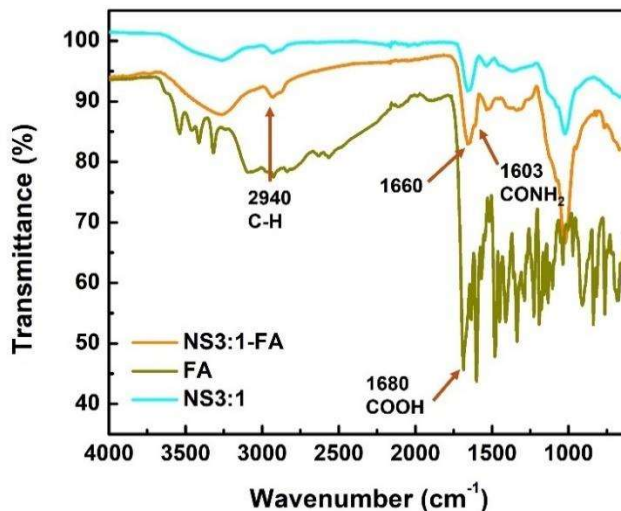


Figure 45. FTIR spectrum for NS3:1, FA and NS3:1-FA conjugate.

Table 12. Characteristic bands for FA, NS3:1 and NS3:1-FA conjugate with their corresponding identity.

Sample(s)	Wavenumber, cm^{-1}	Identity
FA	3101-2400 (broad)	O-H stretching vibration of glutamic acid
FA	3300–3500	N-H stretching vibration of amide groups
FA	1680	C=O stretching vibration of COOH
FA	1635	C=N stretching vibration
FA	1603	bending vibration of NH_2 (CONH_2)
FA, NS3:1-FA	2940	C-H stretching vibration in aromatic ring
NS3:1-FA	1660	N-H bending vibration
NS3:1, NS3:1-FA	1030	Symmetric stretching vibration of C-O-C
NS3:1	1647	C=N stretching vibration (amide bond)
NS3:1, NS3:1-FA	1550	N-H bending vibration (amide bond)

3.4.2. UV-Vis Analysis for NS3:1-FA Conjugate

UV-Vis spectroscopy is employed to examine the chemical characteristics of a substance and is especially important in determining the concentrations of molecules/compounds and conjugation of these molecules to other substances. In this part, UV-Vis analysis was established to investigate FA, since FA has an absorption maxima near 285 nm [209]. The conjugation ratio of FA to NS3:1 was calculated by measuring the free amount of FA in supernatants using calibration curve. Accordingly, conjugation ratio was calculated as 20 % for NS3:1-FA using Equation 4. Figure 46 shows UV-Vis spectra of FA, NS3:1-FA and NS3:1. Accordingly, NS3:1 had no absorption peak within the specified wavelength range. FA exhibited two absorption bands, one at 288 nm, corresponding to for π - π^* interaction in the pterin ring of the FA [139], another at 360 nm, due to the interactions between FA and DMSO [210]. Upon conjugation of FA to NS3:1, the spectrum of NS3:1-FA revealed an absorption maximum at 287 nm [211]. In addition to that, spectra for FA and NS3:1-FA were recorded using equivalent concentrations of samples (25 μ g/ml). As shown in Figure 46, the absorption maximum for free FA was 1.12, while that for NS3:1-FA was 0.213, corresponding to 25 μ g/ml of free FA and 4 μ g/ml bound FA (determined via calibration curve). The conjugation efficiency can also be directly calculated by measuring the concentration of bound FA within a known concentration of conjugate [200]. Applying this method to the system yielded a conjugation ratio of 16% (4 μ g/ml bound FA relative to 25 μ g/ml free FA, as shown in Figure 44). However, calculations derived from Equation 4 (by measuring the unbound FA after the reaction) indicated a 20% conjugation ratio. This discrepancy may be attributed to FA diffusion thorough the NS matrix, which partially masked its absorption, as CDs are capable of forming inclusion complexes with FA [212]. These findings indicated that FA was conjugated on the NS3:1 surface (4% of total FA added) while also being internalized within CD cavities (16 % of total FA added). Altogether, these findings confirmed successful FA conjugation, with a portion of FA incorporated within the NS3:1 matrix.

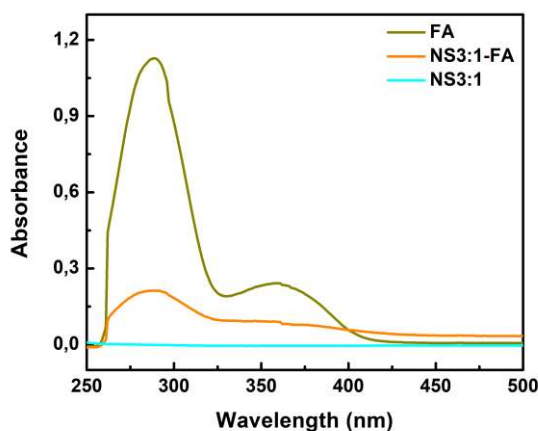


Figure 46. UV-Vis analysis of 25 $\mu\text{g/ml}$ of FA, NS3:1-FA and NS3:1 recorded between 500 nm and 200 nm.

3.4.3. DLS/Zeta Analysis for NS3:1-FA Conjugate

DLS analysis was performed in order to record hydrodynamic size and size distribution of NS3:1-FA conjugate, illustrated in Table 13 and Figure 47. According to the Table 13, Z-average value of NS3:1 was recorded as 132.9 nm, while conjugation of FA increased the hydrodynamic size (219.9 nm for NS3:1-FA), attributed by the addition of FA molecules through the surface of the NS3:1-FA [213]. Table 13 also shows Zeta potentials (mV) of NS3:1, FA and NS3:1-FA. The Zeta potential of FA was negative due to the free carboxylic acid groups of FA [214]. After the conjugation of FA to NS3:1, the Zeta potential changed from -0.0377 mV to -5.821 mV. Normally, once FA was conjugated through its carboxylic acid groups, the remaining free amine groups charges the particles with positive charge [137]. However, in our case, we observed a slightly negative charge. This was due to the remaining free FA inside the NS3:1 as also proved by the UV-Vis analysis, which caused particles to have a negative charge [207]. There were multiple studies showing the decrease of zeta potential after conjugation of FA [215–217]. This negative charge stabilized the NS3:1-FA in aqueous environment by repelling each other, thus showing reduced PDI (0.19) and forming stable colloidal suspension. These findings suggested that FA conjugation was achieved and resulted in larger particles with narrower size distribution and neat negative surface charge.

Table 13. Z-average (nm), PDI and Zeta potentials (mV) of NS3:1, FA and NS3:1-FA conjugate.

Sample	Z-Average (nm)	PDI	Zeta potential, mV
NS3:1	132.9 ± 0.9308	0.3025 ± 0.0215	-0.0377 ± 0.0211
FA	-	-	-39.97 ± 6.303
NS3:1-FA	219.9 ± 7.187	0.1907 ± 0.038	-5.821 ± 0.5272

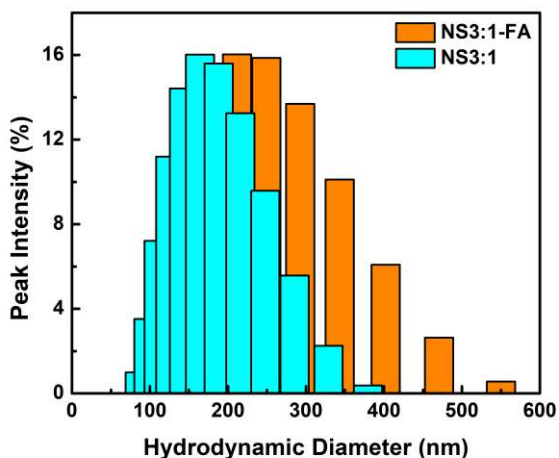


Figure 47. Size distribution by intensity of NS3:1 and NS3:1-FA.

3.4.4. XRD Analysis for NS3:1-FA Conjugate

XRD analysis was employed to investigate the crystal structure of the materials, offering important insights into the structural alterations caused by chemical processes. Figure 48 shows XRD spectrum of NS3:1, FA and NS3:1-FA. FA displayed sharp diffraction peaks indicative of its crystalline structure [218,219]. On the contrary, NS3:1 had no sharp peaks due to complete amorphous structure. However, NS3:1-FA exhibited broad and weak peaks between $2\theta = 5^\circ$ and 30° , indicating the presence of crystalline peaks of FA in the surface of NS3:1-FA and suggesting the amorphous structure of NS3:1-FA, supported by other studies employing FA conjugation [140,220]. These findings suggested that conjugation of FA to NS3:1 was completed.

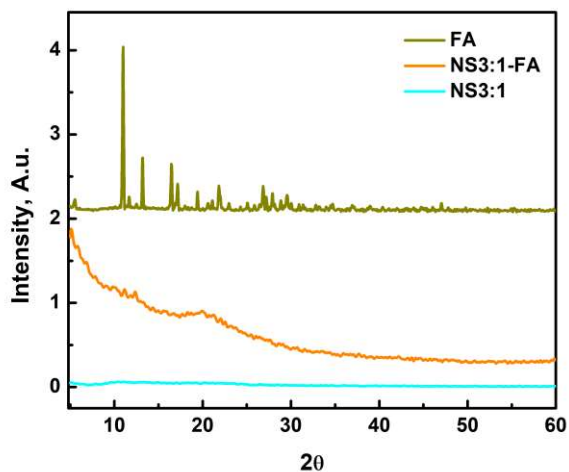


Figure 48. XRD analysis for FA, NS3:1 and NS3:1-FA conjugate.

3.4.5. Thermal Analysis for NS3:1-FA Conjugate

TGA and DSC analyses were conducted on the samples to evaluate their thermal durability, decomposition behavior, and to gain insights into their composition [129,163]. Figure 49 illustrates TGA and DSC diagrams for NS3:1, FA, NS3:1-FA and NS3:1-FA physical mixture (PHY). According to TGA diagram (Figure 49.a) the weight loss for FA primary observed at 112 °C and 210 °C corresponds to water loss and degradation of glutamic acid, pterin and p-amino benzoic acid of FA, respectively [204]. In parallel, NS3:1 had weight loss at 75 °C and 215 °C for moisture removal and degradation, respectively. The diagram of NS3:1-FA had peak for FA degradation at 210 °C, which was related with the glutamic acid unit of FA [204]. During the TGA analysis, FA lost 53% of its original weight. When FA was conjugated to NS3:1, weight loss shifted from 74% for NS3:1 to 70% for NS3:1-FA. This was due to the conjugation enhancing the molecular weight of the NS3:1 and reduced the weight loss upon TGA analysis. Thermal stability enhanced upon FA conjugation [140,214]. In addition, the diagram for NS3:1-FA-PHY was different than the NS3:1-FA, showing the chemical interaction in terms of thermal stability. DSC diagrams for NS3:1, FA and NS3:1-FA conjugate was illustrated in Figure 49.b. NS3:1 had one endotherm at 96 °C and one exotherm at 237 °C referring to water loss and crystallization, respectively [178]. On the other hand, FA had one endothermic peak at 210 °C, reflecting the melting of glutamic acid units of FA [221].

Thus, the diagram for NS3:1-FA possessed one endotherm at 95 °C for water evaporation and exotherm at 227 °C for crystallization. The conjugation of FA to NS3:1 reduced the temperature of crystallization peak from 237 °C to 227 °C, indicating their different crystalline nature. These finding suggested that conjugation of FA reduced the energy need to arrange the crystalline structure in NS3:1-FA, due to their slightly crystallinity compared to NS3:1 (which was completely amorphous) also proven by the XRD results. These thermal analysis prove the conjugation of FA to NS3:1.

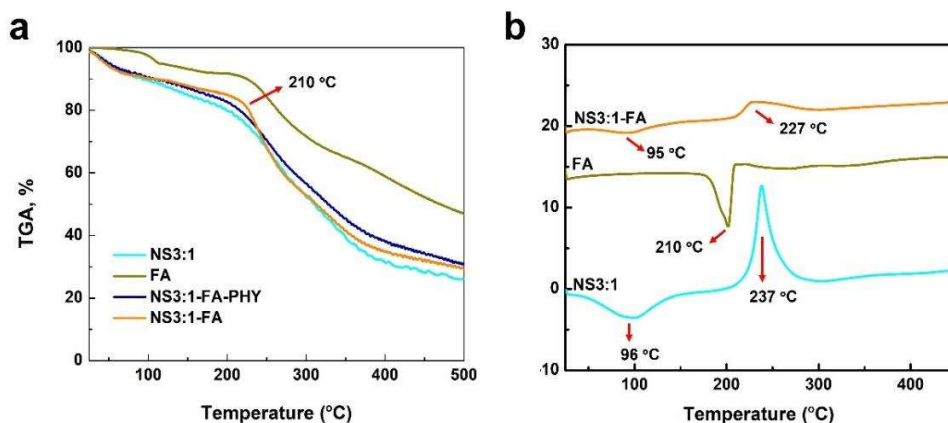


Figure 49. a) TGA analysis for NS3:1, FA, NS3:1-FA and NS3:1-FA physical mixture (PHY) and b) DSC diagrams for NS3:1, FA, NS3:1-FA.

3.4.5. SEM analysis for NS3:1-FA Conjugate

SEM analysis was performed on the specimens in order to reveal their morphological differences and shown in Figure 50. NS3:1 has an unorganized structure. On the other hand, FA displayed laminar stacking structures [218]. The conjugation of FA to NS3:1 did not significantly alter the morphology of NS3:1, which NS3:1-FA exhibited irregular structure. Similar observations were also reported once FA was conjugated to zinc oxide NPs [222], chitosan NPs [215], and iron oxide NPs [220], where no significant change in their morphology after conjugation was reported.

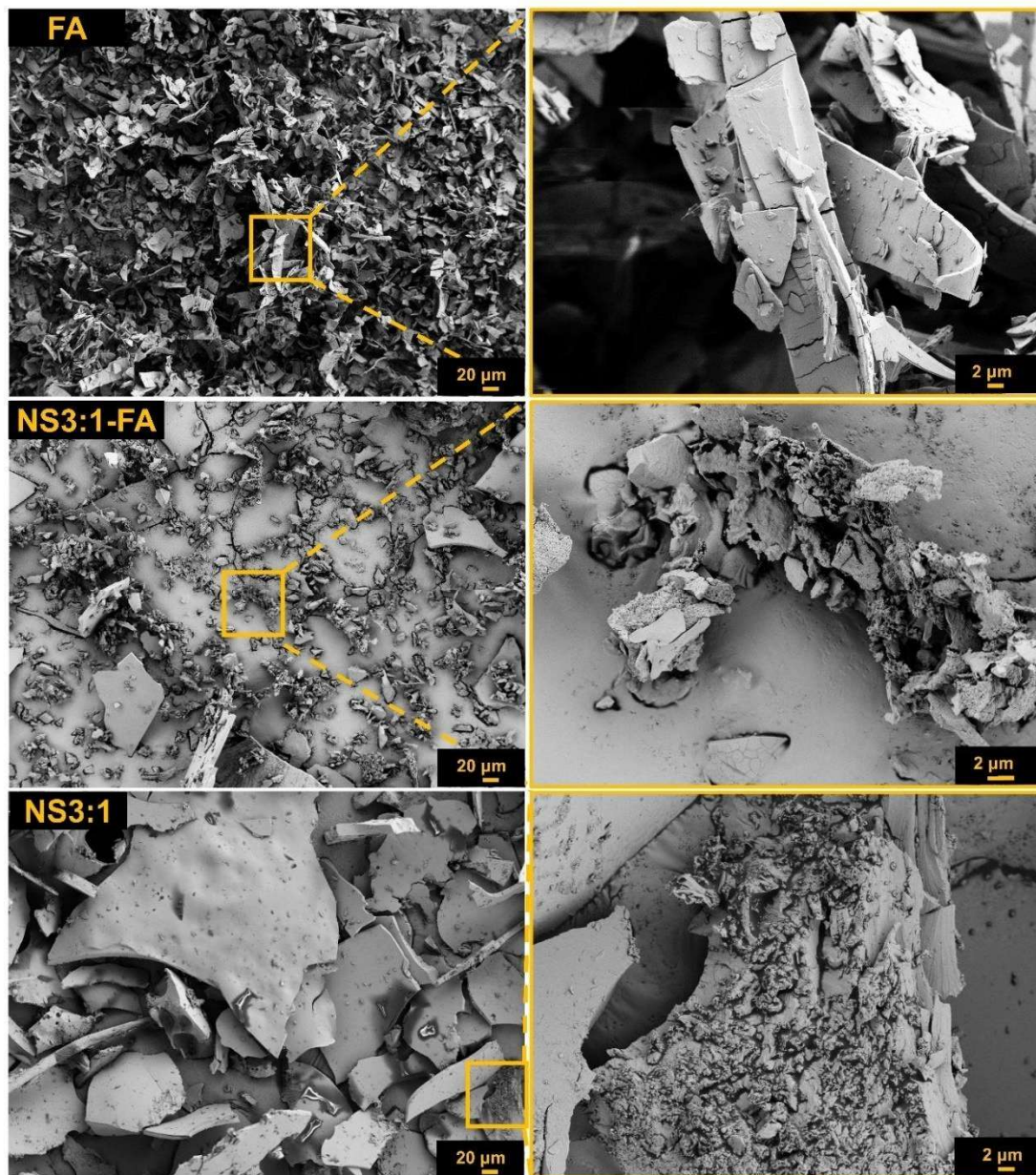


Figure 50. SEM images of NS3:1, FA and NS3:1-FA.

3.4.6. TEM Analysis for NS3:1-FA Conjugate

TEM analysis was performed on the NS3:1-FA conjugate in order to investigate their morphology and dry size. Figure 51 illustrates TEM images of NS3:1-FA with different magnifications. The dry size of NS3:1-FA was measured as 43.42 nm. This was quite low compared to DLS data (219.9 nm), since DLS measures the hydrodynamic size of the NPs. The difference between TEM and DLS in terms of size also gives information about

their swelling ability, whereby these particles were able to hold water in their structure [111,128,177]. The conjugation of FA increased the dry size of NS3:1, which was also parallel with the DLS data. In addition, particles with spherical shape was observed with TEM analysis, showing that FA conjugation did not alter the spherical structure of NS3:1, as also reported for polymeric NPs conjugated with FA [223,224].

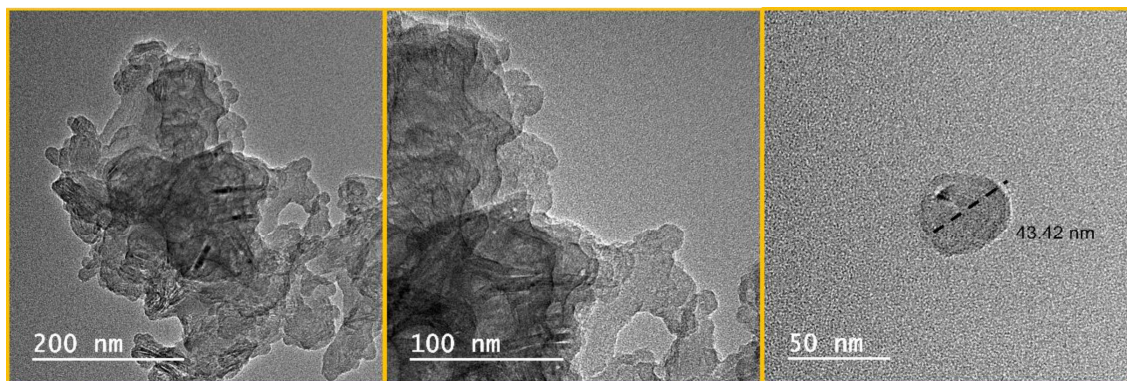


Figure 51. TEM images of NS3:1-FA with different magnifications.

3.5. Dox Loading to NS3:1-FA

Dox loading to NS3:1-FA was confirmed with EE% and LC, FTIR, DLS/Zeta measurements and DSC analysis. According to Equation 1 and 2, EE% and LC for Dox were calculated as 51.8% and 0.051 (mg/mg). The conjugation of FA to NS3:1 slightly reduced the EE% and LC. This is related with the steric hindrance of FA molecules, restricting the drug loading, also confirmed by several reports [225–227].

3.5.1. FTIR Analysis for NS3:1-FA-Dox

FTIR analysis was conducted to assess the chemical composition of the specimens and shown in Figure 52. The spectrum of NS3:1-FA and Dox were explained in previous sections. More specifically, the spectrum of Dox had bands at 3330 cm^{-1} for N-H stretching, 2935 cm^{-1} for C-H stretching and 1414 cm^{-1} for C=C double bond ring stretch (Figure 52.a) [228]. The spectrum of NS3:1-FA-Dox exhibited bands representative of

both NS3:1-FA and Dox. A broad peak appeared at 3370 cm^{-1} in the spectrum of NS3:1-FA-Dox, due to the N-H stretching of Dox. Thus, the intensity of peak at 2935 cm^{-1} became amplified due to C-H stretching of Dox at 2935 cm^{-1} (Figure 52.b) [185]. In addition, a new peak was recorded at 1410 in the spectrum of NS3:1-FA-Dox, due to C=C double bond ring stretch at 1414 cm^{-1} [228]. Lastly, a new peak independent from each sample was shown at 950 cm^{-1} . Furthermore, the spectrum of NS3:1-FA-Dox physical mixture was quite different from the encapsulated version (NS3:1-FA-Dox), indicating the encapsulation of Dox by NS3:1-FA.

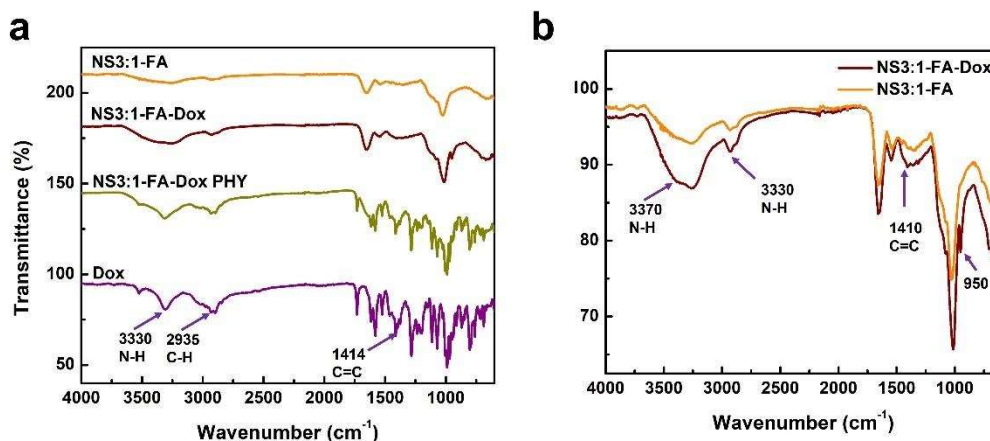


Figure 52. FTIR spectrum of a) NS3:1-FA, NS3:1-FA-Dox, NS3:1-FA-Dox physical mixture (PHY) and Dox, b) NS3:1-FA and NS3:1-FA-Dox.

3.5.2. DSC Analysis for NS3:1-FA-Dox

The thermal characteristics of the materials were examined via a DSC technique [165]. Figure 53 shows DSC diagrams for the specimens. Accordingly, NS3:1-FA had one endothermic peak at $95\text{ }^{\circ}\text{C}$ and one exothermic peak at $227\text{ }^{\circ}\text{C}$, refer to water loss and crystallization, respectively [178]. Dox possessed two endothermic peaks at $228\text{ }^{\circ}\text{C}$ and $243\text{ }^{\circ}\text{C}$, indicating the melting points of the Dox upon heating [193]. Upon encapsulation of Dox, the endothermic peak of NS3:1-FA was increased from $95\text{ }^{\circ}\text{C}$ to $97\text{ }^{\circ}\text{C}$. Thus, Dox incorporation to NS3:1-FA broadened the exothermic peak at $227\text{ }^{\circ}\text{C}$, indicating the incorporation of Dox through NS3:1-FA sample.

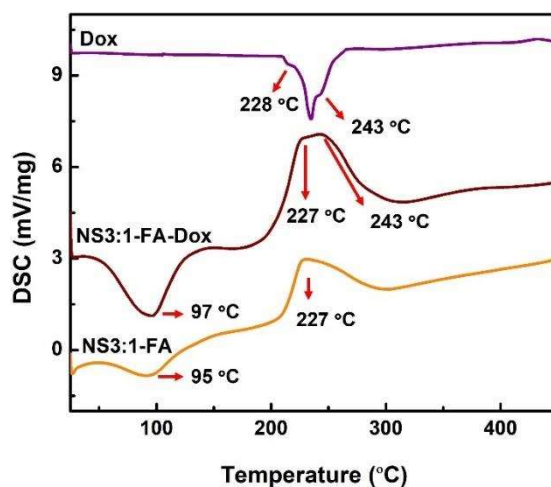


Figure 53. DSC diagrams for NS3:1-FA, NS3:1-FA-Dox and Dox.

3.5.3. DLS/Zeta Analysis for NS3:1-FA-Dox

DLS and Zeta measurements were completed on samples in order to reveal their hydrodynamic size and surface charge upon drug encapsulation. Table 14 illustrates Z-Average (nm), PDI and Zeta potential (mV) values for NS3:1-FA and NS3:1-FA-Dox while Figure 54 indicates size distribution of specimens by intensity. According to Table 14, Dox loading did not alter the hydrodynamic size of the NS3:1-FA, supported by previous reports [229,230]. However, Dox loading altered the surface charge, from -5.8 mV to -2.35 mV, due to the possible interactions between Dox and surface of NS3:1-FA, as also reported by the increase in Zeta potential through Dox loading to NP [188].

Table 14. Z-Average (nm), PDI and Zeta potential (mV) values for NS3:1-FA and NS3:1-FA-Dox.

Sample	Z-Ave (nm)	PDI	Zeta Potential, mV
NS3:1-FA	219.9 ± 7.187	0.1907 ± 0.038	-5.821 ± 0.5272
NS3:1-FA-Dox	220.1 ± 75.64	0.3877 ± 0.1746	-2.35 ± 3.124

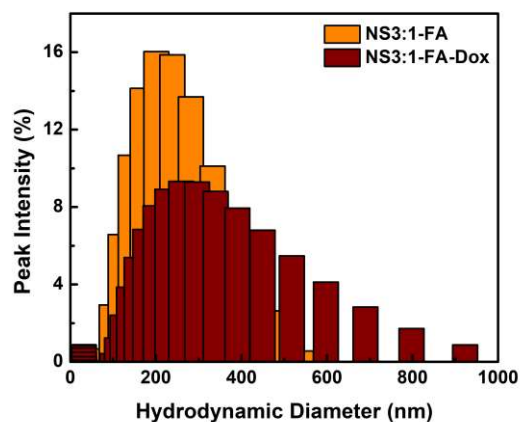


Figure 54. Size distribution by intensity of NS3:1-FA and NS3:1-FA-Dox.

3.5.4. SEM Analysis for NS3:1-FA-Dox

SEM analysis was completed to reveal their morphology and homogeneity. Figure 55 shows SEM images of freeze-dried samples. Dox has irregular morphology and elongated with a smooth surface [194,195]. NS3:1-FA exhibits smaller sized clusters having irregular surface. NS3:1-Dox PHY comprises both NS3:1-FA and Dox flakes. NS3:1-FA-Dox exhibited smoother surface compared to NS3:1, indicating the entrapment of Dox through all the NS3:1, pores of NS3:1 were filled up with Dox. Plus, the morphology of NS3:1-FA-Dox PHY was quite different than the NS3:1-FA-Dox, indicating the encapsulation. Similar observations were recorded for resveratrol loaded carbonyl and carboxylate CD NSs [196] and nifedipine loaded carbonate NS [171] and other study for NS [90].

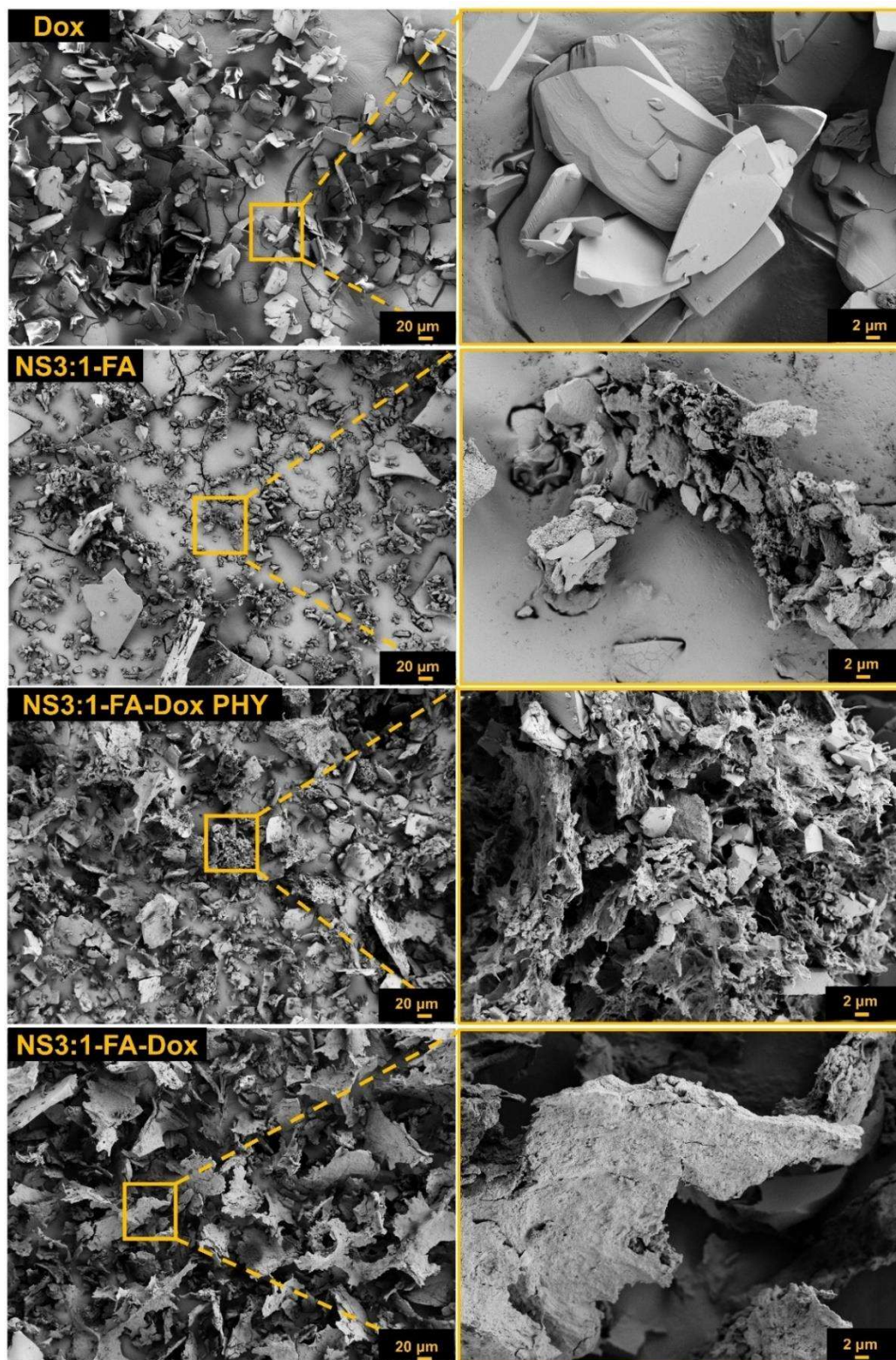


Figure 55. SEM images of Dox, NS3:1-FA, NS3:1-FA-Dox physical mixture (PHY) and NS3:1-FA-Dox.

3.5.5. *In vitro* Drug Release

Drug release assay was performed with NS3:1-FA-Dox loaded with 0.5 mg Dox. NS3:1-FA-Dox formulation was assayed for pH 5.5, 6.5 and 7.4 for 72 h and shown in Figure 56. Accordingly, burst release of Dox from NS3:1-FA-Dox in each pH was observed within 8 h and the release was slowed within 12 h, and consistent release was observed until 72 h. For pH 7.4, 34% of loaded drug was released within 12 h that reached to about 41% of loaded drug during 72 h. For pH 6.5, 56% of loaded Dox was released during first 12 h that reached to about 62% of loaded drug at the end of the test. And for pH 5.5, 64% of loaded drug was released from NS3:1-FA-Dox during 12 h, reached to the 70% after 72 h. This data was consistent with the drug release profile of NS3:1-Dox. Since their loading was slightly different (58% for NS3:1-Dox and 50% for NS3:1-FA-Dox), their release also showed slight differences in terms of released amount, but followed the same pattern, where the conjugation of FA did not alter drug release [231]. The increased release in acidic pH could be related to the breaking of hydrazone bonds in NS3:1 matrix [198]. For pH 7.4, initial burst release could be attributed to the diffusion of Dox from outer layer of the NS3:1-FA where the Dox was poorly entrapped. The following release could be related to the erosion of NS3:1-FA matrix, eventually leading the release [143]. These findings indicate that NS3:1-FA-Dox complex was able to release the encapsulated Dox at neutral and slightly acidic pH values. Drug release was improved once the pH was altered from neutral to 6.5 and 5.5. Especially, pH 5.5 showed greater release as 70% release compared to other pHs. These findings indicate that the Dox release from NS is pH-dependent and shows higher release at acidic pH values ($p < 0.0001$ by ANOVA), supported by the other pH-responsive carriers [202,203].

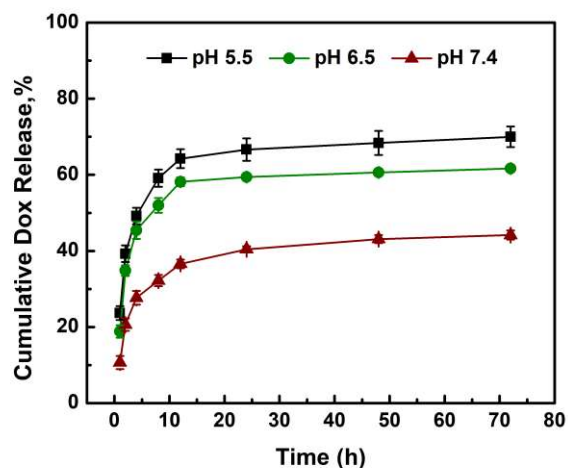


Figure 56. *In vitro* release profile of Dox at different pHs from NS3:1-FA-Dox formulation.

3.6. Cell-Based Assays

The toxicity of Dox loaded formulations were studied with *in vitro* MTT assay against MCF-7 breast cancer cells and L929 fibroblast cells. The internalization and uptake of Dox loaded formulations in MCF-7 breast cancer cells were also studied with confocal microscopy and spectroscopic measurements, respectively.

3.6.1. MTT Assessment

The MTT assay was conducted on MCF-7 and L929 cell lines, representing cancerous and normal cells, respectively, to assess cell viability following treatment with the Dox encapsulated formulations, free Dox and blank NSs. The MTT assay is essential for assessing and validating the efficacy of NS3:1-Dox and NS3:1-FA-Dox inducing cytotoxicity in cancer cells relative to the free drug, while safeguarding control cells from the toxicity associated with free Dox. Validating the toxicity of NS is crucial, particularly in comparison to control cells, as blank NS3:1 and NS3:1-FA is not intended to eliminate any cell type. The concentration of specimens was established according to the free Dox

concentration. The NS3:1-Dox concentration was determined based on the quantity of NS3:1-Dox that corresponded to the encapsulated Dox. For an 8 μM concentration, 8 μM free Dox (4.6 $\mu\text{g}/\text{ml}$), 8 μM encapsulated Dox (equivalent to 80 $\mu\text{g}/\text{ml}$ for NS3:1-Dox and 96 $\mu\text{g}/\text{ml}$ for NS3:1-FA-Dox), and an equal amount of blank NSs (80 $\mu\text{g}/\text{ml}$ of NS3:1 and 96 $\mu\text{g}/\text{ml}$ of NS3:1-FA for the 8 μM concentration) were employed.

The survival of MCF-7 cells was assessed using MTT assay following treatment with free Dox, NS3:1-Dox, and blank NS3:1, NS3:1-FA-Dox and NS3:1-FA for 24 h, as illustrated in Figure 57. Figure 57.a shows MCF-7 cell viability after 24 h treatment with Dox, NS3:1-Dox and NS3:1-FA-Dox. Dox is able to reduce MCF-7 cell viability in a dose-dependent manner. Viability was recorded as 31.6% for 8 μM concentration of free Dox, while 97.3% was recorded for 0.125 μM concentration. This is because Dox kills cancer cells by inducing several events which are mainly the DNA intercalation and inhibition of Topoisomerase II activity to block DNA repair and inducing reactive oxygen species to drive apoptosis [232]. In addition to that, the viability values of MCF-7 cells treated with 8 μM and 0.125 μM NS3:1-Dox were recorded as 26.5% and 86.5%, respectively. According to these findings and Figure 57.a, the toxicity of NS3:1-Dox was moderately higher compared to free Dox, but did not reach the statistical significance, except for 2 μM concentration (* $p < 0.05$ by ANOVA). Therefore, it is concluded that NS3:1-Dox showed same inhibitory effect with free Dox against MCF-7 cells after 24 h incubation, also supported by other studies [233–235]. Figure 57.a also indicates the significant difference in cell viability once Dox is encapsulated with the NS3:1-FA, enhancing its toxicity in each concentration compared to free Dox, as also indicated by several studies [227,236,237]. This improvement was linked with the targeted delivery enabled by folate receptor binding, which is overexpressed on many breast cancer cells [238]. Moreover, no significant difference in cell viability was observed once Dox was encapsulated with FA bound and FA free NS3:1, although there were slight differences, they did not meet the criteria for statistical significance. Figure 57.b shows that NS3:1 and NS3:1-FA are not toxic to the MCF-7 cells which is confirmed by cell viability over 90% [239].

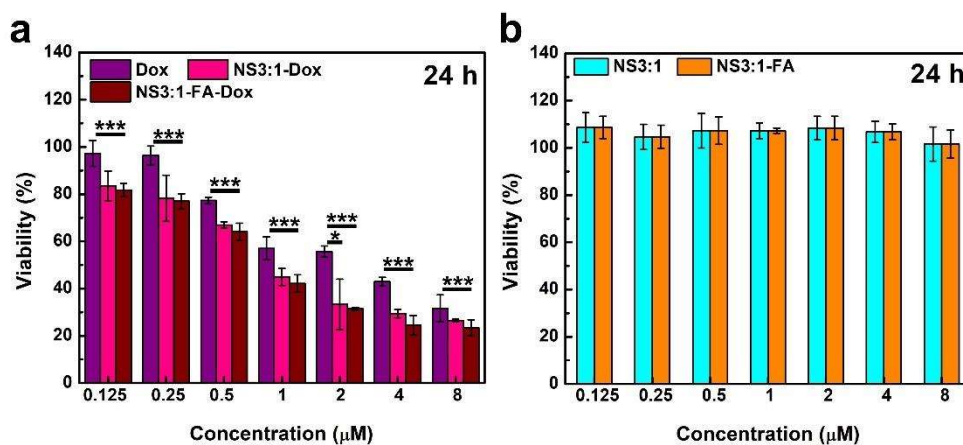


Figure 57. MTT assays for MCF-7 cells treated with a) Dox, NS3:1-Dox, NS3:1-FA-Dox, b) NS3:1 and NS3:1-FA. For an 8 μM concentration, 8 μM free Dox (4.6 μg/ml), 8 μM encapsulated Dox (equivalent to 80 μg/ml for NS3:1-Dox and 96 μg/ml for NS3:1-FA-Dox), and an equal amount of blank NSs (80 μg/ml of NS3:1 and 96 μg/ml of NS3:1-FA) were utilized in MTT assay as higher concentration. * $p < 0.05$; *** $p < 0.0001$ by ANOVA.

As control, L929 cells were subjected to MTT assay to show the protection of normal cells from cellular death caused by free drug. Figure 58 shows cell viability in which L929 cells were treated for 24 h with defined samples. It was observed that, blank NS3:1 and NS3:1-FA is not toxic to control cells, meaning that the cell viability is over 90% in all concentration confirming that they are biocompatible [88]. Meanwhile, Dox was toxic to the cells, reducing their viability. According to Figure 58, cell viability was higher in each concentration of encapsulated Dox (NS3:1-Dox and NS3:1-FA-Dox), although the difference is statistically significant in high concentrations (2 μM and 4 μM of free and encapsulated Dox). Thus, no effect of the presence of FA on the surface of NS3:1 on control cell viability was observed. These findings indicate that encapsulation of Dox via NSs could either reduce or keep constant of control cell viability [181,240,241].

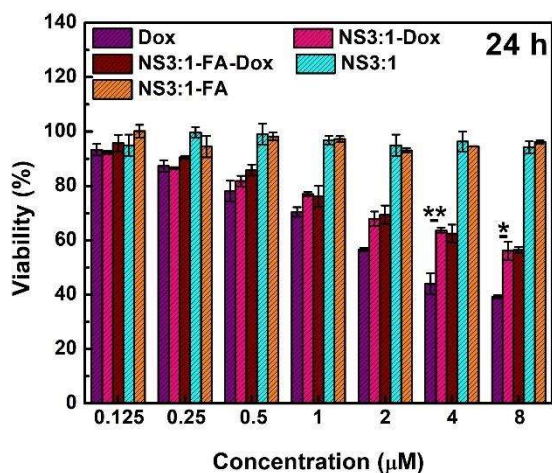


Figure 58. MTT assays for L929 cells treated with Dox, NS3:1-Dox, NS3:1-FA-Dox and blank NS3:1 and NS3:1-FA for 24 h. For an 8 µM concentration, 8 µM free Dox (4.6 µg/ml), 8 µM encapsulated Dox (equivalent to 80 µg/ml for NS3:1-Dox and 96 µg/ml for NS3:1-FA-Dox), and an equal amount of blank NSs (80 µg/ml of NS3:1 and 96 µg/ml of NS3:1-FA) were utilized in MTT assay as higher concentration. * $p < 0.05$; ** $p < 0.005$ by ANOVA.

Figure 59 shows the survival of MCF-7 cells treated with free Dox, NS3:1-Dox, and blank NS3:1, NS3:1-FA-Dox and NS3:1-FA for 48 h. Figure 59.a shows MCF-7 cell viability after 48 h treatment with Dox, NS3:1-Dox and NS3:1-FA-Dox. Dox is able to reduce MCF-7 cell viability in dose-dependent manner [232]. In addition, NS3:1-Dox showed significant toxicity compared to free Dox, especially in the concentration lower than the 2 µM. These findings suggest that Dox can be more internalized by the NS3:1-Dox compared to the free Dox, and might be able to protect Dox from inactivation or extrusion, yielding low doses more effective compared to higher doses (more than 1 µM) on killing MCF-7 cancer cells [82]. Significant difference in cell viability was observed once Dox is encapsulated with the NS3:1-FA, enhancing its toxicity in lower concentrations (2 µM and lesser ones) compared to free Dox. In other words, at high concentration of Dox and due to its high toxicity effect nearly the same cytotoxicity result was observed, while by decreasing the concentration drug loaded samples showed higher toxicity results confirmed the effectiveness of targeted nanocarrier in enhancing drug delivery into cancer cells. The other interesting point was that by increasing time of incubation, the toxicity effect of drug loaded NSs was enhanced that could be related to increasing amounts of

drug inside the cells. Indeed, by increasing exposure time, more amounts of NSs could be internalized into the cells that could be exposed with lower pH of early endosomes and released their therapeutic compounds. Moreover, increasing the time led to change in pH of cells microenvironment to weak acidic pH, resulted from the release of cells' byproducts into the environment, that induced drug release in the microenvironment of cells and so improved cytotoxicity effect [242]. Thus, there was no difference between the cell viability once they are exposed to NS3:1-Dox and NS3:1-FA-Dox. Figure 59.b illustrates the cell survival after the treatment with bare NS3:1 and NS3:1-FA. These sponges had no toxicity effect was observed on MCF-7 cells, but also viability of cells was increased compared with control cells, which confirmed compatibility of NS [239].

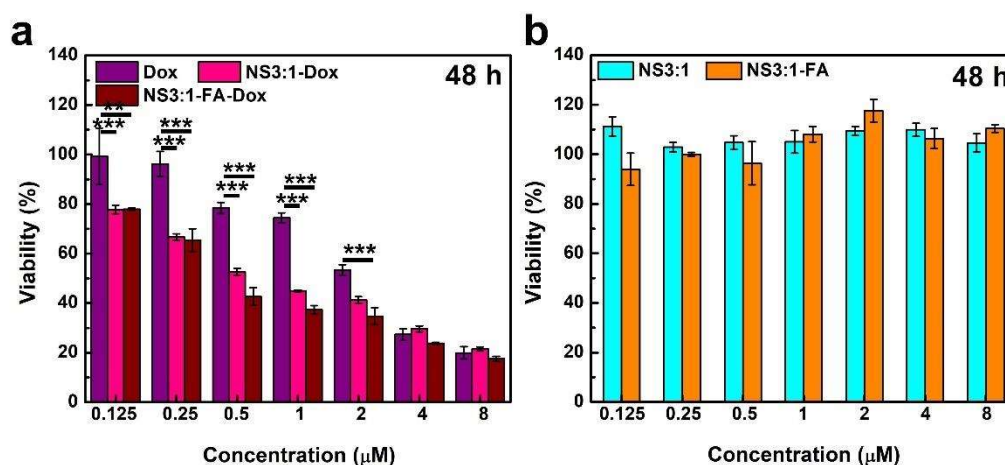


Figure 59. MTT assays for MCF-7 cells treated with a) Dox, NS3:1-Dox, NS3:1-FA-Dox, b) blank NS3:1 and NS3:1-FA. For an 8 µM concentration, 8 µM free Dox (4.6 µg/ml), 8 µM encapsulated Dox (equivalent to 80 µg/ml for NS3:1-Dox and 96 µg/ml for NS3:1-FA-Dox), and an equal amount of blank NSs (80 µg/ml of NS3:1 and 96 µg/ml of NS3:1-FA) were utilized in MTT assay as higher concentration. ***p < 0.0001 by ANOVA.

To confirm the effect of pH on samples, different concentrations of NS3:1-Dox and NS3:1-FA-Dox samples were exposed with cancer cells in normal and acidic pH (Figure 60) [243,244]. According to the results of this test, difference in cell viability arose when the pH of the medium was altered from neutral to acidic (pH 6.5), that confirmed pH-responsiveness of fabricated carrier. All of these findings suggest the synergistic effect of

both FA conjugation and pH alteration were responsible for high toxicity effect seen after 48 h.

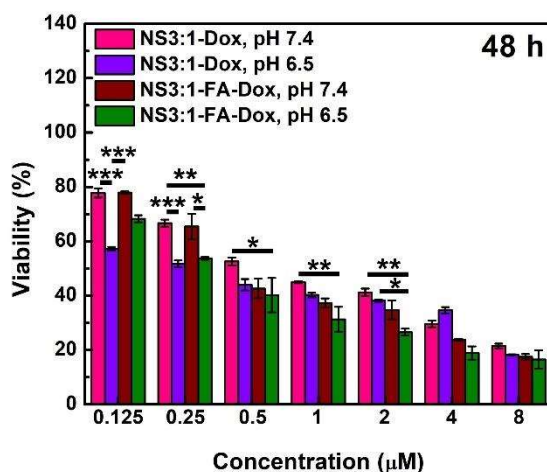


Figure 60. MTT assays for MCF-7 cells treated NS3:1-Dox and NS3:1-FA-Dox at neutral and acidic pH. For an 8 µM concentration, 8 µM free Dox (4.6 µg/ml) and 8 µM encapsulated Dox (equivalent to 80 µg/ml for NS3:1-Dox and 96 µg/ml for NS3:1-FA-Dox) were utilized in MTT assay as higher concentration. * $p < 0.05$; ** $p < 0.005$. *** $p < 0.0001$ by ANOVA.

Figure 61 shows cell viability of L929 cells which were treated 48 h with defined samples. It was observed that, blank NS3:1 and NS3:1-FA were not toxic to control cells, and showed cell viability over 90% in all concentration that confirmed their biocompatibility [88]. Meanwhile, Dox was toxic to the cells, reducing their viability. According to Figure 61, cell viability was significantly (** $p < 0.0001$ by ANOVA) higher in encapsulated Dox, compared to free Dox, that could be related to the lower amounts of available drug. Indeed, in here drugs were encapsulated inside the NSs and thus not completely exposed with cells. The observed toxicity effect was also related to the drug released from the carrier, as confirmed by drug release study. The difference in viability was also consistent with treatment of NS3:1-FA-Dox sample (Figure 61). It is also concluded that FA conjugation did not alter the toxicity of these formulations against L929. This is because these control cells are not sensitive to folate, they do not express folate receptors as much as cancer cells, therefore, they become insensitive to FA presence [245,246].

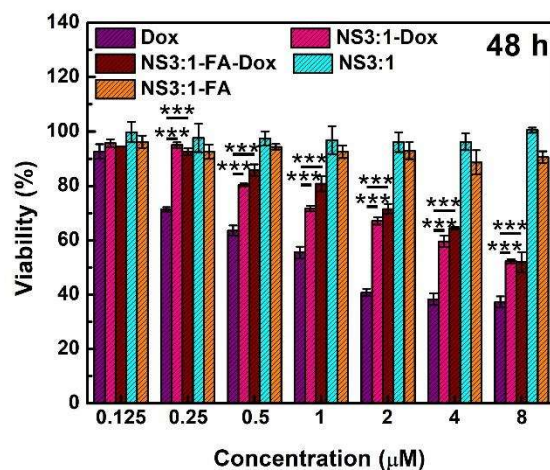


Figure 61. MTT assays for L929 cells treated with a) Dox, NS3:1-Dox, and blank NS3:1 and b) Dox, NS3:1-FA-Dox and NS3:1-FA for 48 h. For an 8 µM concentration, 8 µM free Dox (4.6 µg/ml), 8 µM encapsulated Dox (equivalent to 80 µg/ml for NS3:1-Dox and 96 µg/ml for NS3:1-FA-Dox), and an equal amount of blank NSs (80 µg/ml of NS3:1 and 96 µg/ml of NS3:1-FA) were utilized in MTT assay as higher concentration. ***p < 0.0001 by ANOVA.

According to the results of MTT assay, IC₅₀ samples were determined which are outlined in Table 15. Accordingly, drug loaded NSs showed much lower IC₅₀ concentration than free drug that confirmed the effectiveness of NS in enhancing therapeutic performance of Dox. Moreover, the effectiveness of targeting agent in reducing IC₅₀ of drug loaded NS (0.82 µM for NS3:1-Dox and 0.31 µM of NS3:1-FA-Dox at 48 h under neutral pH) was also confirmed based on the results, confirming the effectiveness of FA conjugation [237,247]. Therefore, FA conjugated NS was better to kill MCF-7 cells having low dose of IC₅₀ value, enhancing the therapeutic efficiency [149,248].

Table 15. IC₅₀ values for Dox, NS3:1-Dox and NS3:1-FA-Dox with their corresponding free or encapsulated Dox amount as molarity against MCF-7 cells. The concentration of each specimen for defined IC₅₀ value was also shown as µg/ml independent of the Dox molarity.

Sample		24 h	48 h, pH 7.4	48 h, pH 6.5
Dox (µM)	Dox	2.56	2.12	-
	NS3:1-Dox	1.08	0.82	0.56
	NS3:1-FA-Dox	1.31	0.31	0.33
µg/ml	Dox	1.47	1.22	-
	NS3:1-Dox	13.01	10	6.83
	NS3:1-FA-Dox	15.78	3.8	3.97

3.6.2. Confocal Analysis for Internalization

The uptake of the Dox into tumor cells is a crucial step for its cytotoxic effect, as Dox must reach the nucleus to exert its anti-cancer activity through DNA intercalation [88]. In this part, MCF-7 cells were treated with NS3:1-Dox, NS3:1-FA-Dox and free Dox to evaluate cellular internalization. After treatment, the cells were stained with Hoechst to label the nucleus (blue fluorescence), while Dox exhibited inherent red fluorescence. MCF-7 cells were incubated with 1 µM concentrations of both free and encapsulated Dox for 2 and 6 h followed by CLSM analysis to observe Dox and nuclear localization [88,249]. As shown in Figure 62, after 2 h of incubation, Dox fluorescence was visible within the cytoplasm of MCF-7 cells for all Dox formulations [250]. Only negligible nuclear fluorescence was seen with free Dox since it is experiencing diffusion [251,252], and no nuclear localization of NS3:1-Dox and NS-FA-Dox was observed at this time. Although free Dox is capable of diffusing into the nucleus, encapsulation did not alter its internalization although active transport mechanisms involve in such drug-loaded systems [80]. Once the incubation time enhanced to 6 h, the Dox fluorescence is evident in the nucleus for both free Dox and encapsulated Dox specimens, although Dox fluorescence was observed at nucleus at 8 h in another report [253]. No significant difference in overall fluorescence intensity between free and encapsulated was noted on

the contrary to a report [254], due to equal molar application of free and encapsulated Dox, thus only internalization was observed.

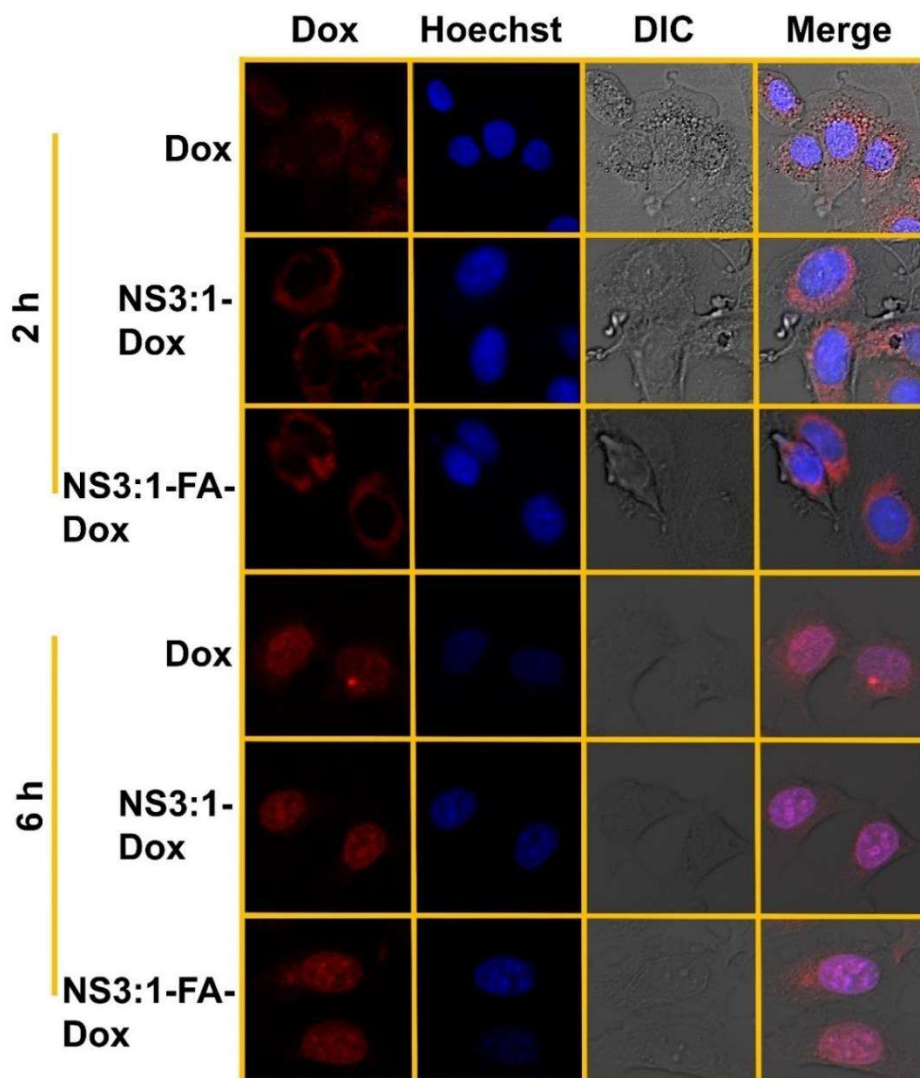


Figure 62. Confocal microscopy images of MCF-7 cells treated with Dox formulations for 2 h and 6 h.

3.6.3. Cellular Uptake Studies

The uptake of the Dox into tumor cells is a crucial step for its cytotoxic effect, as the enhanced Dox uptake is evident for anti-cancer activity. Therefore, Dox uptake study was performed in MCF-7 cells treated with equivalent molar (1 μ M) of Dox, NS3:1-Dox and

NS3:1-FA-Dox for 2 h and 6 h. After the treatment, cells were lysed for internalized Dox measurement using Florescence spectrophotometer [255]. Calibration curves for each specimen were also generated by dispersing each specimen in control cell lysate and then measuring the Dox florescence [148]. Dox cellular uptake (%) was calculated by dividing the amount of internalized Dox (free and encapsulated) in cell lysate to initial amount of free or encapsulated Dox added to cell media [149]. The cell number for each specimen was also counted for treated wells after 2 h and 6 h thus the change in the cell number was negligible (data not shown). Figure 63 illustrates cellular uptake of Dox formulations after 2 h and 6 h incubation with MCF-7 cells. Accordingly, after 2 h incubation, cellular uptake was recorded as 38% for Dox, 69% for NS3:1-Dox and 72% for NS3:1-FA-Dox. The cellular uptake further increased once the incubation was extended to 6 h as parallel to the 2 h results. Once the Dox was encapsulated by NS3:1, the uptake was significantly amplified. The conjugation of FA slightly enhanced the uptake; however, it did not reach statistical significance. Therefore, it was concluded that encapsulation of Dox via NS3:1 and NS3:1-FA significantly enhanced the drug uptake, as also proven by several studies [138,148,254,256]. Thus, the further incubation of cells with NS3:1-Dox and NS3:1-FA-Dox specimen yield similar cellular uptake at 6 h. This might be related to the accumulation of NS3:1-FA-Dox through the surface of MCF-7 cells and although it has FA on the surface, it might be blocking the folate-mediated internalization and showing reduced endocytosis due to their increased hydrodynamic size and slightly negative charge compared to NS3:1-Dox [257,258]. Therefore, both NS3:1-Dox and NS3:1-FA-Dox showed same cellular uptake at 6 h incubation.

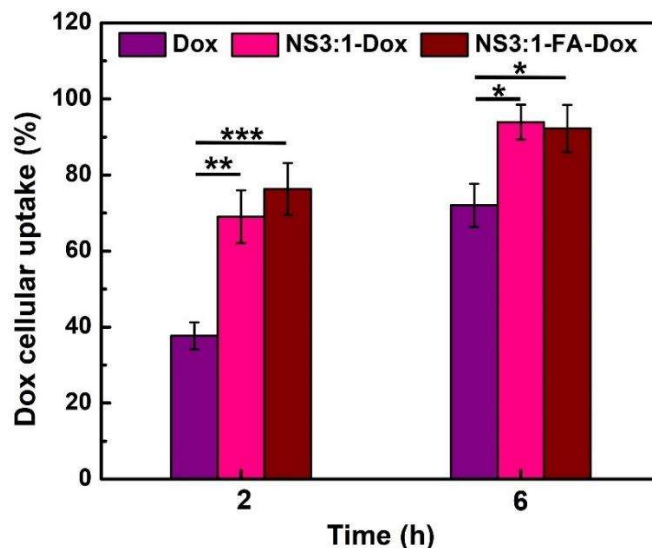


Figure 63. Cellular uptake of Dox, NS3:1-Dox and NS3:1-FA-Dox after 2 h and 6 h incubation with the MCF-7 cells. * $p < 0.05$; ** $p < 0.005$. *** $p < 0.0001$ by ANOVA.

Limitations for prepared NSs

CD NSs are versatile materials in drug delivery systems; however, they contain several limitations in terms of their characterizations and applications. The following paragraphs will outline some limitations associated with as-prepared NSs.

- NSs are reported to have nanosized pores in their structures. For CD NSs, these pores are thought to be derived from the CD cavity. These cavities cannot be determined by imaging techniques, as these pores are below 1 nm, collapsed during drying, and also covered with crosslinkers. Brunauer-Emmett-Teller (BET) analysis was used to measure the porosity of CD NSs; however, the intrinsic property of CDs limits the use of BET in porosity measurements. Accurate BET measurements cannot be completed for CD NSs due to a complex, cross-linked network and potential non-uniform pore structures of CD NSs. Therefore, reliable BET data cannot be obtained since CDs have moisture content. Therefore, indirect methods were utilized to indicate their porosity, since crosslinked CD polymers are called NSs in the literature [259].
- CD NSs were prone to aggregate in aqueous environments for long-term storage, limiting their biomedical use. Although they possessed good PDI values, SEM and TEM analyses indicated their aggregation behavior in dry conditions, which might limit their use in cell-based applications.

- There are few studies showing the conjugation of FA or cholesterol to CD NSs. The conjugation of slightly hydrophobic molecules to CD NSs was limited due to the inclusion capacity of parent CDs, thus favoring the encapsulation of defined molecules as well as the conjugation of them. Therefore, control over the structure in terms of conjugation was limited for this system.
- The prepared blank NSs were characterized by the TEM analysis, showing their morphology. However, drug-loaded NSs were not characterized by the TEM. Other study also indicated that drug loading did not alter the morphology [171]. The change in the size was assayed with DLS analysis.
- Dox has a broad range of excitation wavelengths (350–600 nm), with excitation maxima at 488 nm. Although this property makes it easier to observe Dox through fluorescence microscopy, it also limits its co-administration with several other molecules, such as Annexin V, propidium iodide, or even with the oxidative stress marker Dichlorodihydrofluorescein diacetate, due to the overlapping of excitation and emission wavelengths. Therefore, Dox-loaded NSs were usually directly analyzed with Dox fluorescence, and additionally the nucleus was stained.
- The cellular uptake of NSs with Dox was performed for short periods of time, although the toxicity assays were done after 24 h. This is due to the observation of initial dynamics of the NS internalization to evaluate the rate of NS uptake at early phases by visualization of Dox signal. Therefore, it was considered to be a crucial step before applying long-term cell-based analyses to evaluate the effectiveness of the carriers [260]. Thus, since Dox was metabolized by the cells, the measurement of Dox as well as their metabolites requires additional measurement techniques [261]. Therefore, the internalization was observed at early phases of incubation with NS-Dox formulations.

4. Conclusion

In this thesis, pH-responsive CD NS was generated by a novel method comprising oxidized β -CD synthesis, followed by crosslinking with ADH. This simple and original synthesis method enables us to obtain NS with hydrazone bonds. These bonds are pH-labile, and cleavable under acidic pH, thus providing pH-responsiveness to our system. The generated NS was utilized for Dox delivery, an anticancer drug currently used in several cancer research. This NS was further decorated with FA, in order to enhance its accumulation inside folate-expressing tumor cells.

A variety of characterization methods and cell-based assays were utilized to evaluate the effectiveness of NS. $^1\text{H-NMR}$ analysis showed the oxidation reaction of β -CD with NaIO_4 . FTIR analysis also confirmed oxidation reaction, as well as NS synthesis, FA conjugation and Dox loading to targeted/non-targeted NS. UV-Vis analysis revealed the oxidation reaction, NS synthesis and FA conjugation. DLS and Zeta potential measurements revealed hydrodynamic size and surface charge of each specimen. The hydrodynamic size of NS was increased with both drug loading and FA conjugation. All NSs showed near zero Zeta potential with uniform size distribution. XRD analysis showed that β -CD has crystalline nature, while oxidize β -CD has semicrystalline structure and NS has an amorphous structure. Thus, XRD also illustrated FA conjugation to NS surface.

TGA and DSC analyses also explored β -CD oxidation, NS synthesis, FA conjugation and drug loading. Accordingly, TGA and DSC curves for each specimen are significantly different from each other, reflecting the chemical reaction and drug encapsulation. The thermal stability enhanced once FA is conjugated to NS. SEM analysis was performed to assess the morphology of freeze-dried NSs. The real morphology/shape of FA-free and FA-conjugated NS were analyzed with TEM, showing spherical shaped NS and FA conjugated NS, while having 30-40 nm dry size. The pH-responsiveness study revealed a decrease in hydrodynamic size under acidic pH due to the cleavage of hydrazone bonds.

Long-term stability showed that NS is not stable in water since CD units are prone to clump together thus increasing the size.

According to *in vitro* drug release assay, Dox release was calculated as 53% and 42% for NS3:1 and NS3:1-FA at neutral pH and enhanced to 76% and 70% at acidic pH, confirming pH-responsive drug release.

MTT assay was performed on MCF-7 as cancer cells and L929 as control cells. The results of the assay revealed that Dox is killing both cancer and control cells in dose- and time-dependent manner. On the contrary, NS formulations are biocompatible, showing cell survival over 90% in each dose. Thus, the encapsulation of Dox with NS further enhanced the toxicity of drug molecules due to specific uptake of the NS. The difference in viability becomes visible once the incubation is extended from 24 h to 48 h. The difference also became visible in lower concentrations, showing that the NS was able to protect the drug from unwanted degradation.

It was revealed that both NS-Dox formulations had higher toxicity compared to free Dox and FA conjugated NS with Dox showed slightly high toxicity against cancer cells. Once the pH of the media altered to acidic pH, the toxicity of both NS-Dox formulations was enhanced, showing pH-responsive anticancer activity. Once MTT performed on the control cells, the toxicity of drug molecules significantly reduced in each dose and time and independent of FA presence, consequence of decreased side effects of the drug molecules. IC_{50} calculations clearly demonstrated the FA impact, which the IC_{50} values for NS3:1-Dox and NS3:1-FA-Dox were calculated as 0.82 μ M and 0.31 μ M (equivalent Dox), respectively. Therefore, it was shown that FA conjugation enhanced the therapeutic efficiency while reducing the IC_{50} value. Confocal analysis showed the internalization of Dox and NS-Dox formulations, which all specimens showed the same localization patterns. Cellular uptake studies indicated that encapsulation enhanced the uptake, almost 2 times of increased Dox in cell lysates were recorded. In light of these findings, we can conclude that this novel pH-responsive CD NS could be an alternative to drug delivery vesicles used in cancer therapy.

5. References

- [1] M. Egeblad, E.S. Nakasone, Z. Werb, Tumors as Organs: Complex Tissues that Interface with the Entire Organism, *Dev. Cell.* 18 (2010) 884–901.
<https://doi.org/10.1016/j.devcel.2010.05.012>.
- [2] G. Cooper, K. Adams, *The cell: a molecular approach*, Oxford University Press, 2022.
- [3] N. Datta, S. Chakraborty, M. Basu, M.K. Ghosh, Tumor Suppressors Having Oncogenic Functions: The Double Agents, *Cells.* 10 (2021).
<https://doi.org/10.3390/cells10010046>.
- [4] M. Sinkala, Mutational landscape of cancer-driver genes across human cancers, *Sci. Rep.* 13 (2023) 12742. <https://doi.org/10.1038/s41598-023-39608-2>.
- [5] E. Bidram, Y. Esmaceli, H. Ranji-Burachaloo, N. Al-Zaubai, A. Zarrabi, A. Stewart, D.E. Dunstan, A concise review on cancer treatment methods and delivery systems, *J. Drug Deliv. Sci. Technol.* 54 (2019) 101350.
<https://doi.org/https://doi.org/10.1016/j.jddst.2019.101350>.
- [6] D. Yang, J. Liu, H. Qian, Q. Zhuang, Cancer-associated fibroblasts: from basic science to anticancer therapy, *Exp. Mol. Med.* 55 (2023) 1322–1332.
<https://doi.org/10.1038/s12276-023-01013-0>.
- [7] M. V Liberti, J.W. Locasale, The Warburg Effect: How Does it Benefit Cancer Cells?, *Trends Biochem. Sci.* 41 (2016) 211–218.
<https://doi.org/10.1016/j.tibs.2015.12.001>.
- [8] J. Winkler, A. Abisoye-Ogunniyan, K.J. Metcalf, Z. Werb, Concepts of extracellular matrix remodelling in tumour progression and metastasis, *Nat. Commun.* 11 (2020) 5120. <https://doi.org/10.1038/s41467-020-18794-x>.
- [9] L. V Yang, Tumor Microenvironment and Metabolism, *Int. J. Mol. Sci.* 18

- (2017). <https://doi.org/10.3390/ijms18122729>.
- [10] X. Guan, Cancer metastases: challenges and opportunities, *Acta Pharm. Sin. B.* 5 (2015) 402–418. <https://doi.org/https://doi.org/10.1016/j.apsb.2015.07.005>.
- [11] A. Carbone, Cancer Classification at the Crossroads, *Cancers (Basel)*. 12 (2020). <https://doi.org/10.3390/cancers12040980>.
- [12] H. Sung, J. Ferlay, R.L. Siegel, M. Laversanne, I. Soerjomataram, A. Jemal, F. Bray, Global Cancer Statistics 2020: GLOBOCAN Estimates of Incidence and Mortality Worldwide for 36 Cancers in 185 Countries, *CA. Cancer J. Clin.* 71 (2021) 209–249. <https://doi.org/https://doi.org/10.3322/caac.21660>.
- [13] R.L. Siegel, K.D. Miller, N.S. Wagle, A. Jemal, Cancer statistics, 2023, *CA. Cancer J. Clin.* 73 (2023) 17–48. <https://doi.org/https://doi.org/10.3322/caac.21763>.
- [14] R.C. Fitzgerald, A.C. Antoniou, L. Fruk, N. Rosenfeld, The future of early cancer detection, *Nat. Med.* 28 (2022) 666–677. <https://doi.org/10.1038/s41591-022-01746-x>.
- [15] D.T. Debela, S.G.Y. Muzazu, K.D. Heraro, M.T. Ndalama, B.W. Mesele, D.C. Haile, S.K. Kitui, T. Manyazewal, New approaches and procedures for cancer treatment: Current perspectives, *SAGE Open Med.* 9 (2021) 20503121211034370. <https://doi.org/10.1177/20503121211034366>.
- [16] R. Kaur, A. Bhardwaj, S. Gupta, Cancer treatment therapies: traditional to modern approaches to combat cancers, *Mol. Biol. Rep.* 50 (2023) 9663–9676. <https://doi.org/10.1007/s11033-023-08809-3>.
- [17] Y. Cao, Q. Ren, R. Hao, Z. Sun, Innovative strategies to boost photothermal therapy at mild temperature mediated by functional nanomaterials, *Mater. Des.* 214 (2022) 110391. <https://doi.org/https://doi.org/10.1016/j.matdes.2022.110391>.
- [18] S.A. Atallah-Yunes, M.J. Robertson, Cytokine Based Immunotherapy for Cancer and Lymphoma: Biology, Challenges and Future Perspectives, *Front. Immunol.* 13 (2022). <https://www.frontiersin.org/journals/immunology/articles/10.3389/fimmu.2022.872010>.

- [19] D. Zahavi, L. Weiner, Monoclonal Antibodies in Cancer Therapy, *Antibodies*. 9 (2020). <https://doi.org/10.3390/antib9030034>.
- [20] D. Lin, Y. Shen, T. Liang, Oncolytic virotherapy: basic principles, recent advances and future directions, *Signal Transduct. Target. Ther.* 8 (2023) 156. <https://doi.org/10.1038/s41392-023-01407-6>.
- [21] S. Jin, Y. Sun, X. Liang, X. Gu, J. Ning, Y. Xu, S. Chen, L. Pan, Emerging new therapeutic antibody derivatives for cancer treatment, *Signal Transduct. Target. Ther.* 7 (2022) 39. <https://doi.org/10.1038/s41392-021-00868-x>.
- [22] H. Ghazal, A. Waqar, F. Yaseen, M. Shahid, M. Sultana, M. Tariq, M.K. Bashir, H. Tahseen, T. Raza, F. Ahmad, Role of nanoparticles in enhancing chemotherapy efficacy for cancer treatment, *Next Mater.* 2 (2024) 100128. <https://doi.org/https://doi.org/10.1016/j.nxmater.2024.100128>.
- [23] L. Na, F. Fan, Advances in nanobubbles for cancer theranostics: Delivery, imaging and therapy, *Biochem. Pharmacol.* 226 (2024) 116341. <https://doi.org/https://doi.org/10.1016/j.bcp.2024.116341>.
- [24] P. Mi, Stimuli-responsive nanocarriers for drug delivery, tumor imaging, therapy and theranostics, *Theranostics*. 10 (2020) 4557.
- [25] L. Tairiol, B. Formicola, R.D. Magro, S. Sesana, F. Re, An Update of Nanoparticle-Based Approaches for Glioblastoma Multiforme Immunotherapy, *Nanomedicine*. 15 (2020) 1861–1871. <https://doi.org/10.2217/nnm-2020-0132>.
- [26] M.J. Mitchell, M.M. Billingsley, R.M. Haley, M.E. Wechsler, N.A. Peppas, R. Langer, Engineering precision nanoparticles for drug delivery, *Nat. Rev. Drug Discov.* 20 (2021) 101–124. <https://doi.org/10.1038/s41573-020-0090-8>.
- [27] M. Vassal, S. Rebelo, M.D. Pereira, Metal Oxide Nanoparticles: Evidence of Adverse Effects on the Male Reproductive System, *Int. J. Mol. Sci.* 22 (2021). <https://doi.org/10.3390/ijms22158061>.
- [28] B. Mekuye, B. Abera, Nanomaterials: An overview of synthesis, classification, characterization, and applications, *Nano Sel.* 4 (2023) 486–501. <https://doi.org/https://doi.org/10.1002/nano.202300038>.
- [29] T.-M. Cheng, H.-Y. Chu, H.-M. Huang, Z.-L. Li, C.-Y. Chen, Y.-J. Shih, J.

- Wang-Peng, R.H. Cheng, J.-K. Mo, H.-Y. Lin, K. Wang, Toxicologic Concerns with Current Medical Nanoparticles, *Int. J. Mol. Sci.* 23 (2022).
<https://doi.org/10.3390/ijms23147597>.
- [30] M.A. Beach, U. Nayanathara, Y. Gao, C. Zhang, Y. Xiong, Y. Wang, G.K. Such, Polymeric Nanoparticles for Drug Delivery, *Chem. Rev.* 124 (2024) 5505–5616.
<https://doi.org/10.1021/acs.chemrev.3c00705>.
- [31] B. Begines, T. Ortiz, M. Pérez-Aranda, G. Martínez, M. Merinero, F. Argüelles-Arias, A. Alcludia, Polymeric Nanoparticles for Drug Delivery: Recent Developments and Future Prospects, *Nanomaterials.* 10 (2020).
<https://doi.org/10.3390/nano10071403>.
- [32] R. Gannimani, P. Walvekar, V.R. Naidu, T.M. Aminabhavi, T. Govender, Acetal containing polymers as pH-responsive nano-drug delivery systems, *J. Control. Release.* 328 (2020) 736–761.
<https://doi.org/https://doi.org/10.1016/j.jconrel.2020.09.044>.
- [33] M. Mehta, T.A. Bui, X. Yang, Y. Aksoy, E.M. Goldys, W. Deng, Lipid-Based Nanoparticles for Drug/Gene Delivery: An Overview of the Production Techniques and Difficulties Encountered in Their Industrial Development, *ACS Mater. Au.* 3 (2023) 600–619. <https://doi.org/10.1021/acsmaterialsau.3c00032>.
- [34] Y. Hao, Z. Ji, H. Zhou, D. Wu, Z. Gu, D. Wang, P. ten Dijke, Lipid-based nanoparticles as drug delivery systems for cancer immunotherapy, *MedComm.* 4 (2023) e339. <https://doi.org/https://doi.org/10.1002/mco2.339>.
- [35] Q. Liu, Y.-J. Kim, G.-B. Im, J. Zhu, Y. Wu, Y. Liu, S.H. Bhang, Inorganic Nanoparticles Applied as Functional Therapeutics, *Adv. Funct. Mater.* 31 (2021) 2008171. <https://doi.org/https://doi.org/10.1002/adfm.202008171>.
- [36] G. Unnikrishnan, A. Joy, M. Megha, E. Kolanthai, M. Senthilkumar, Exploration of inorganic nanoparticles for revolutionary drug delivery applications: a critical review, *Discov. Nano.* 18 (2023) 157. <https://doi.org/10.1186/s11671-023-03943-0>.
- [37] J.J. Giner-Casares, M. Henriksen-Lacey, M. Coronado-Puchau, L.M. Liz-Marzán, Inorganic nanoparticles for biomedicine: where materials scientists meet medical research, *Mater. Today.* 19 (2016) 19–28.

<https://doi.org/https://doi.org/10.1016/j.mattod.2015.07.004>.

- [38] L.C. Kennedy, L.R. Bickford, N.A. Lewinski, A.J. Coughlin, Y. Hu, E.S. Day, J.L. West, R.A. Drezek, A New Era for Cancer Treatment: Gold-Nanoparticle-Mediated Thermal Therapies, *Small*. 7 (2011) 169–183.
<https://doi.org/https://doi.org/10.1002/sml.201000134>.
- [39] J. Saleem, L. Wang, C. Chen, Carbon-Based Nanomaterials for Cancer Therapy via Targeting Tumor Microenvironment, *Adv. Healthc. Mater.* 7 (2018) 1800525.
<https://doi.org/https://doi.org/10.1002/adhm.201800525>.
- [40] D.T. Thomas, A. Baby, V. Raman, S.P. Balakrishnan, Carbon-Based Nanomaterials for Cancer Treatment and Diagnosis: A Review, *ChemistrySelect*. 7 (2022) e202202455. <https://doi.org/https://doi.org/10.1002/slct.202202455>.
- [41] C.F. Rodrigues, C.G. Alves, R. Lima-Sousa, A.F. Moreira, D. de Melo-Diogo, I.J. Correia, Chapter 10 - Inorganic-based drug delivery systems for cancer therapy, in: M.R. Singh, D. Singh, J.R. Kanwar, N.S.B.T.-A. and A. in the D. of N.C. for B. and B.A. Chauhan (Eds.), Academic Press, 2020: pp. 283–316.
<https://doi.org/https://doi.org/10.1016/B978-0-12-819666-3.00010-9>.
- [42] Z. Xu, X. Chen, Z. Sun, C. Li, B. Jiang, Recent progress on mitochondrial targeted cancer therapy based on inorganic nanomaterials, *Mater. Today Chem.* 12 (2019) 240–260.
- [43] A. Bianco, K. Kostarelos, M. Prato, Opportunities and challenges of carbon-based nanomaterials for cancer therapy, *Expert Opin. Drug Deliv.* 5 (2008) 331–342. <https://doi.org/10.1517/17425247.5.3.331>.
- [44] A. Moammeri, M.M. Chegeni, H. Sahrayi, R. Ghafelehbash, F. Memarzadeh, A. Mansouri, I. Akbarzadeh, M.S. Abtahi, F. Hejabi, Q. Ren, Current advances in niosomes applications for drug delivery and cancer treatment, *Mater. Today Bio.* 23 (2023) 100837. <https://doi.org/https://doi.org/10.1016/j.mtbio.2023.100837>.
- [45] K. Tiwari, S. Bhattacharya, The ascension of nanosponges as a drug delivery carrier: preparation, characterization, and applications, *J. Mater. Sci. Mater. Med.* 33 (2022) 28. <https://doi.org/10.1007/s10856-022-06652-9>.
- [46] R. Kar, R. Dhar, S. Mukherjee, S. Nag, S. Gorai, N. Mukerjee, D. Mukherjee, R.

- Vatsa, M. Chandrakanth Jadhav, A. Ghosh, A. Devi, A. Krishnan, N.D. Thorat, Exosome-Based Smart Drug Delivery Tool for Cancer Theranostics, *ACS Biomater. Sci. Eng.* 9 (2023) 577–594.
<https://doi.org/10.1021/acsbiomaterials.2c01329>.
- [47] A. Kalra, S. Sharma, Virosomes: A Viral Envelope System Having a Promising Application in Vaccination and Drug Delivery System, in: *Nanopharmaceutical Adv. Deliv. Syst.*, 2021: pp. 145–160.
<https://doi.org/https://doi.org/10.1002/9781119711698.ch7>.
- [48] A. Hedges, Chapter 22 - Cyclodextrins: Properties and Applications, in: J. BeMiller, R.B.T.-S. (Third E. Whistler (Eds.), *Food Sci. Technol.*, Academic Press, San Diego, 2009: pp. 833–851.
<https://doi.org/https://doi.org/10.1016/B978-0-12-746275-2.00022-7>.
- [49] A. Sá Couto, P. Salústio, H. Cabral-Marques, CyclodextrinsCyclodextrins (CDs) BT - Polysaccharides: Bioactivity and Biotechnology, in: K.G. Ramawat, J.-M. Mérillon (Eds.), *Springer International Publishing*, Cham, 2021: pp. 1–36.
https://doi.org/10.1007/978-3-319-03751-6_22-1.
- [50] B.G. Poulson, Q.A. Alsulami, A. Sharfalddin, E.F. El Agammy, F. Mouffouk, A.-H. Emwas, L. Jaremko, M. Jaremko, Cyclodextrins: Structural, Chemical, and Physical Properties, and Applications, *Polysaccharides*. 3 (2022) 1–31.
<https://doi.org/10.3390/polysaccharides3010001>.
- [51] N.G. Hădărugă, G.N. Bandur, I. David, D.I. Hădărugă, A review on thermal analyses of cyclodextrins and cyclodextrin complexes, *Environ. Chem. Lett.* 17 (2019) 349–373. <https://doi.org/10.1007/s10311-018-0806-8>.
- [52] A.P. Sherje, B.R. Dravyakar, D. Kadam, M. Jadhav, Cyclodextrin-based nanosponges: A critical review, *Carbohydr. Polym.* 173 (2017) 37–49.
<https://doi.org/https://doi.org/10.1016/j.carbpol.2017.05.086>.
- [53] G. Crini, S. Fourmentin, É. Fenyvesi, G. Torri, M. Fourmentin, N. Morin-Crini, Cyclodextrins, from molecules to applications, *Environ. Chem. Lett.* 16 (2018) 1361–1375. <https://doi.org/10.1007/s10311-018-0763-2>.
- [54] A. Karthic, A. Roy, J. Lakkakula, S. Alghamdi, A. Shakoory, A.O. Babalghith, T. Bin Emran, R. Sharma, C.M.G. Lima, B. Kim, M.N. Park, S.Z. Safi, R.S. de

- Almeida, H.D.M. Coutinho, Cyclodextrin nanoparticles for diagnosis and potential cancer therapy: A systematic review, *Front. Cell Dev. Biol.* 10 (2022). <https://www.frontiersin.org/journals/cell-and-developmental-biology/articles/10.3389/fcell.2022.984311>.
- [55] A. Cid-Samamed, J. Rakmai, J.C. Mejuto, J. Simal-Gandara, G. Astray, Cyclodextrins inclusion complex: Preparation methods, analytical techniques and food industry applications, *Food Chem.* 384 (2022) 132467. <https://doi.org/https://doi.org/10.1016/j.foodchem.2022.132467>.
- [56] F.M. Bezerra, M.J. Lis, H.B. Firmino, J.G. Dias da Silva, R.D. Curto Valle, J.A. Borges Valle, F.A. Scacchetti, A.L. Tessaro, The Role of β -Cyclodextrin in the Textile Industry—Review, *Molecules.* 25 (2020). <https://doi.org/10.3390/molecules25163624>.
- [57] H.-J. Buschmann, E. Schollmeyer, Applications of cyclodextrins in cosmetic products: A review, *J. Cosmet. Sci.* 53 (2002) 185–192.
- [58] A. Gonzalez Pereira, M. Carpena, P. García Oliveira, J.C. Mejuto, M.A. Prieto, J. Simal Gandara, Main Applications of Cyclodextrins in the Food Industry as the Compounds of Choice to Form Host–Guest Complexes, *Int. J. Mol. Sci.* 22 (2021). <https://doi.org/10.3390/ijms22031339>.
- [59] A. Matencio, S. Navarro-Orcajada, F. García-Carmona, J.M. López-Nicolás, Applications of cyclodextrins in food science. A review, *Trends Food Sci. Technol.* 104 (2020) 132–143. <https://doi.org/https://doi.org/10.1016/j.tifs.2020.08.009>.
- [60] E. Morillo González, Application of cyclodextrins in agrochemistry, (2006).
- [61] S. Wren, T.A. Berger, K.-S. Boos, H. Engelhardt, E.R. Adlard, I.W. Davies, K.D. Altria, R. Stock, The Use of Cyclodextrins as Chiral Selectors BT - The Separation of Enantiomers by Capillary Electrophoresis, in: S. Wren, T.A. Berger, K.-S. Boos, H. Engelhardt, E.R. Adlard, I.W. Davies, K.D. Altria, R. Stock (Eds.), Vieweg+Teubner Verlag, Wiesbaden, 2001: pp. 59–77. https://doi.org/10.1007/978-3-322-83141-5_5.
- [62] S. Shukla, B. Sagar, S. Gupta, Application of Cyclodextrin-Based Nanosponges in Soil and Aquifer Bioremediation BT - Nanosponges for Environmental

- Remediation, in: S. Gulati (Ed.), Springer Nature Switzerland, Cham, 2023: pp. 145–167. https://doi.org/10.1007/978-3-031-41077-2_7.
- [63] Á. Sarabia-Vallejo, M.D. Caja, A.I. Olives, M.A. Martín, J.C. Menéndez, Cyclodextrin Inclusion Complexes for Improved Drug Bioavailability and Activity: Synthetic and Analytical Aspects, *Pharmaceutics*. 15 (2023). <https://doi.org/10.3390/pharmaceutics15092345>.
- [64] C. Qiu, J. Wang, H. Fan, Y. Bai, Y. Tian, X. Xu, Z. Jin, High-efficiency production of γ -cyclodextrin using β -cyclodextrin as the donor raw material by cyclodextrin opening reactions using recombinant cyclodextrin glycosyltransferase, *Carbohydr. Polym.* 182 (2018) 75–80. <https://doi.org/https://doi.org/10.1016/j.carbpol.2017.11.014>.
- [65] A.A. Sandilya, U. Natarajan, M.H. Priya, Molecular View into the Cyclodextrin Cavity: Structure and Hydration, *ACS Omega*. 5 (2020) 25655–25667. <https://doi.org/10.1021/acsomega.0c02760>.
- [66] M. Řezanka, Synthesis of substituted cyclodextrins, *Environ. Chem. Lett.* 17 (2019) 49–63. <https://doi.org/10.1007/s10311-018-0779-7>.
- [67] G. Kali, S. Haddadzadegan, A. Bernkop-Schnürch, Cyclodextrins and derivatives in drug delivery: New developments, relevant clinical trials, and advanced products, *Carbohydr. Polym.* 324 (2024) 121500. <https://doi.org/https://doi.org/10.1016/j.carbpol.2023.121500>.
- [68] V. Aiassa, C. Garnerio, A. Zoppi, M.R. Longhi, Cyclodextrins and Their Derivatives as Drug Stability Modifiers, *Pharmaceutics*. 16 (2023). <https://doi.org/10.3390/ph16081074>.
- [69] B. Gidwani, A. Vyas, A Comprehensive Review on Cyclodextrin-Based Carriers for Delivery of Chemotherapeutic Cytotoxic Anticancer Drugs, *Biomed Res. Int.* 2015 (2015) 198268. <https://doi.org/https://doi.org/10.1155/2015/198268>.
- [70] Y. Liu, T. Lin, C. Cheng, Q. Wang, S. Lin, C. Liu, X. Han, Research Progress on Synthesis and Application of Cyclodextrin Polymers, *Molecules*. 26 (2021). <https://doi.org/10.3390/molecules26041090>.
- [71] X. Li, J. Liu, N. Qiu, Cyclodextrin-Based Polymeric Drug Delivery Systems for

- Cancer Therapy, Polymers (Basel). 15 (2023).
<https://doi.org/10.3390/polym15061400>.
- [72] C. Lou, X. Tian, H. Deng, Y. Wang, X. Jiang, Dialdehyde- β -cyclodextrin-crosslinked carboxymethyl chitosan hydrogel for drug release, Carbohydr. Polym. 231 (2020) 115678.
<https://doi.org/https://doi.org/10.1016/j.carbpol.2019.115678>.
- [73] T.T. Hoang Thi, Y. Lee, S.B. Ryu, H.-J. Sung, K.D. Park, Oxidized cyclodextrin-functionalized injectable gelatin hydrogels as a new platform for tissue-adhesive hydrophobic drug delivery, RSC Adv. 7 (2017) 34053–34062.
<https://doi.org/10.1039/C7RA04137C>.
- [74] F. Caldera, M. Tannous, R. Cavalli, M. Zanetti, F. Trotta, Evolution of Cyclodextrin Nanosponges, Int. J. Pharm. 531 (2017) 470–479.
<https://doi.org/https://doi.org/10.1016/j.ijpharm.2017.06.072>.
- [75] G. Utzeri, P.M.C. Matias, D. Murtinho, A.J.M. Valente, Cyclodextrin-Based Nanosponges: Overview and Opportunities, Front. Chem. 10 (2022).
<https://www.frontiersin.org/article/10.3389/fchem.2022.859406>.
- [76] S. Jemli, D. Pinto, W.G. Kanhounon, F. Ben Amara, L. Sellaoui, A. Bonilla-Petriciolet, F. Dhaouadi, R. Ameri, L.F.O. Silva, S. Bejar, G.L. Dotto, M. Badawi, Green β -cyclodextrin nanosponges for the efficient adsorption of light rare earth elements: Cerium and lanthanum, Chem. Eng. J. 466 (2023) 143108.
<https://doi.org/https://doi.org/10.1016/j.cej.2023.143108>.
- [77] P. Dalal, R. Rao, β -Cyclodextrin nanosponges for enhanced anti-melanoma potential of silymarin with functions of anti-oxidant, anti-inflammatory and anti-tyrosinase, Results Chem. 6 (2023) 101006.
<https://doi.org/https://doi.org/10.1016/j.rechem.2023.101006>.
- [78] B. Pyrak, K. Rogacka-Pyrak, T. Gubica, Ł. Szeleszczuk, Exploring Cyclodextrin-Based Nanosponges as Drug Delivery Systems: Understanding the Physicochemical Factors Influencing Drug Loading and Release Kinetics, Int. J. Mol. Sci. 25 (2024). <https://doi.org/10.3390/ijms25063527>.
- [79] A. Garg, W.-C. Lai, H. Chopra, R. Agrawal, T. Singh, R. Chaudhary, B.N. Dubey, Nanosponge: A promising and intriguing strategy in medical and

pharmaceutical Science, *Heliyon*. 10 (2024) e23303.

<https://doi.org/https://doi.org/10.1016/j.heliyon.2023.e23303>.

- [80] M. Daga, I.A.M. de Graaf, M. Argenziano, A.S.M. Barranco, M. Loeck, Y. Al-Adwi, M.A. Cucci, F. Caldera, F. Trotta, G. Barrera, A. Casini, R. Cavalli, S. Pizzimenti, Glutathione-responsive cyclodextrin-nanosponges as drug delivery systems for doxorubicin: Evaluation of toxicity and transport mechanisms in the liver, *Toxicol. Vitro*. 65 (2020) 104800.
<https://doi.org/https://doi.org/10.1016/j.tiv.2020.104800>.
- [81] M. Argenziano, F. Foglietta, R. Canaparo, R. Spagnolo, C. Della Pepa, F. Caldera, F. Trotta, L. Serpe, R. Cavalli, Biological Effect Evaluation of Glutathione-Responsive Cyclodextrin-Based Nanosponges: 2D and 3D Studies, *Molecules*. 25 (2020). <https://doi.org/10.3390/molecules25122775>.
- [82] F. Trotta, F. Caldera, C. Dianzani, M. Argenziano, G. Barrera, R. Cavalli, Glutathione Bioresponsive Cyclodextrin Nanosponges, *Chempluschem*. 81 (2016) 439–443. <https://doi.org/https://doi.org/10.1002/cplu.201500531>.
- [83] M. Daga, C. Ullio, M. Argenziano, C. Dianzani, R. Cavalli, F. Trotta, C. Ferretti, G.P. Zara, C.L. Gigliotti, E.S. Ciamporcero, P. Pettazzoni, D. Corti, S. Pizzimenti, G. Barrera, GSH-targeted nanosponges increase doxorubicin-induced toxicity “in vitro” and “in vivo” in cancer cells with high antioxidant defenses, *Free Radic. Biol. Med.* 97 (2016) 24–37.
<https://doi.org/https://doi.org/10.1016/j.freeradbiomed.2016.05.009>.
- [84] M. Palminteri, N.K. Dhakar, A. Ferraresi, F. Caldera, C. Vidoni, F. Trotta, C. Isidoro, Cyclodextrin nanosponge for the GSH-mediated delivery of Resveratrol in human cancer cells, *Nanotheranostics*. 5 (2021) 197–212.
<https://doi.org/10.7150/ntno.53888>.
- [85] M.M. Momin, Z. Zaheer, R. Zainuddin, J.N. Sangshetti, Extended release delivery of erlotinib glutathione nanosponge for targeting lung cancer, *Artif. Cells, Nanomedicine, Biotechnol.* 46 (2018) 1064–1075.
<https://doi.org/10.1080/21691401.2017.1360324>.
- [86] M. Argenziano, C. Lombardi, B. Ferrara, F. Trotta, F. Caldera, M. Blangetti, H. Koltai, Y. Kapulnik, R. Yarden, L. Gigliotti, U. Dianzani, C. Dianzani, C. Prandi,

- R. Cavalli, Glutathione/pH-responsive nanosponges enhance strigolactone delivery to prostate cancer cells, *Oncotarget*. 9 (2018) 35813–35829. <https://doi.org/10.18632/oncotarget.26287>.
- [87] M. Russo, M.L. Saladino, D. Chillura Martino, P. Lo Meo, R. Noto, Polyaminocyclodextrin nanosponges: synthesis, characterization and pH-responsive sequestration abilities, *RSC Adv*. 6 (2016) 49941–49953. <https://doi.org/10.1039/C6RA06417E>.
- [88] Y. Dai, Q. Li, S. Zhang, S. Shi, Y. Li, X. Zhao, L. Zhou, X. Wang, Y. Zhu, W. Li, Smart GSH/pH dual-bioresponsive degradable nanosponges based on β -CD-appended hyper-cross-linked polymer for triggered intracellular anticancer drug delivery, *J. Drug Deliv. Sci. Technol*. 64 (2021) 102650. <https://doi.org/https://doi.org/10.1016/j.jddst.2021.102650>.
- [89] M. Pei, J.-Y. Pai, P. Du, P. Liu, Facile Synthesis of Fluorescent Hyper-Cross-Linked β -Cyclodextrin-Carbon Quantum Dot Hybrid Nanosponges for Tumor Theranostic Application with Enhanced Antitumor Efficacy, *Mol. Pharm*. 15 (2018) 4084–4091. <https://doi.org/10.1021/acs.molpharmaceut.8b00508>.
- [90] S. Salazar Sandoval, E. Cortés-Adasme, E. Gallardo-Toledo, I. Araya, F. Celis, N. Yutronic, P. Jara, M.J. Kogan, β -Cyclodextrin-Based Nanosponges Inclusion Compounds Associated with Gold Nanorods for Potential NIR-II Drug Delivery, *Pharmaceutics*. 14 (2022). <https://doi.org/10.3390/pharmaceutics14102206>.
- [91] S. Iravani, R.S. Varma, Nanosponges for Drug Delivery and Cancer Therapy: Recent Advances, *Nanomaterials*. 12 (2022). <https://doi.org/10.3390/nano12142440>.
- [92] M. Tannous, F. Caldera, G. Hoti, U. Dianzani, R. Cavalli, F. Trotta, Drug-Encapsulated CyclodextrinCyclodextrin (CD)NanospongesNanosponges (NSs) BT - Supramolecules in Drug Discovery and Drug Delivery: Methods and Protocols, in: T. Mavromoustakos, A.G. Tzakos, S. Durdagi (Eds.), Springer US, New York, NY, 2021: pp. 247–283. https://doi.org/10.1007/978-1-0716-0920-0_19.
- [93] J. Deng, Q.J. Chen, W. Li, Z. Zuberi, J.X. Feng, Q.L. Lin, J.L. Ren, F.J. Luo, Q.M. Ding, X.X. Zeng, L. Ma, H.Q. Yin, X.M. Zheng, Toward improvements for

carrying capacity of the cyclodextrin-based nanosponges: recent progress from a material and drug delivery, *J. Mater. Sci.* 56 (2021) 5995–6015.

<https://doi.org/10.1007/s10853-020-05646-8>.

- [94] C. Molinar, S. Navarro-Orcajada, I.A. Ansari, I. Conesa, G. Hoti, Y.K. Monfared, A. Matencio, A. Scomparin, J.M. López-Nicolás, R. Cavalli, F. Trotta, Cyclodextrins and Cyclodextrin-Based Nanosponges for Anti-Cancer Drug and Nutraceutical Delivery BT - Targeted Cancer Therapy in Biomedical Engineering, in: R. Malviya, S. Sundram (Eds.), Springer Nature Singapore, Singapore, 2023: pp. 597–629. https://doi.org/10.1007/978-981-19-9786-0_17.
- [95] S.J. Torne, K.A. Ansari, P.R. Vavia, F. Trotta, R. Cavalli, Enhanced oral paclitaxel bioavailability after administration of paclitaxel-loaded nanosponges, *Drug Deliv.* 17 (2010) 419–425. <https://doi.org/10.3109/10717541003777233>.
- [96] B. Moggetti, A. Barberis, S. Marino, G. Berta, S. De Francia, F. Trotta, R. Cavalli, In vitro enhancement of anticancer activity of paclitaxel by a Cremophor free cyclodextrin-based nanosponge formulation, *J. Incl. Phenom. Macrocycl. Chem.* 74 (2012) 201–210. <https://doi.org/10.1007/s10847-011-0101-9>.
- [97] K. A Ansari, S. J Torne, P.R. Vavia, F. Trotta, R. Cavalli, Paclitaxel loaded nanosponges: in-vitro characterization and cytotoxicity study on MCF-7 cell line culture, *Curr. Drug Deliv.* 8 (2011) 194–202.
- [98] S. Swaminathan, L. Pastero, L. Serpe, F. Trotta, P. Vavia, D. Aquilano, M. Trotta, G. Zara, R. Cavalli, Cyclodextrin-based nanosponges encapsulating camptothecin: Physicochemical characterization, stability and cytotoxicity, *Eur. J. Pharm. Biopharm.* 74 (2010) 193–201. <https://doi.org/https://doi.org/10.1016/j.ejpb.2009.11.003>.
- [99] R. Minelli, R. Cavalli, L. Ellis, P. Pettazzoni, F. Trotta, E. Ciamporcero, G. Barrera, R. Fantozzi, C. Dianzani, R. Pili, Nanosponge-encapsulated camptothecin exerts anti-tumor activity in human prostate cancer cells, *Eur. J. Pharm. Sci.* 47 (2012) 686–694. <https://doi.org/https://doi.org/10.1016/j.ejps.2012.08.003>.
- [100] C.L. Gigliotti, R. Minelli, R. Cavalli, S. Occhipinti, G. Barrera, S. Pizzimenti, G. Cappellano, E. Boggio, L. Conti, R. Fantozzi, In vitro and in vivo therapeutic

evaluation of camptothecin-encapsulated β -cyclodextrin nanosponges in prostate cancer, *J. Biomed. Nanotechnol.* 12 (2016) 114–127.

- [101] C.L. Gigliotti, B. Ferrara, S. Occhipinti, E. Boggio, G. Barrera, S. Pizzimenti, M. Giovarelli, R. Fantozzi, A. Chiocchetti, M. Argenziano, N. Clemente, F. Trotta, C. Marchiò, L. Annaratone, R. Boldorini, U. Dianzani, R. Cavalli, C. Dianzani, Enhanced cytotoxic effect of camptothecin nanosponges in anaplastic thyroid cancer cells in vitro and in vivo on orthotopic xenograft tumors, *Drug Deliv.* 24 (2017) 670–680. <https://doi.org/10.1080/10717544.2017.1303856>.
- [102] S. Torne, S. Darandale, P. Vavia, F. Trotta, R. Cavalli, Cyclodextrin-based nanosponges: effective nanocarrier for Tamoxifen delivery, *Pharm. Dev. Technol.* 18 (2013) 619–625. <https://doi.org/10.3109/10837450.2011.649855>.
- [103] D. Jain, T. Gursalkar, A. Bajaj, Nanosponges of an Anticancer Agent for Potential Treatment of Brain Tumors, *Am. J. Neuroprot. Neuroregen.* 5 (2013). <https://doi.org/10.1166/ajnn.2013.1063>.
- [104] N. Rafati, A. Zarrabi, F. Caldera, F. Trotta, N. Ghias, Pyromellitic dianhydride crosslinked cyclodextrin nanosponges for curcumin controlled release; formulation, physicochemical characterization and cytotoxicity investigations, *J. Microencapsul.* 36 (2019) 715–727. <https://doi.org/10.1080/02652048.2019.1669728>.
- [105] S.S. Darandale, P.R. Vavia, Cyclodextrin-based nanosponges of curcumin: formulation and physicochemical characterization, *J. Incl. Phenom. Macrocycl. Chem.* 75 (2013) 315–322.
- [106] M. Gharakhloo, S. Sadjadi, M. Rezaeetabar, F. Askari, A. Rahimi, Cyclodextrin-Based Nanosponges for Improving Solubility and Sustainable Release of Curcumin, *ChemistrySelect.* 5 (2020) 1734–1738. <https://doi.org/https://doi.org/10.1002/slct.201904007>.
- [107] R. Pushpalatha, S. Selvamuthukumar, D. Kilimozhi, Cross-linked, cyclodextrin-based nanosponges for curcumin delivery - Physicochemical characterization, drug release, stability and cytotoxicity, *J. Drug Deliv. Sci. Technol.* 45 (2018) 45–53. <https://doi.org/https://doi.org/10.1016/j.jddst.2018.03.004>.
- [108] H. Mashaqbeh, R. Obaidat, N. Al-Shar'i, Evaluation and characterization of

curcumin- β -cyclodextrin and cyclodextrin-based nanosponge inclusion complexation, *Polymers (Basel)*. 13 (2021) 4073.

- [109] R. Pushpalatha, S. Selvamuthukumar, D. Kilimozhi, Cyclodextrin nanosponge based hydrogel for the transdermal co-delivery of curcumin and resveratrol: Development, optimization, in vitro and ex vivo evaluation, *J. Drug Deliv. Sci. Technol.* 52 (2019) 55–64.
<https://doi.org/https://doi.org/10.1016/j.jddst.2019.04.025>.
- [110] V. Giglio, M. Viale, V. Bertone, I. Maric, R. Vaccarone, G. Vecchio, Cyclodextrin polymers as nanocarriers for sorafenib, *Invest. New Drugs*. 36 (2018) 370–379. <https://doi.org/10.1007/s10637-017-0538-9>.
- [111] M. Argenziano, C. Gigliotti, N. Clemente, E. Boggio, B. Ferrara, F. Trotta, S. Pizzimenti, G. Barrera, R. Boldorini, F. Bessone, U. Dianzani, R. Cavalli, C. Dianzani, Improvement in the Anti-Tumor Efficacy of Doxorubicin Nanosponges in In Vitro and in Mice Bearing Breast Tumor Models, *Cancers (Basel)*. 12 (2020) 162. <https://doi.org/10.3390/cancers12010162>.
- [112] S. Allahyari, H. Valizadeh, L. Roshangar, M. Mahmoudian, F. Trotta, F. Caldera, M. Jelvehgari, P. Zakeri-Milani, Preparation and characterization of cyclodextrin nanosponges for bortezomib delivery, *Expert Opin. Drug Deliv.* 17 (2020) 1807–1816. <https://doi.org/10.1080/17425247.2020.1800637>.
- [113] C.P. Dora, F. Trotta, V. Kushwah, N. Devasari, C. Singh, S. Suresh, S. Jain, Potential of erlotinib cyclodextrin nanosponge complex to enhance solubility, dissolution rate, in vitro cytotoxicity and oral bioavailability, *Carbohydr. Polym.* 137 (2016) 339–349.
<https://doi.org/https://doi.org/10.1016/j.carbpol.2015.10.080>.
- [114] P.K. Shende, F. Trotta, R.S. Gaud, K. Deshmukh, R. Cavalli, M. Biasizzo, Influence of different techniques on formulation and comparative characterization of inclusion complexes of ASA with β -cyclodextrin and inclusion complexes of ASA with PMDA cross-linked β -cyclodextrin nanosponges, *J. Incl. Phenom. Macrocycl. Chem.* 74 (2012) 447–454.
<https://doi.org/10.1007/s10847-012-0140-x>.
- [115] P.K. Shende, R.S. Gaud, R. Bakal, D. Patil, Effect of inclusion complexation of

meloxicam with β -cyclodextrin- and β -cyclodextrin-based nanosponges on solubility, in vitro release and stability studies, *Colloids Surfaces B Biointerfaces*. 136 (2015) 105–110.

<https://doi.org/https://doi.org/10.1016/j.colsurfb.2015.09.002>.

- [116] D. Lembo, S. Swaminathan, M. Donalisio, A. Civra, L. Pastero, D. Aquilano, P. Vavia, F. Trotta, R. Cavalli, Encapsulation of Acyclovir in new carboxylated cyclodextrin-based nanosponges improves the agent's antiviral efficacy, *Int. J. Pharm.* 443 (2013) 262–272.
<https://doi.org/https://doi.org/10.1016/j.ijpharm.2012.12.031>.
- [117] M.R.P. Rao, J. Chaudhari, F. Trotta, F. Caldera, Investigation of Cyclodextrin-Based Nanosponges for Solubility and Bioavailability Enhancement of Rilpivirine, *AAPS PharmSciTech*. 19 (2018) 2358–2369.
<https://doi.org/10.1208/s12249-018-1064-6>.
- [118] M.R.P. Rao, C. Shirsath, Enhancement of Bioavailability of Non-nucleoside Reverse Transcriptase Inhibitor Using Nanosponges, *AAPS PharmSciTech*. 18 (2017) 1728–1738. <https://doi.org/10.1208/s12249-016-0636-6>.
- [119] S. Swaminathan, P.R. Vavia, F. Trotta, S. Torne, Formulation of betacyclodextrin based nanosponges of itraconazole, *J. Incl. Phenom. Macrocycl. Chem.* 57 (2007) 89–94. <https://doi.org/10.1007/s10847-006-9216-9>.
- [120] R.A.M. Osmani, P.K. Kulkarni, S. Shanmuganathan, U. Hani, A. Srivastava, P. M, C.G. Shinde, R.R. Bhosale, A 32 full factorial design for development and characterization of a nanosponge-based intravaginal in situ gelling system for vulvovaginal candidiasis, *RSC Adv.* 6 (2016) 18737–18750.
<https://doi.org/10.1039/C5RA26218F>.
- [121] C. Bastiancich, S. Scutera, D. Alotto, I. Cambieri, M. Fumagalli, S. Casarin, S. Rossi, F. Trotta, M. Stella, R. Cavalli, T. Musso, C. Castagnoli, Cyclodextrin-Based Nanosponges as a Nanotechnology Strategy for Imiquimod Delivery in Pathological Scarring Prevention and Treatment, *J. Nanopharmaceutics Drug Deliv.* 2 (2014). <https://doi.org/10.1166/jnd.2014.1071>.
- [122] M. Argenziano, A. Haimhoffer, C. Bastiancich, L. Jicsinszky, F. Caldera, F. Trotta, S. Scutera, D. Alotto, M. Fumagalli, T. Musso, C. Castagnoli, R. Cavalli,

In Vitro Enhanced Skin Permeation and Retention of Imiquimod Loaded in β -Cyclodextrin Nanosponge Hydrogel, *Pharmaceutics*. 11 (2019).

<https://doi.org/10.3390/pharmaceutics11030138>.

- [123] A. Singireddy, S. Subramanian, Cyclodextrin nanosponges to enhance the dissolution profile of quercetin by inclusion complex formation, *Part. Sci. Technol.* 34 (2016) 341–346. <https://doi.org/10.1080/02726351.2015.1081658>.
- [124] S. Anandam, S. Selvamuthukumar, Fabrication of cyclodextrin nanosponges for quercetin delivery: physicochemical characterization, photostability, and antioxidant effects, *J. Mater. Sci.* 49 (2014) 8140–8153. <https://doi.org/10.1007/s10853-014-8523-6>.
- [125] A.R. Aboushanab, R.M. El-Moslemany, A.H. El-Kamel, R.A. Mehanna, B.A. Bakr, A.A. Ashour, Targeted Fisetin-Encapsulated β -Cyclodextrin Nanosponges for Breast Cancer, *Pharmaceutics*. 15 (2023). <https://doi.org/10.3390/pharmaceutics15051480>.
- [126] M. Brill, S. Fredrich, N.A. Kurniawan, Stimuli-responsive materials: A smart way to study dynamic cell responses, *Smart Mater. Med.* 3 (2022) 257–273. <https://doi.org/https://doi.org/10.1016/j.smaim.2022.01.010>.
- [127] A.-G. Niculescu, A.M. Grumezescu, Novel Tumor-Targeting Nanoparticles for Cancer Treatment—A Review, *Int. J. Mol. Sci.* 23 (2022). <https://doi.org/10.3390/ijms23095253>.
- [128] E. Gholibegloo, T. Mortezaazadeh, F. Salehian, H. Forootanfar, L. Firoozpour, A. Foroumadi, A. Ramazani, M. Khoobi, Folic acid decorated magnetic nanosponge: An efficient nanosystem for targeted curcumin delivery and magnetic resonance imaging, *J. Colloid Interface Sci.* 556 (2019) 128–139. <https://doi.org/https://doi.org/10.1016/j.jcis.2019.08.046>.
- [129] P. Singh, X. Ren, T. Guo, L. Wu, S. Shakya, Y. He, C. Wang, A. Maharjan, V. Singh, J. Zhang, Biofunctionalization of β -cyclodextrin nanosponges using cholesterol, *Carbohydr. Polym.* 190 (2018) 23–30. <https://doi.org/https://doi.org/10.1016/j.carbpol.2018.02.044>.
- [130] W.-Y. Su, Y.-C. Chen, F.-H. Lin, Injectable oxidized hyaluronic acid/adipic acid dihydrazide hydrogel for nucleus pulposus regeneration, *Acta Biomater.* 6 (2010)

3044–3055. <https://doi.org/https://doi.org/10.1016/j.actbio.2010.02.037>.

- [131] F. Afinjuomo, P. Fouladian, A. Parikh, T.G. Barclay, Y. Song, S. Garg, Preparation and Characterization of Oxidized Inulin Hydrogel for Controlled Drug Delivery, *Pharmaceutics*. 11 (2019). <https://doi.org/10.3390/pharmaceutics11070356>.
- [132] M.-Y. Bai, Q. Zhou, J. Zhang, T. Li, J. Cheng, Q. Liu, W.-R. Xu, Y.-C. Zhang, Antioxidant and antibacterial properties of essential oils-loaded β -cyclodextrin-epichlorohydrin oligomer and chitosan composite films, *Colloids Surfaces B Biointerfaces*. 215 (2022) 112504. <https://doi.org/https://doi.org/10.1016/j.colsurfb.2022.112504>.
- [133] W. Li, H. Liu, L. Li, K. Liu, J. Liu, T. Tang, W. Jiang, Green synthesis of citric acid-crosslinked β -cyclodextrin for highly efficient removal of uranium(VI) from aqueous solution, *J. Radioanal. Nucl. Chem.* 322 (2019) 2033–2042. <https://doi.org/10.1007/s10967-019-06901-2>.
- [134] H. Hao, Q. Ma, C. Huang, F. He, P. Yao, Preparation, characterization, and in vivo evaluation of doxorubicin loaded BSA nanoparticles with folic acid modified dextran surface, *Int. J. Pharm.* 444 (2013) 77–84. <https://doi.org/https://doi.org/10.1016/j.ijpharm.2013.01.041>.
- [135] Y. Yamada, Dimerization of Doxorubicin Causes Its Precipitation, *ACS Omega*. 5 (2020) 33235–33241. <https://doi.org/10.1021/acsomega.0c04925>.
- [136] M. Alibolandi, K. Abnous, F. Sadeghi, H. Hosseinkhani, M. Ramezani, F. Hadizadeh, Folate receptor-targeted multimodal polymersomes for delivery of quantum dots and doxorubicin to breast adenocarcinoma: In vitro and in vivo evaluation, *Int. J. Pharm.* 500 (2016) 162–178. <https://doi.org/https://doi.org/10.1016/j.ijpharm.2016.01.040>.
- [137] F. Ghasemzadeh, M. Mohammadi, G.D. Najafpour, A.A. Moghadamnia, Ursolic acid loaded β -cyclodextrin/folic acid/Fe₃O₄ nanocomplex for drug delivery to tumor cells, *J. Drug Deliv. Sci. Technol.* 72 (2022) 103412. <https://doi.org/https://doi.org/10.1016/j.jddst.2022.103412>.
- [138] S. Ramazi, M. Salimian, A. Allahverdi, S. Kianamiri, P. Abdolmaleki, Synergistic cytotoxic effects of an extremely low-frequency electromagnetic field

with doxorubicin on MCF-7 cell line, *Sci. Rep.* 13 (2023) 8844.

<https://doi.org/10.1038/s41598-023-35767-4>.

- [139] S. Biju, J. Gallo, M. Bañobre-López, B.B. Manshian, S.J. Soenen, U. Himmelreich, L. Vander Elst, T.N. Parac-Vogt, A Magnetic Chameleon: Biocompatible Lanthanide Fluoride Nanoparticles with Magnetic Field Dependent Tunable Contrast Properties as a Versatile Contrast Agent for Low to Ultrahigh Field MRI and Optical Imaging in Biological Window, *Chem. – A Eur. J.* 24 (2018) 7388–7397. <https://doi.org/https://doi.org/10.1002/chem.201800283>.
- [140] R. Solanki, A.K. Srivastav, S. Patel, S.K. Singh, B. Jodha, U. Kumar, S. Patel, Folate conjugated albumin as a targeted nanocarrier for the delivery of fisetin: in silico and in vitro biological studies, *RSC Adv.* 14 (2024) 7338–7349. <https://doi.org/10.1039/D3RA08434E>.
- [141] X. Peng, P. Liu, B. Pang, Y. Yao, J. Wang, K. Zhang, Facile fabrication of pH-responsive nanoparticles from cellulose derivatives via Schiff base formation for controlled release, *Carbohydr. Polym.* 216 (2019) 113–118. <https://doi.org/https://doi.org/10.1016/j.carbpol.2019.04.029>.
- [142] W. Fatima, S.R. Batool, F. Mushtaq, M. Aslam, Z.A. Raza, M.A. Nazeer, Controlled release of doxorubicin from gelatin-based nanoparticles: theoretical and experimental approach, *Mater. Adv.* 5 (2024) 2347–2358. <https://doi.org/10.1039/D3MA00825H>.
- [143] J. Mosafer, K. Abnous, M. Tafaghodi, A. Mokhtarzadeh, M. Ramezani, In vitro and in vivo evaluation of anti-nucleolin-targeted magnetic PLGA nanoparticles loaded with doxorubicin as a theranostic agent for enhanced targeted cancer imaging and therapy, *Eur. J. Pharm. Biopharm.* 113 (2017) 60–74. <https://doi.org/https://doi.org/10.1016/j.ejpb.2016.12.009>.
- [144] S. Saharkhiz, A. Zarepour, N. Nasri, M. Cordani, A. Zarrabi, A comparison study between doxorubicin and curcumin co-administration and co-loading in a smart niosomal formulation for MCF-7 breast cancer therapy, *Eur. J. Pharm. Sci.* 191 (2023) 106600. <https://doi.org/https://doi.org/10.1016/j.ejps.2023.106600>.
- [145] S. Saharkhiz, A. Zarepour, A. Zarrabi, Empowering Cancer Therapy: Comparing PEGylated and Non-PEGylated Niosomes Loaded with Curcumin and

- Doxorubicin on MCF-7 Cell Line, *Bioengineering*. 10 (2023).
<https://doi.org/10.3390/bioengineering10101159>.
- [146] M.S. Oliveira, B. Aryasomayajula, B. Pattni, S. V Mussi, L.A.M. Ferreira, V.P. Torchilin, Solid lipid nanoparticles co-loaded with doxorubicin and α -tocopherol succinate are effective against drug-resistant cancer cells in monolayer and 3-D spheroid cancer cell models, *Int. J. Pharm.* 512 (2016) 292–300.
<https://doi.org/https://doi.org/10.1016/j.ijpharm.2016.08.049>.
- [147] G. Wang, Y. Gong, F.J. Burczynski, B.B. Hasinoff, Cell lysis with dimethyl sulphoxide produces stable homogeneous solutions in the dichlorofluorescein oxidative stress assay, *Free Radic. Res.* 42 (2008) 435–441.
<https://doi.org/10.1080/10715760802074462>.
- [148] T. Lei, S. Srinivasan, Y. Tang, R. Manchanda, A. Nagesetti, A. Fernandez-Fernandez, A.J. McGoron, Comparing cellular uptake and cytotoxicity of targeted drug carriers in cancer cell lines with different drug resistance mechanisms, *Nanomedicine Nanotechnology, Biol. Med.* 7 (2011) 324–332.
<https://doi.org/https://doi.org/10.1016/j.nano.2010.11.004>.
- [149] M. Nasr, F. Hashem, M. Teiama, N. Tantawy, R. Abdelmoniem, Folic acid grafted mixed polymeric micelles as a targeted delivery strategy for tamoxifen citrate in treatment of breast cancer, *Drug Deliv. Transl. Res.* 14 (2024) 945–958.
<https://doi.org/10.1007/s13346-023-01443-3>.
- [150] R.L. Abarca, F.J. Rodríguez, A. Guarda, M.J. Galotto, J.E. Bruna, Characterization of beta-cyclodextrin inclusion complexes containing an essential oil component, *Food Chem.* 196 (2016) 968–975.
<https://doi.org/https://doi.org/10.1016/j.foodchem.2015.10.023>.
- [151] C. Yuan, B. Liu, H. Liu, Characterization of hydroxypropyl- β -cyclodextrins with different substitution patterns via FTIR, GC–MS, and TG–DTA, *Carbohydr. Polym.* 118 (2015) 36–40.
<https://doi.org/https://doi.org/10.1016/j.carbpol.2014.10.070>.
- [152] R. Xu, X. Lin, J. Xu, C. Lei, Controlling the water absorption and improving the high C-rate stability: a coated Li-ion battery separator using β -cyclodextrin as binder, *Ionics (Kiel)*. 26 (2020) 3359–3365. <https://doi.org/10.1007/s11581-020->

03449-0.

- [153] W.-Y. Su, K.-H. Chen, Y.-C. Chen, Y.-H. Lee, C.-L. Tseng, F.-H. Lin, An Injectable Oxidated Hyaluronic Acid/Adipic Acid Dihydrazide Hydrogel as a Vitreous Substitute, *J. Biomater. Sci. Polym. Ed.* 22 (2011) 1777–1797. <https://doi.org/10.1163/092050610X522729>.
- [154] I. García-Santos, J. Sanmartín, A.M. García-Deibe, M. Fondo, E. Gómez, Structural and spectroscopic studies on some metal complexes of an 8-hydroxyquinoline derivative, *Inorganica Chim. Acta.* 363 (2010) 193–198. <https://doi.org/https://doi.org/10.1016/j.ica.2009.09.004>.
- [155] S. Deng, H. Liu, C. Qi, A. Yang, Z. Li, Study on preparation and inclusion behavior of inclusion complexes between β -cyclodextrin derivatives with benzophenone, *J. Incl. Phenom. Macrocycl. Chem.* 90 (2018) 321–329. <https://doi.org/10.1007/s10847-018-0787-z>.
- [156] A. Matei, C. Puscas, I. Patrascu, M. Lehene, J. Ziebro, F. Scurtu, M. Baia, D. Porumb, R. Totos, R. Silaghi-Dumitrescu, On the Stability of Glutaraldehyde in Biocide Compositions, *Int. J. Mol. Sci.* 21 (2020) 3372. <https://doi.org/10.3390/ijms21093372>.
- [157] Z. Xue, R. Fu, Z. Duan, L. Chi, C. Zhu, D. Fan, Inhibitory Effect of pH-Responsive Nanogel Encapsulating Ginsenoside CK against Lung Cancer, *Polymers (Basel)*. 13 (2021). <https://doi.org/10.3390/polym13111784>.
- [158] I. Asela, O. Donoso-González, N. Yutronic, R. Sierpe, β -Cyclodextrin-Based Nanosponges Functionalized with Drugs and Gold Nanoparticles, *Pharmaceutics*. 13 (2021). <https://doi.org/10.3390/pharmaceutics13040513>.
- [159] B. Yang, L. Yang, J. Lin, Y. Chen, Y. Liu, Binding behaviors of scutellarin with α -, β -, γ -cyclodextrins and their derivatives, *J. Incl. Phenom. Macrocycl. Chem.* 64 (2009) 149–155. <https://doi.org/10.1007/s10847-009-9547-4>.
- [160] M.L. Calabrò, S. Tommasini, P. Donato, D. Raneri, R. Stancanelli, P. Ficarra, R. Ficarra, C. Costa, S. Catania, C. Rustichelli, G. Gamberini, Effects of α - and β -cyclodextrin complexation on the physico-chemical properties and antioxidant activity of some 3-hydroxyflavones, *J. Pharm. Biomed. Anal.* 35 (2004) 365–377. <https://doi.org/https://doi.org/10.1016/j.jpba.2003.12.005>.

- [161] L. Cunha-Silva, J.J.C. Teixeira-Dias, How humidity affects the solid-state inclusion of 2-phenoxyethanol in β -cyclodextrin: a comparison with β -cyclodextrin, *New J. Chem.* 28 (2004) 200–206.
<https://doi.org/10.1039/B309491J>.
- [162] F. Afinjuomo, P. Fouladian, T.G. Barclay, Y. Song, N. Petrovsky, S. Garg, Influence of Oxidation Degree on the Physicochemical Properties of Oxidized Inulin, *Polymers (Basel)*. 12 (2020). <https://doi.org/10.3390/polym12051025>.
- [163] A. Lis-Cieplak, F. Charuk, M. Sobczak, A. Zgadzaj, A. Drobniewska, Ł. Szeleszczuk, E. Oledzka, Development and Evaluation of Matrices Composed of β -cyclodextrin and Biodegradable Polyesters in the Controlled Delivery of Pindolol, *Pharmaceutics*. 12 (2020).
<https://doi.org/10.3390/pharmaceutics12060500>.
- [164] A. Kumar, R. Rao, Formulation and modification of physicochemical parameters of p-Coumaric acid by cyclodextrin nanosponges, *J. Incl. Phenom. Macrocycl. Chem.* 102 (2022) 313–326. <https://doi.org/10.1007/s10847-021-01121-2>.
- [165] M. Bakonyi, S. Berkó, M. Budai-Szűcs, A. Kovács, E. Csányi, DSC for evaluating the encapsulation efficiency of lidocaine-loaded liposomes compared to the ultracentrifugation method, *J. Therm. Anal. Calorim.* 130 (2017) 1619–1625. <https://doi.org/10.1007/s10973-017-6394-1>.
- [166] F. Du, T. Pan, X. Ji, J. Hu, T. Ren, Study on the preparation of geranyl acetone and β -cyclodextrin inclusion complex and its application in cigarette flavoring, *Sci. Rep.* 10 (2020) 12375. <https://doi.org/10.1038/s41598-020-69323-1>.
- [167] H. Rachmawati, C. Ariani, R. Mauludin, Molecular Inclusion Complex of Curcumin– β -Cyclodextrin Nanoparticle to Enhance Curcumin Skin Permeability from Hydrophilic Matrix Gel, *AAPS PharmSciTech.* 14 (2013).
<https://doi.org/10.1208/s12249-013-0023-5>.
- [168] C.G. França, K.C. Leme, Â.C.M. Luzo, J. Hernandez-Montelongo, M.H.A. Santana, Oxidized hyaluronic acid/adipic acid dihydrazide hydrogel as cell microcarriers for tissue regeneration applications, 22 (2022) 949–958.
<https://doi.org/doi:10.1515/epoly-2022-0086>.
- [169] S.-H. Lee, S.-R. Shin, D.-S. Lee, Self-healing of cross-linked PU via dual-

- dynamic covalent bonds of a Schiff base from cystine and vanillin, *Mater. Des.* 172 (2019) 107774. <https://doi.org/10.1016/j.matdes.2019.107774>.
- [170] Y.-C. Chen, W.-Y. Su, S.-H. Yang, A. Gefen, F.-H. Lin, In situ forming hydrogels composed of oxidized high molecular weight hyaluronic acid and gelatin for nucleus pulposus regeneration, *Acta Biomater.* 9 (2013) 5181–5193. <https://doi.org/10.1016/j.actbio.2012.09.039>.
- [171] M. Shringirishi, A. Mahor, R. Gupta, S.K. Prajapati, K. Bansal, P. Kesharwani, Fabrication and characterization of nifedipine loaded β -cyclodextrin nanosponges: An in vitro and in vivo evaluation, *J. Drug Deliv. Sci. Technol.* 41 (2017) 344–350. <https://doi.org/10.1016/j.jddst.2017.08.005>.
- [172] C. Pan, J. Qian, C. Zhao, H. Yang, X. Zhao, H. Guo, Study on the relationship between crosslinking degree and properties of TPP crosslinked chitosan nanoparticles, *Carbohydr. Polym.* 241 (2020) 116349. <https://doi.org/10.1016/j.carbpol.2020.116349>.
- [173] D.T. Pham, N. Saelim, R. Cornu, A. Béduneau, W. Tiyaboonchai, Crosslinked Fibroin Nanoparticles: Investigations on Biostability, Cytotoxicity, and Cellular Internalization, *Pharmaceuticals.* 13 (2020). <https://doi.org/10.3390/ph13050086>.
- [174] X. Xing, Y. Han, Q. Jiang, Y. Sun, X. Wang, G. Qu, G. Sun, Y. Li, Immobilization of laccases onto cellulose nanocrystals derived from waste newspaper: relationship between immobilized laccase activity and dialdehyde content, *Cellulose.* 28 (2021) 4793–4805. <https://doi.org/10.1007/s10570-021-03867-x>.
- [175] H. Yong, R. Bai, F. Bi, J. Liu, Y. Qin, J. Liu, Synthesis, characterization, antioxidant and antimicrobial activities of starch aldehyde-quercetin conjugate, *Int. J. Biol. Macromol.* 156 (2020) 462–470. <https://doi.org/10.1016/j.ijbiomac.2020.04.035>.
- [176] R.P. Das, V. V Gandhi, B.G. Singh, A. Kunwar, N.N. Kumar, K.I. Priyadarsini, Preparation of albumin nanoparticles: Optimum size for cellular uptake of entrapped drug (Curcumin), *Colloids Surfaces A Physicochem. Eng. Asp.* 567 (2019) 86–95. <https://doi.org/10.1016/j.colsurfa.2019.01.043>.
- [177] X. Liu, W. Li, G. Xuan, Preparation and Characterization of β -Cyclodextrin

Nanosponges and Study on Enhancing the Solubility of Insoluble Nicosulfuron, IOP Conf. Ser. Mater. Sci. Eng. 774 (2020) 12108. <https://doi.org/10.1088/1757-899X/774/1/012108>.

- [178] V. Suvarna, V. Singh, D. Sharma, M. Murahari, Experimental and computational insight of the supramolecular complexes of Irbesartan with β -cyclodextrin based nanosponges, J. Drug Deliv. Sci. Technol. 63 (2021) 102494. <https://doi.org/https://doi.org/10.1016/j.jddst.2021.102494>.
- [179] M.I. Rodriguez López, J. Pellicer, T. Gómez-Morte, D. Auñon Calles, V. Gómez-López, M. Yáñez-Gascón, J. Cerón-Carrasco, C. grégorio, E. Núñez-Delicado, J. Gabaldon, Removal of an Azo Dye from Wastewater through the Use of Two Technologies: Magnetic Cyclodextrin Polymers and Pulsed Light, Int. J. Mol. Sci. 23 (2022) 8406. <https://doi.org/10.3390/ijms23158406>.
- [180] V. Singh, J. Xu, L. Wu, B. Liu, T. Guo, Z. Guo, P. York, R. Gref, J. Zhang, Ordered and disordered cyclodextrin nanosponges with diverse physicochemical properties, RSC Adv. 7 (2017) 23759–23764. <https://doi.org/10.1039/C7RA00584A>.
- [181] S. Peimanfard, A. Zarrabi, F. Trotta, A. Matencio, C. Cecone, F. Caldera, Developing Novel Hydroxypropyl- β -Cyclodextrin-Based Nanosponges as Carriers for Anticancer Hydrophobic Agents: Overcoming Limitations of Host–Guest Complexes in a Comparative Evaluation, Pharmaceutics. 14 (2022). <https://doi.org/10.3390/pharmaceutics14051059>.
- [182] C. Bofill-Bonet, M. Gil-Vives, M. Artigues, M. Hernández, S. Borrós, C. Fornaguera, Fine-tuning formulation and biological interaction of doxorubicin-loaded polymeric nanoparticles via electrolyte concentration modulation, J. Mol. Liq. 390 (2023) 122986. <https://doi.org/https://doi.org/10.1016/j.molliq.2023.122986>.
- [183] D. Kim, S.S. Lee, W.Y. Yoo, H. Moon, A. Cho, S.Y. Park, Y.-S. Kim, H.R. Kim, H.J. Lee, Combination Therapy with Doxorubicin-Loaded Reduced Albumin Nanoparticles and Focused Ultrasound in Mouse Breast Cancer Xenografts, Pharmaceutics. 13 (2020). <https://doi.org/10.3390/ph13090235>.
- [184] S.N. Dada, G.K. Babanyinah, M.T. Tetteh, V.E. Palau, Z.F. Walls, K. Krishnan,

- Z. Croft, A.U. Khan, G. Liu, T.E. Wiese, E. Glotser, H. Mei, Covalent and Noncovalent Loading of Doxorubicin by Folic Acid-Carbon Dot Nanoparticles for Cancer Theranostics, *ACS Omega*. 7 (2022) 23322–23331.
<https://doi.org/10.1021/acsomega.2c01482>.
- [185] M.M. Can, S. Shawuti, F.D. Kalindemirtas, G. Erdemir, D.S. Kuruca, S. Kaneko, Z. Aktas, O. Oncul, Anticancer drug doxorubicin (DOX) loading performance of functionalized polyaniline (PANI) surface with active carbon, *J. Mater. Sci.* 58 (2023) 4726–4738. <https://doi.org/10.1007/s10853-023-08291-z>.
- [186] S. Kayal, R. V Ramanujan, Doxorubicin loaded PVA coated iron oxide nanoparticles for targeted drug delivery, *Mater. Sci. Eng. C*. 30 (2010) 484–490.
<https://doi.org/https://doi.org/10.1016/j.msec.2010.01.006>.
- [187] J. Xu, M. Song, Z. Fang, L. Zheng, X. Huang, K. Liu, Applications and challenges of ultra-small particle size nanoparticles in tumor therapy, *J. Control. Release*. 353 (2023) 699–712.
<https://doi.org/https://doi.org/10.1016/j.jconrel.2022.12.028>.
- [188] Y. Mi, J. Zhang, W. Tan, Q. Miao, Q. Li, Z. Guo, Preparation of Doxorubicin-Loaded Carboxymethyl- β -Cyclodextrin/Chitosan Nanoparticles with Antioxidant, Antitumor Activities and pH-Sensitive Release, *Mar. Drugs*. 20 (2022). <https://doi.org/10.3390/md20050278>.
- [189] T.N. Nguyen, T.T. Nguyen, T.H.L. Nghiem, D.T. Nguyen, T.T.H. Tran, D. Vu, T.B.N. Nguyen, T.M.H. Nguyen, V.T. Nguyen, M.H. Nguyen, Optical properties of doxorubicin hydrochloride load and release on silica nanoparticle platform, *Molecules*. 26 (2021) 3968.
- [190] H.Y. Fan, G. Raval, A. Shalviri, S. May, X.Y. Wu, H. Heerklotz, Coupled equilibria of a self-associating drug loaded into polymeric nanoparticles, *Methods*. 76 (2015) 162–170.
<https://doi.org/https://doi.org/10.1016/j.ymeth.2014.12.015>.
- [191] T.N.T. Nguyen, N.T.T. Le, N.H. Nguyen, B.T.K. Ly, T.D. Nguyen, D.H. Nguyen, Aminated hollow mesoporous silica nanoparticles as an enhanced loading and sustained releasing carrier for doxorubicin delivery, *Microporous Mesoporous Mater.* 309 (2020) 110543.

<https://doi.org/https://doi.org/10.1016/j.micromeso.2020.110543>.

- [192] V.R. Khabibullin, M.R. Chetyrkina, S.I. Obydenny, S. V Maksimov, G. V Stepanov, S.N. Shtykov, Study on Doxorubicin Loading on Differently Functionalized Iron Oxide Nanoparticles: Implications for Controlled Drug-Delivery Application, *Int. J. Mol. Sci.* 24 (2023).
<https://doi.org/10.3390/ijms24054480>.
- [193] S. V Lale, A. Kumar, F. Naz, A.C. Bharti, V. Koul, Multifunctional ATRP based pH responsive polymeric nanoparticles for improved doxorubicin chemotherapy in breast cancer by proton sponge effect/endo-lysosomal escape, *Polym. Chem.* 6 (2015) 2115–2132. <https://doi.org/10.1039/C4PY01698J>.
- [194] V.O. Fasiku, B.A. Aderibigbe, E.R. Sadiku, Y. Lemmer, S.J. Owonubi, S.S. Ray, E. Mukwevho, Polyethylene glycol–gum acacia-based multidrug delivery system for controlled delivery of anticancer drugs, *Polym. Bull.* 76 (2019) 5011–5037.
<https://doi.org/10.1007/s00289-018-2642-1>.
- [195] M.C. García, N. Naitlho, J.M. Calderón-Montaña, E. Drago, M. Rueda, M. Longhi, A.M. Rabasco, M. López-Lázaro, F. Prieto-Dapena, M.L. González-Rodríguez, Cholesterol Levels Affect the Performance of AuNPs-Decorated Thermo-Sensitive Liposomes as Nanocarriers for Controlled Doxorubicin Delivery, *Pharmaceutics.* 13 (2021).
<https://doi.org/10.3390/pharmaceutics13070973>.
- [196] R. Pushpalatha, S. Selvamuthukumar, D. Kilimozhi, Carbonyl and carboxylate crosslinked cyclodextrin as a nanocarrier for resveratrol: in silico, in vitro and in vivo evaluation, *J. Incl. Phenom. Macrocycl. Chem.* 92 (2018) 261–272.
<https://doi.org/10.1007/s10847-018-0843-8>.
- [197] N.M. AlSawafth, N.S. Awad, W.G. Pitt, G.A. Hussein, pH-Responsive Nanocarriers in Cancer Therapy, *Polymers (Basel).* 14 (2022).
<https://doi.org/10.3390/polym14050936>.
- [198] F. Jia, Y. Wang, H. Wang, Q. Jin, T. Cai, Y. Chen, J. Ji, Light cross-linkable and pH de-cross-linkable drug nanocarriers for intracellular drug delivery, *Polym. Chem.* 6 (2015) 2069–2075. <https://doi.org/10.1039/C4PY01420K>.
- [199] O. Jordan, A. Denys, T. De Baere, N. Boulens, E. Doelker, Comparative Study of

- Chemoembolization Loadable Beads: In vitro Drug Release and Physical Properties of DC Bead and Hepasphere Loaded with Doxorubicin and Irinotecan, *J. Vasc. Interv. Radiol.* 21 (2010) 1084–1090.
<https://doi.org/https://doi.org/10.1016/j.jvir.2010.02.042>.
- [200] F. Espinola-Portilla, F. d’Orlyé, L. Trapiella-Alfonso, S. Gutiérrez-Granados, G. Ramírez-García, A. Varenne, Rational Understanding of Loading and Release of Doxorubicin by UV-Light- and pH-Responsive Poly(NIPAM-co-SPMA) Micelle-like Aggregates, *Mol. Pharm.* 20 (2023) 1490–1499.
<https://doi.org/10.1021/acs.molpharmaceut.2c00690>.
- [201] Z. Liu, R. Cheung, X.Y. Wu, J.R. Ballinger, R. Bendayan, A.M. Rauth, A study of doxorubicin loading onto and release from sulfopropyl dextran ion-exchange microspheres, *J. Control. Release.* 77 (2001) 213–224.
[https://doi.org/https://doi.org/10.1016/S0168-3659\(01\)00473-4](https://doi.org/https://doi.org/10.1016/S0168-3659(01)00473-4).
- [202] B.K. Heragh, H. Taherinezhad, G.R. Mahdavinia, S. Javanshir, P. Labib, S. Ghasemsolb, pH-responsive co-delivery of doxorubicin and saffron via cross-linked chitosan/laponite RD nanoparticles for enhanced-chemotherapy, *Mater. Today Commun.* 34 (2023) 104956.
<https://doi.org/https://doi.org/10.1016/j.mtcomm.2022.104956>.
- [203] J. Nogueira, S.F. Soares, C.O. Amorim, J.S. Amaral, C. Silva, F. Martel, T. Trindade, A.L. Daniel-da-Silva, Magnetic Driven Nanocarriers for pH-Responsive Doxorubicin Release in Cancer Therapy, *Molecules.* 25 (2020).
<https://doi.org/10.3390/molecules25020333>.
- [204] F.N. Parin, S. Ullah, K. Yildirim, M. Hashmi, I.-S. Kim, Fabrication and Characterization of Electrospun Folic Acid/Hybrid Fibers: In Vitro Controlled Release Study and Cytocompatibility Assays, *Polymers (Basel).* 13 (2021).
<https://doi.org/10.3390/polym13203594>.
- [205] J. Zhang, S. Rana, R.S. Srivastava, R.D.K. Misra, On the chemical synthesis and drug delivery response of folate receptor-activated, polyethylene glycol-functionalized magnetite nanoparticles, *Acta Biomater.* 4 (2008) 40–48.
<https://doi.org/https://doi.org/10.1016/j.actbio.2007.06.006>.
- [206] N. Sun, R. Lei, J. Xu, S.C. Kundu, Y. Cai, J. Yao, Q. Ni, Fabricated porous silk

- fibroin particles for pH-responsive drug delivery and targeting of tumor cells, *J. Mater. Sci.* 54 (2019) 3319–3330.
- [207] S.-J. Yang, F.-H. Lin, K.-C. Tsai, M.-F. Wei, H.-M. Tsai, J.-M. Wong, M.-J. Shieh, Folic Acid-Conjugated Chitosan Nanoparticles Enhanced Protoporphyrin IX Accumulation in Colorectal Cancer Cells, *Bioconjug. Chem.* 21 (2010) 679–689. <https://doi.org/10.1021/bc9004798>.
- [208] S. Jain, V. V Rathi, A.K. Jain, M. Das, C. Godugu, Folate-decorated PLGA nanoparticles as a rationally designed vehicle for the oral delivery of insulin, *Nanomedicine.* 7 (2012) 1311–1337.
- [209] N.O. Okamoto-Schalch, S.G.B. Pinho, T.T. de Barros-Alexandrino, G.C. Dacanal, O.B.G. Assis, M. Martelli-Tosi, Production and characterization of chitosan-TPP/cellulose nanocrystal system for encapsulation: a case study using folic acid as active compound, *Cellulose.* 27 (2020) 5855–5869. <https://doi.org/10.1007/s10570-020-03173-y>.
- [210] S. Milewska, G. Siemiaszko, A.Z. Wilczewska, I. Misztalewska-Turkowicz, K.H. Markiewicz, D. Szymczuk, D. Sawicka, H. Car, R. Lazny, K. Niemirowicz-Laskowska, Folic-acid-conjugated thermoresponsive polymeric particles for targeted delivery of 5-fluorouracil to CRC cells, *Int. J. Mol. Sci.* 24 (2023) 1364.
- [211] A.S. Novikova, T.S. Ponomaryova, I.Y. Goryacheva, Fluorescent AgInS/ZnS quantum dots microplate and lateral flow immunoassays for folic acid determination in juice samples, *Microchim. Acta.* 187 (2020) 427. <https://doi.org/10.1007/s00604-020-04398-1>.
- [212] M. Ceborska, M. Zimnicka, M. Wszelaka-Rylik, A. Troć, Characterization of folic acid/native cyclodextrins host–guest complexes in solution, *J. Mol. Struct.* 1109 (2016) 114–118. <https://doi.org/https://doi.org/10.1016/j.molstruc.2015.12.082>.
- [213] S.-J. Yang, F.-H. Lin, H.-M. Tsai, C.-F. Lin, H.-C. Chin, J.-M. Wong, M.-J. Shieh, Alginate-folic acid-modified chitosan nanoparticles for photodynamic detection of intestinal neoplasms, *Biomaterials.* 32 (2011) 2174–2182. <https://doi.org/https://doi.org/10.1016/j.biomaterials.2010.11.039>.
- [214] V.T. Nguyen, T.H. Nguyen, L.H. Dang, H. Vu-Quang, N.Q. Tran, Folate-

Conjugated Chitosan-Pluronic P123 Nanogels: Synthesis and Characterizations towards Dual Drug Delivery, *J. Nanomater.* 2019 (2019) 1067821.
<https://doi.org/10.1155/2019/1067821>.

- [215] S. Ullah, A.K. Azad, A. Nawaz, K.U. Shah, M. Iqbal, G.M. Albadrani, F.A. Al-Joufi, A.A. Sayed, M.M. Abdel-Daim, 5-Fluorouracil-Loaded Folic-Acid-Fabricated Chitosan Nanoparticles for Site-Targeted Drug Delivery Cargo, *Polymers (Basel)*. 14 (2022). <https://doi.org/10.3390/polym14102010>.
- [216] D. Luong, P. Kesharwani, H.O. Alsaab, S. Sau, S. Padhye, F.H. Sarkar, A.K. Iyer, Folic acid conjugated polymeric micelles loaded with a curcumin difluorinated analog for targeting cervical and ovarian cancers, *Colloids Surfaces B Biointerfaces*. 157 (2017) 490–502.
- [217] İ. İnce, Y. Yıldırım, G. Güler, E.İ. Medine, G. Ballica, B.C. Kuşdemir, E. Göker, Synthesis and characterization of folic acid-chitosan nanoparticles loaded with thymoquinone to target ovarian cancer cells, *J. Radioanal. Nucl. Chem.* 324 (2020) 71–85.
- [218] F. Jiang, H. Ye, H. Li, K. Sun, J. Yin, H. Zhu, Metal complexes of folic acid for lithium ion storage, *Chem. Commun.* 54 (2018) 4971–4974.
<https://doi.org/10.1039/C8CC01234B>.
- [219] U. Ruman, K. Buskaran, G. Pastorin, M.J. Masarudin, S. Fakurazi, M.Z. Hussein, Synthesis and Characterization of Chitosan-Based Nanodelivery Systems to Enhance the Anticancer Effect of Sorafenib Drug in Hepatocellular Carcinoma and Colorectal Adenocarcinoma Cells, *Nanomaterials*. 11 (2021).
<https://doi.org/10.3390/nano11020497>.
- [220] Q.L. Jiang, S.W. Zheng, R.Y. Hong, S.M. Deng, L. Guo, R.L. Hu, B. Gao, M. Huang, L.F. Cheng, G.H. Liu, Y.Q. Wang, Folic acid-conjugated Fe₃O₄ magnetic nanoparticles for hyperthermia and MRI in vitro and in vivo, *Appl. Surf. Sci.* 307 (2014) 224–233.
<https://doi.org/https://doi.org/10.1016/j.apsusc.2014.04.018>.
- [221] E. Fathima, I. Nallamuthu, T. Anand, M. Naika, F. Khanum, Enhanced cellular uptake, transport and oral bioavailability of optimized folic acid-loaded chitosan nanoparticles, *Int. J. Biol. Macromol.* 208 (2022) 596–610.

<https://doi.org/https://doi.org/10.1016/j.ijbiomac.2022.03.042>.

- [222] O.M. El-Borady, A.F. El-Sayed, Synthesis, morphological, spectral and thermal studies for folic acid conjugated ZnO nanoparticles: potency for multi-functional bio-nanocomposite as antimicrobial, antioxidant and photocatalytic agent, *J. Mater. Res. Technol.* 9 (2020) 1905–1917.
<https://doi.org/https://doi.org/10.1016/j.jmrt.2019.12.022>.
- [223] R. Biabanikhankahdani, S. Bayat, K.L. Ho, N.B.M. Alitheen, W.S. Tan, A Simple Add-and-Display Method for Immobilisation of Cancer Drug on His-tagged Virus-like Nanoparticles for Controlled Drug Delivery, *Sci. Rep.* 7 (2017) 5303. <https://doi.org/10.1038/s41598-017-05525-4>.
- [224] G. Siemiaszko, K. Niemirowicz - Laskowska, K. Markiewicz, I. Misztalewska-Turkowicz, E. Dudź, S. Milewska, P. Misiak, I. Kurowska, A. Sadowska, H. Car, A. Wilczewska, Synergistic effect of folate-conjugated polymers and 5-fluorouracil in the treatment of colon cancer, *Cancer Nanotechnol.* 12 (2021).
<https://doi.org/10.1186/s12645-021-00104-9>.
- [225] P. Chanphai, H.A. Tajmir-Riahi, Characterization of folic acid-PAMAM conjugates: drug loading efficacy and dendrimer morphology, *J. Biomol. Struct. Dyn.* 36 (2018) 1918–1924. <https://doi.org/10.1080/07391102.2017.1341339>.
- [226] M. Khalil, E.A. Haq, A. Dwiranti, E.S. Prasedya, Y. Kitamoto, Bifunctional folic-conjugated aspartic-modified Fe₃O₄ nanocarriers for efficient targeted anticancer drug delivery, *RSC Adv.* 12 (2022) 4961–4971.
<https://doi.org/10.1039/D1RA08776B>.
- [227] S. Rana, N.G. Shetake, K.C. Barick, B.N. Pandey, H.G. Salunke, P.A. Hassan, Folic acid conjugated Fe₃O₄ magnetic nanoparticles for targeted delivery of doxorubicin, *Dalt. Trans.* 45 (2016) 17401–17408.
<https://doi.org/10.1039/C6DT03323G>.
- [228] R. Bansal, R. Singh, K. Kaur, Quantitative analysis of doxorubicin hydrochloride and arterolane maleate by mid IR spectroscopy using transmission and reflectance modes, *BMC Chem.* 15 (2021). <https://doi.org/10.1186/s13065-021-00752-3>.
- [229] Y. Yu, C.-K. Chen, W.-C. Law, E. Weinheimer, S. Sengupta, P.N. Prasad, C.

- Cheng, Polylactide-graft-doxorubicin Nanoparticles with Precisely Controlled Drug Loading for pH-Triggered Drug Delivery, *Biomacromolecules*. 15 (2014) 524–532. <https://doi.org/10.1021/bm401471p>.
- [230] H. Yang, A. Sun, J. Yang, H. Cheng, X. Yang, H. Chen, D. Huanfei, M. Falahati, Development of doxorubicin-loaded chitosan–heparin nanoparticles with selective anticancer efficacy against gastric cancer cells in vitro through regulation of intrinsic apoptosis pathway, *Arab. J. Chem.* 14 (2021) 103266. <https://doi.org/https://doi.org/10.1016/j.arabjc.2021.103266>.
- [231] J. Lu, W. Zhao, Y. Huang, H. Liu, R. Marquez, R.B. Gibbs, J. Li, R. Venkataramanan, L. Xu, S. Li, S. Li, Targeted Delivery of Doxorubicin by Folic Acid-Decorated Dual Functional Nanocarrier, *Mol. Pharm.* 11 (2014) 4164–4178. <https://doi.org/10.1021/mp500389v>.
- [232] M. Kciuk, A. Gielecińska, S. Mujwar, D. Kołat, Ż. Kałuzińska-Kołat, I. Celik, R. Kontek, Doxorubicin—An Agent with Multiple Mechanisms of Anticancer Activity, *Cells*. 12 (2023). <https://doi.org/10.3390/cells12040659>.
- [233] C. Parisi, F. Moret, A. Fraix, L. Menilli, M. Failla, F. Sodano, C. Conte, F. Quaglia, E. Reddi, S. Sortino, Doxorubicin–NO Releaser Molecular Hybrid Activatable by Green Light to Overcome Resistance in Breast Cancer Cells, *ACS Omega*. 7 (2022) 7452–7459. <https://doi.org/10.1021/acsomega.1c03988>.
- [234] N. Dube, J.Y. Shu, H. Dong, J.W. Seo, E. Ingham, A. Kheirrolomoom, P.-Y. Chen, J. Forsayeth, K. Bankiewicz, K.W. Ferrara, T. Xu, Evaluation of Doxorubicin-Loaded 3-Helix Micelles as Nanocarriers, *Biomacromolecules*. 14 (2013) 3697–3705. <https://doi.org/10.1021/bm4010518>.
- [235] N. Tsakiris, M. Papavasileiou, E. Bozzato, A. Lopes, A.M. Vigneron, V. Pr at, Combinational drug-loaded lipid nanocapsules for the treatment of cancer, *Int. J. Pharm.* 569 (2019) 118588. <https://doi.org/https://doi.org/10.1016/j.ijpharm.2019.118588>.
- [236] Z. Kayani, A.-K. Bordbar, O. Firuzi, Novel folic acid-conjugated doxorubicin loaded β -lactoglobulin nanoparticles induce apoptosis in breast cancer cells, *Biomed. Pharmacother.* 107 (2018) 945–956. <https://doi.org/https://doi.org/10.1016/j.biopha.2018.08.047>.

- [237] M. Safari Sharafshadeh, F. Tafvizi, P. Khodarahmi, S. Ehtesham, Folic acid-functionalized PEGylated niosomes co-encapsulated cisplatin and doxorubicin exhibit enhanced anticancer efficacy, *Cancer Nanotechnol.* 15 (2024) 14. <https://doi.org/10.1186/s12645-024-00252-8>.
- [238] E. Lamprou, S. Mourtas, M. Mantzari, A. Marazioti, F. Gkartziou, S.G. Antimisiaris, Folic Acid—Targeted Doxorubicin Drug Delivery System for Triple-Negative Breast Cancer Treatment, *Proceedings.* 78 (2021). <https://doi.org/10.3390/IECP2020-08660>.
- [239] P.D. Harvey, J. Plé, Recent Advances in Nanoscale Metal–Organic Frameworks Towards Cancer Cell Cytotoxicity: An Overview, *J. Inorg. Organomet. Polym. Mater.* 31 (2021) 2715–2756. <https://doi.org/10.1007/s10904-021-02011-3>.
- [240] M. Norouzi, V. Yathindranath, J.A. Thliveris, B.M. Kopec, T.J. Siahaan, D.W. Miller, Doxorubicin-loaded iron oxide nanoparticles for glioblastoma therapy: a combinational approach for enhanced delivery of nanoparticles, *Sci. Rep.* 10 (2020) 11292. <https://doi.org/10.1038/s41598-020-68017-y>.
- [241] M. Asif, M. Fakhar-e-Alam, M. Hassan, H. Sardar, M. Zulqarnian, L. Li, A.A. Alothman, A.B. Alangary, S. Mohammad, Synergistic response of PEG coated manganese dioxide nanoparticles conjugated with doxorubicin for breast cancer treatment and MRI application, *Arab. J. Chem.* 17 (2024) 105958. <https://doi.org/https://doi.org/10.1016/j.arabjc.2024.105958>.
- [242] A. Zarepour, A.C. Egil, M. Cokol Cakmak, M. Esmaili Rad, Y. Cetin, S. Aydinlik, G. Ozaydin Ince, A. Zarrabi, Fabrication of a Dual-Drug-Loaded Smart Niosome-g-Chitosan Polymeric Platform for Lung Cancer Treatment, *Polymers (Basel).* 15 (2023). <https://doi.org/10.3390/polym15020298>.
- [243] C. Xu, R. Song, P. Lu, J. Chen, Y. Zhou, G. Shen, M. Jiang, W. Zhang, A pH-Responsive Charge-Reversal Drug Delivery System with Tumor-Specific Drug Release and ROS Generation for Cancer Therapy, *Int. J. Nanomedicine.* 15 (2020) 65–80. <https://doi.org/10.2147/IJN.S230237>.
- [244] M.M. Hadi, H. Nesbitt, H. Masood, F. Sciscione, S. Patel, B.S. Ramesh, M. Emberton, J.F. Callan, A. MacRobert, A.P. McHale, N. Nomikou, Investigating the performance of a novel pH and cathepsin B sensitive, stimulus-responsive

nanoparticle for optimised sonodynamic therapy in prostate cancer, *J. Control. Release.* 329 (2021) 76–86.

<https://doi.org/https://doi.org/10.1016/j.jconrel.2020.11.040>.

- [245] A. Granja, C. Nunes, C.T. Sousa, S. Reis, Folate receptor-mediated delivery of mitoxantrone-loaded solid lipid nanoparticles to breast cancer cells, *Biomed. Pharmacother.* 154 (2022) 113525.
<https://doi.org/https://doi.org/10.1016/j.biopha.2022.113525>.
- [246] A.A. Borisenkova, O.I. Bolshakova, A. V Titova, I.S. Ryabokon, M.A. Markova, Z.B. Lyutova, V.P. Sedov, E.Y. Varfolomeeva, V. V Bakhmetyev, A. V Arutyunyan, V.S. Burdakov, S. V Sarantseva, Fullerene C60 Conjugate with Folic Acid and Polyvinylpyrrolidone for Targeted Delivery to Tumor Cells, *Int. J. Mol. Sci.* 25 (2024). <https://doi.org/10.3390/ijms25105350>.
- [247] N. Rostami, M.M. Gomari, M. Abdouss, A. Moeinzadeh, E. Choupani, R. Davarnejad, R. Heidari, S.A. Bencherif, Synthesis and Characterization of Folic Acid-Functionalized DPLA-co-PEG Nanomicelles for the Targeted Delivery of Letrozole, *ACS Appl. Bio Mater.* 6 (2023) 1806–1815.
<https://doi.org/10.1021/acsabm.3c00041>.
- [248] Y. Herdiana, N. Wathoni, S. Shamsuddin, M. Muchtaridi, Cytotoxicity Enhancement of α -Mangostin with Folate-Conjugated Chitosan Nanoparticles in MCF-7 Breast Cancer Cells, *Molecules.* 28 (2023).
<https://doi.org/10.3390/molecules28227585>.
- [249] X. Long, J. Ren, C. Zhang, F. Ji, L. Jia, Facile and Controllable Fabrication of Protein-Only Nanoparticles through Photo-Induced Crosslinking of Albumin and Their Application as DOX Carriers, *Nanomaterials.* 9 (2019).
<https://doi.org/10.3390/nano9050797>.
- [250] S. Aryal, J.J. Grailer, S. Pilla, D.A. Steeber, S. Gong, Doxorubicin conjugated gold nanoparticles as water-soluble and pH-responsive anticancer drug nanocarriers, *J. Mater. Chem.* 19 (2009) 7879–7884.
<https://doi.org/10.1039/B914071A>.
- [251] K. Kucharczyk, A. Florczak, T. Deptuch, K. Penderecka, K. Jastrzebska, A. Mackiewicz, H. Dams-Kozłowska, Drug affinity and targeted delivery: double

functionalization of silk spheres for controlled doxorubicin delivery into Her2-positive cancer cells, *J. Nanobiotechnology*. 18 (2020) 56.
<https://doi.org/10.1186/s12951-020-00609-2>.

- [252] R. Xu, J. Sui, M. Zhao, Y. Yang, L. Tong, Y. Liu, Y. Sun, Y. Fan, J. Liang, X. Zhang, Targeted inhibition of HER-2 positive breast cancer cells by trastuzumab functionalized pullulan-doxorubicin nanoparticles, *Polym. Test.* 113 (2022) 107669. <https://doi.org/https://doi.org/10.1016/j.polymertesting.2022.107669>.
- [253] Y. Zhang, C. Yang, W. Wang, J. Liu, Q. Liu, F. Huang, L. Chu, H. Gao, C. Li, D. Kong, Q. Liu, J. Liu, Co-delivery of doxorubicin and curcumin by pH-sensitive prodrug nanoparticle for combination therapy of cancer, *Sci. Rep.* 6 (2016) 21225. <https://doi.org/10.1038/srep21225>.
- [254] L. Nair K, S. Jagadeeshan, A. Nair S, G.S.V. Kumar, Folic acid conjugated δ -valerolactone-poly (ethylene glycol) based triblock copolymer as a promising carrier for targeted doxorubicin delivery, *PLoS One*. 8 (2013) e70697.
- [255] N. Ghandhariyoun, M.R. Jaafari, S. Nikoofal-Sahlabadi, S.M. Taghdisi, S.A. Moosavian, Reducing Doxorubicin resistance in breast cancer by liposomal FOXM1 aptamer: In vitro and in vivo, *Life Sci.* 262 (2020) 118520. <https://doi.org/https://doi.org/10.1016/j.lfs.2020.118520>.
- [256] A. Mihanfar, N. Targhazeh, S. Sadighparvar, S.G. Darband, M. Majidinia, B. Yousefi, Doxorubicin loaded magnetism nanoparticles based on cyclodextrin dendritic-graphene oxide inhibited MCF-7 cell proliferation, *12* (2021) 8–15. <https://doi.org/doi:10.1515/bmc-2021-0002>.
- [257] G. Sanità, B. Carrese, A. Lamberti, Nanoparticle Surface Functionalization: How to Improve Biocompatibility and Cellular Internalization, *Front. Mol. Biosci.* 7 (2020). <https://www.frontiersin.org/journals/molecular-biosciences/articles/10.3389/fmolb.2020.587012>.
- [258] M. Sousa de Almeida, E. Susnik, B. Drasler, P. Taladriz-Blanco, A. Petri-Fink, B. Rothen-Rutishauser, Understanding nanoparticle endocytosis to improve targeting strategies in nanomedicine, *Chem. Soc. Rev.* 50 (2021) 5397–5434. <https://doi.org/10.1039/D0CS01127D>.
- [259] G. Yaşayan, B. Şatıroğlu Sert, E. Tatar, İ. Küçükgülzel, Fabrication and

characterisation studies of cyclodextrin-based nanosponges for sulfamethoxazole delivery, *J. Incl. Phenom. Macrocycl. Chem.* 97 (2020) 175–186.

<https://doi.org/10.1007/s10847-020-01003-z>.

- [260] P. Kattel, S. Sulthana, J. Trousil, D. Shrestha, D. Pearson, S. Aryal, Effect of Nanoparticle Weight on the Cellular Uptake and Drug Delivery Potential of PLGA Nanoparticles, *ACS Omega*. 8 (2023) 27146–27155.

<https://doi.org/10.1021/acsomega.3c02273>.

- [261] J. Gautier, E. Munnier, M. Soucé, I. Chourpa, L. Douziech Eyrolles, Analysis of doxorubicin distribution in MCF-7 cells treated with drug-loaded nanoparticles by combination of two fluorescence-based techniques, confocal spectral imaging and capillary electrophoresis, *Anal. Bioanal. Chem.* 407 (2015) 3425–3435.

<https://doi.org/10.1007/s00216-015-8566-9>.